Sorbonne University
Doctoral School of Informatics, Telecommunications and Electronics of Paris
EURECOM

User Equipment Positioning in 5G NR and Beyond

Presented by **Mohsen Ahadi**

Dissertation for Doctor of Philosophy in Information and Communication Engineering

Directed by **Prof. Florian Kaltenberger**

The Jury committee is composed of:

Prof. Stefan Schwarz	TU Wien, Austria	Reviewer
Dr. Maxime Guillaud	INRIA Lyon, France	Reviewer
Prof. Moe Win	MIT, USA	Examiner
Prof. Valérie Renaudin	Université Gustaf Eiffel, France	Examiner
Prof. Jérôme Härri	EURECOM, France	Examiner
Prof. Florian Kaltenberger	EURECOM, France	Thesis Director
Dr. Omid Esrafilian	EURECOM, France	Thesis Co-Supervisor

EURECOM, Sophia Antipolis, 03.12.2025

Sorbonne Université

École Doctorale Informatique, Télécommunications et Électronique de Paris

EURECOM

Localisation de l'utilisateur dans la 5G NR et au-delà

Présenté par **Mohsen Ahadi**

Thèse de doctorat en Sciences de l'Information et de la Communication

Dirigée par **Prof. Florian Kaltenberger**

Le jury est composé de :

Prof. Stefan Schwarz	TU Wien, Autriche	Rapporteur
Dr. Maxime Guillaud	INRIA Lyon, France	Rapporteur
Prof. Moe Win	MIT, États-Unis	Examinateur
Prof. Valérie Renaudin	Université Gustave Eiffel, France	Examinatrice
Prof. Jérôme Härri	EURECOM, France	Examinateur
Prof. Florian Kaltenberger	EURECOM, France	Directeur de Thèse
Dr. Omid Esrafilian	EURECOM, France	Co-Encadrant de Thèse

EURECOM, Sophia Antipolis, 03.12.2025

Abstract

Precise positioning of User Equipment (UE) is a cornerstone for emerging Internet of Things (IoT) applications and intelligent industries, including smart factories, autonomous vehicles, robotics, and smart cities. To address these demands, 5G introduces substantial enhancements in bandwidth, latency, architecture, and dedicated signaling that enable advanced localization services. Despite this potential, accurate positioning in real-world deployments remains challenging. Conventional methods rely on signal's arrival time or angle measurements, which are severely affected by practical impairments such as multi-path propagation, Non-Line-of-Sight (NLoS) links between the user and Transmission Reception Points (TRPs), and synchronization errors arising from hardware imperfections. Moreover, much of the state-of-the-art in the literature relies on simulations or synthetic data, which overlook these real-world limitations and fail to capture the complexity of operational environments, particularly indoors or in dense urban scenarios.

In this dissertation, we adopt an experimental perspective to close this gap. We design and implement a complete 5G positioning system that follows the 3rd Generation Partnership Project (3GPP) specifications, leveraging standard positioning signals, protocols, and architecture. Specifically, we present the first experimental evaluation of the uplink Time Difference of Arrival (TDoA) method integrated within the OpenAirInterface (OAI) platform, including the New Radio Positioning Protocol A (NRPPa) and the Location Management Function (LMF). Furthermore, we deploy this system in diverse indoor and outdoor testbeds using commercial Open RAN (O-RAN) Radio Units (RUs), enabling an unprecedented validation of standard-compliant 5G positioning in practice. Our results demonstrate both the effectiveness and the limitations of TDoA-based methods in real deployments. Motivated by these findings, we further explore advanced solutions based on data-driven and learning-based approaches. Leveraging the large-scale datasets collected from our experimental testbeds, we design supervised and unsupervised models with sensor fusion that can outperform conventional TDoA in scenarios with insufficient measurement quality. Finally, we benchmark these learning-based solutions against both TDoA and commercial high-accuracy alternatives such as Real-Time Kinematic (RTK) positioning, highlighting their potential to overcome constraints of standard methods.

These proposed open-source frameworks, spanning both 5G and beyond-5G standards, together with the publicly shared datasets from our testbeds, constitute a unique contribution to the positioning research community.

Résumé

La localisation précise des équipements utilisateurs (UE) constitue un élément fondamental pour les applications émergentes de l'Internet des objets (IoT) et des industries intelligentes, telles que les usines connectées, les véhicules autonomes, la robotique et les villes intelligentes. Pour répondre à ces besoins, la 5G introduit des améliorations substantielles en termes de bande passante, de latence, d'architecture et de signalisations dédiées, permettant ainsi la mise en œuvre de services avancés de localisation.

Malgré ce potentiel, une localisation précise dans des déploiements réels demeure un défi. Les méthodes conventionnelles reposent sur les mesures de temps ou d'angle d'arrivée du signal, fortement affectées par des limitations pratiques telles que la propagation en trajets multiples (multipath), les liens Non-Line-of-Sight (NLoS) entre l'utilisateur et les points de transmission/réception (TRP), ainsi que les erreurs de synchronisation dues aux imperfections matérielles. De plus, une grande partie de l'état de l'art s'appuie encore sur des simulations ou des données synthétiques, qui ne tiennent pas compte de ces contraintes réelles et ne reflètent pas la complexité des environnements opérationnels, en particulier en intérieur ou dans des zones urbaines denses.

Dans cette thèse, nous adoptons une approche expérimentale afin de combler cette lacune. Nous concevons et mettons en œuvre un système complet de localisation 5G conforme aux spécifications du 3rd Generation Partnership Project (3GPP), en exploitant les signaux, protocoles et architectures normalisés. Plus précisément, nous présentons la première évaluation expérimentale de la méthode uplink Time Difference of Arrival (TDoA) intégrée à la plateforme OpenAirInterface (OAI), incluant le protocole New Radio Positioning Protocol A (NRPPa) et la fonction Location Management Function (LMF). En outre, nous déployons ce système sur plusieurs bancs d'essais, en environnements intérieurs et extérieurs, en utilisant des unités radio commerciales Open RAN (O-RAN RUs), permettant une validation sans précédent de la localisation 5G conforme aux standards.

Nos résultats mettent en évidence à la fois l'efficacité et les limites des méthodes basées sur le TDoA dans des déploiements réels. Motivés par ces constats, nous explorons ensuite des solutions avancées basées sur l'apprentissage automatique et l'exploitation des données. En nous appuyant sur les jeux de données de grande ampleur collectés sur nos bancs d'essais, nous concevons des modèles supervisés et non supervisés intégrant de la fusion de capteurs, capables de surpasser le TDoA conventionnel dans des scénarios où la qualité des mesures est insuffisante. Enfin, nous comparons ces approches apprenantes au TDoA ainsi qu'à des solutions commerciales de haute précision telles que la localisation en cinématique temps réel (RTK), en soulignant leur potentiel pour dépasser les limitations des méthodes standard.

Ces cadres logiciels open-source, couvrant la 5G et les évolutions au-delà de la 5G, ainsi que les jeux de données issus de nos bancs d'essais et rendus publics, constituent une contribution unique à la communauté scientifique travaillant sur la localisation.

Acknowledgment

To my wife, for the endless love,
to my family, missed and far,
to Florian and Omid, for the guiding light.
Mohsen

This work has been funded by the *France 2030* investment program through the *5G-OPERA* and *GEO-5G* projects.

Contents

List of Figures

List of Tables

List of Abbreviations

3GPP	3rd Generation Partnership Project.
AI	Artificial Intelligence.
AMF	Access and Mobility Management Function.
AoA	Angle of Arrival.
AoD	Angle of Departure.
API	Application Programming Interface.
CC	Channel Charting.
CIR	Channel Impulse Response.
CN	Core Network.
CSI	Channel State Information.
CU	Central Unit.
DL	Downlink.
DU	Distributed Unit.
FR1	Frequency Range 1.
FR2	Frequency Range 2.
gNB	Next Generation NodeB.
GNSS	Global Navigation Satellite System.
IoT	Internet of Things.
LMF	Location Management Function.
LoS	Line of Sight.
LTE	Long Term Evolution.
MAC	Medium Access Control.
ML	Machine Learning.
MLE	Maximum Likelihood Estimation.
MQTT	Message Queuing Telemetry Transport.
NLoS	Non-Line of Sight.
NR	New Radio.
NRPPa	New Radio Positioning Protocol Annex.

O-RAN	Open Radio Access Network.
OAI	OpenAirInterface.
PRS	Positioning Reference Signal.
RAN	Radio Access Network.
RIC	RAN Intelligent Controller.
RMSE	Root Mean Squared Error.
RSRP	Reference Signal Received Power.
RSRQ	Reference Signal Received Quality.
RSSI	Received Signal Strength Indicator.
RTK	Real-Time Kinematic.
RU	Radio Unit.
SA	Simulated Annealing.
SA	Stand Alone (5G).
SDP	Semi-Definite Programming.
SIB	System Information Block.
SRS	Sounding Reference Signal.
TDoA	Time Difference of Arrival.
ToA	Time of Arrival.
TRP	Transmission Reception Point.
UAV	Unmanned Aerial Vehicle.
UE	User Equipment.
UL	Uplink.

List of Notations

$\mathbf{u}$	UE position vector.
$\mathbf{x}_m$	m-th TRP position.
M	Total number of TRPs.
K	Total number of gNBs / RUs.
φ	Azimuth angle.
θ	Elevation angle.
T_s	Sampling period.
Δf	Subcarrier spacing.
N_{FFT}	FFT size.
$\mathbf{w}$	CFR vector.
$\mathbf{x}$	Transmitted signal.
$\mathbf{y}$	Received signal.
$\mathbf{n}$	Additive White Gaussian Noise (AWGN).
$\mathbf{k}$	Wave vector.
$\mathbf{s}$	Steering vector.
$\mathbf{r}_e$	Position of antenna element e.
E	Number of antenna elements.
λ_c	Carrier wavelength.
$\mathcal{L}$	Loss function.
$\mathbf{u}^{\text{global}}$	Global best position in PSO.
$\mathbf{u}_p^{\text{local}}$	Local best position in PSO.
$\mathbf{u}_p$	Position of particle p.
$\mathbf{v}_p$	Velocity of particle p.
$\|\cdot\|$	Norm operator.
L	Oversampling factor.
$\hat{d}_{m,1}$	Estimated distance difference between TRP m and reference TRP 1.
c	Speed of light.
$\mathbf{x}_{k,m}$	Position of m-th antenna of RU k.
$\hat{T}_{n,n'}$	Estimated UE displacement.
M_k	Number of TRPs in RU k.
$\mathbf{h}_{k,m_k,t}$	CIR between TRP m_k of RU k and UE at time t.
$\mathbf{H}_{k,t}$	Preprocessed CIR matrix at time t.
$\mathbf{H}_t$	Global CIR matrix across all RUs at time t.
$\tau_{k,m_k,t}^{\text{peak}}$	CIR peak index at TRP m_k of RU k at time t.

$\eta_{k,t}^{\text{offset}}$	Shifting index for RU k at time t.
$\boldsymbol{\Delta}\tau_{k,t}$	TDoA vector across TRPs of RU k at time t.
$\mathcal{D}_{\text{tr}}$	Training dataset of CIRs, TDoA, TRP positions, displacements, and timestamps.
$d_{i,j}$	Displacement between times t_i and t_j.
$b_{i,j}$	Bias term in displacement measurement between t_i and t_j.

Chapter 1

Introduction

1.1 Positioning Systems and Use-Cases

Position estimation is a fundamental enabler for a wide range of applications, from everyday navigation on smartphones to mission-critical operations in intelligent transportation systems, logistics, robotics, and emergency services. In autonomous driving and advanced driver assistance systems, reliable positioning is essential for safety and coordination. In smart factories and warehouses, accurate indoor localization of assets, robots, and workers enables efficient automation, monitoring, and process optimization. Similarly, in smart cities and IoT ecosystems, precise knowledge of device and user locations is key to providing context-aware services, traffic management, and public safety solutions.

Over the past decades, positioning systems have evolved considerably. The first breakthrough came with GPS (Global Positioning System), which revolutionized outdoor navigation by providing accurate global location estimates using satellite signals [1]. GPS and other Global Navigation Satellite Systems (GNSS), such as GLONASS, Galileo, and BeiDou, remain the backbone of global positioning in different countries and continents. However, the performance of satellite navigation systems degrades significantly in certain environments, such as urban canyons, underground spaces, or indoors, due to signal blockage, attenuation, and multipath propagation [2].

To overcome these limitations, a wide range of complementary technologies has been developed. For indoor positioning, solutions include Wi-Fi fingerprinting, Bluetooth Low Energy (BLE) beacons, Ultra-Wideband (UWB), Radio-Frequency Identification (RFID), and Light Detection and Ranging (LiDAR) based localization, each offering trade-offs in terms of accuracy, cost, coverage, and scalability [3]. Additionally, sensor-based approaches utilizing Inertial Measurement Units (IMUs), odometry, and Simultaneous Localization And Mapping (SLAM) techniques offer relative positioning that can be integrated with external references.

More recently, cellular networks have emerged as a promising alternative for ubiquitous positioning. Fourth-generation (4G LTE) networks already offered coarse location capabilities through cell-ID, and signal traveling time measurements. With the advent of fifth-generation (5G) New Radio (NR), new opportunities have been unlocked thanks to wider bandwidths, denser infrastructure, lower latency, and dedicated positioning reference signals, targeting sub-meter accuracy in favorable conditions [4]. Looking forward, beyond-5G and 6G networks aim to integrate Artificial Intelligence (AI), as well as sensing and communication to provide seamless, high-accuracy positioning as a native service of the network.

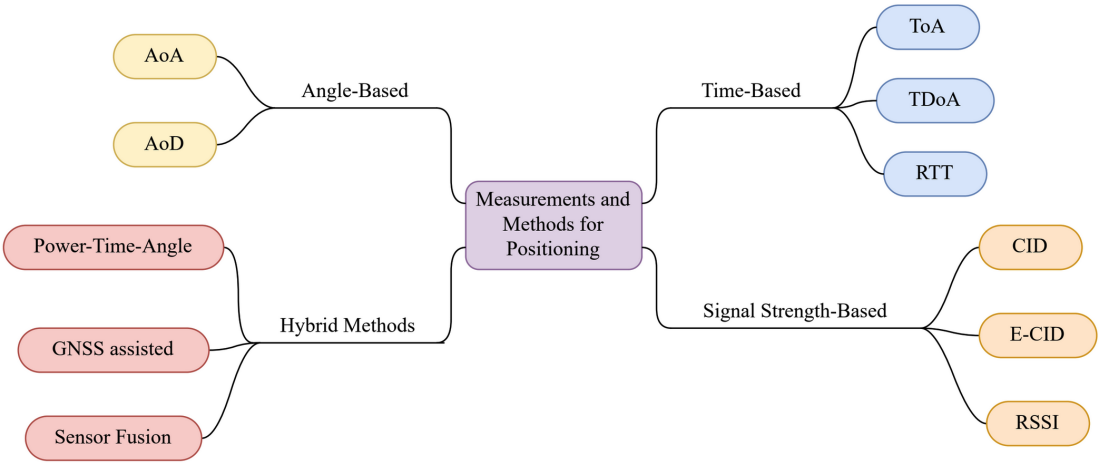

Figure 1.1: Positioning measurements and methods

1.2 Positioning Background in Cellular Networks

The evolution of positioning capabilities in cellular networks from 2G to 5G has been largely shaped by the growing need for location-aware services. Figure 1.1 illustrates various methods used in cellular networks for User Equipment (UE) positioning, based on power, time, or angle measurements, as well as their combinations. In 2G (GSM), basic positioning was enabled primarily through Cell-ID, suitable for coarse applications like emergency calls via E911 [5]. With the transition to 2.5G (EDGE), minor enhancements were introduced, but the positioning remained limited in accuracy. In 3G, more advanced techniques like Time of Arrival (ToA) and Time Difference of Arrival (TDoA) were introduced, supporting services like asset tracking and mobile navigation [6]. The advent of 4G, Long-Term Evolution (LTE) brought higher bandwidths and improved synchronization, enabling enhanced TDoA, Assisted-GNSS (A-GNSS), and hybrid approaches for improved accuracy, supporting commercial applications like geo-fencing and location-based advertising [7]. With 5G NR, positioning capabilities are further enhanced by exploiting features such as mmWave, wide bandwidth, and beamforming that enable accurate TDoA combined with Angle of Arrival/Departure (AoD/AoD) measurements. 5G positioning systems target sub-meter accuracy to support advanced use cases like autonomous driving, industrial automation, and AR/VR [8, 9]. Furthermore, 5G enables fusion of radio signals with sensors such as IMU or LiDAR, for resilient localization in GNSS-denied environments [10]. Most recently, enabling AI has been considered in 3GPP study items, paving the way for data-driven positioning methods in future beyond-5G networks [11].

While radio frequency measurements provide raw information about the radio channel, these quantities must be processed by dedicated estimation algorithms to infer the UE position accurately. Position estimation has been approached via a spectrum of methodologies that differ in their modeling assumptions, computational complexity, and robustness to nonlinearities. Broadly, we distinguish four categories of algorithms:

- Deterministic methods
- Probabilistic/Bayesian filtering methods
- Stochastic or global optimization methods

- Data-driven methods

Deterministic methods such as Linear/Non-Linear/Weighted Least Squares (LLS/NLS/WLS) have closed-form solutions that attempt to solve the system of position equations by linear approximation and involve some known information, such as antenna locations and channel measurements. They are attractive for their simplicity and efficiency, but are sensitive to noisy measurements and imperfect geometry [12].

Probabilistic filters, including Kalman Filter (KF) and its variants (Extended KF, Unscented KF), fuse users' dynamics and channel measurements to predict and correct their position estimation recursively over time. They embed a motion model and measurement likelihood within a recursive Bayesian estimator, providing temporal smoothing and principled uncertainty quantification [13–15].

However, both categories often rely on linearizing the inherently non-linear system of positioning equations, which introduces additional error into the final position estimate. Furthermore, assumptions regarding the availability of an initial estimate or a predefined motion model are not always practical in real-world scenarios.

The third category of algorithms comprises stochastic methods such as Particle Swarm Optimization (PSO), Genetic Algorithms (GA), and Simulated Annealing (SA). These approaches search for the best solution in a non-convex and non-linear space without requiring an initial estimate, and they do not attempt to linearize the positioning model. As a result, when measurement models are highly nonlinear or the cost function contains many local minima, stochastic optimizers can enhance robustness while avoiding linear approximation errors and maintaining an acceptable computational complexity [16–19].

Finally, data-driven approaches such as Finger Printing (FP) or Channel Charting (CC) leverage AI and Machine Learning (ML) together with large datasets, in either supervised or unsupervised settings, to map raw channel measurements to position estimates. This enables the capture of complex propagation characteristics that are difficult to parametrize explicitly [3, 20]. Table 1.1 provides a summary of these methods, organized into their respective categories.

Category	**Methods**
Deterministic (closed-form)	LLS, WLS, NLS [12]
Probabilistic / Bayesian filtering	KF [13], EKF, UKF [15], Particle Filter (PF) [14]
Stochastic optimization	PSO [16], GA [17], SA [18]
Data-driven (AI/ML)	FP [3], CC [20]

Table 1.1: Position Estimation Algorithms

1.3 5G NR Enhancements for Positioning

The Third Generation Partnership Project (3GPP) is the international standards body that defines the technical specifications for cellular networks, including GSM, UMTS, LTE, and 5G NR. Over successive releases, 3GPP has progressively introduced positioning capabilities into cellular systems. With the advent of 5G NR, positioning has become a native service, supported by a dedicated architecture and signaling framework specified in Releases 15, 16, and beyond [4, 21].

Compared to its predecessors, 5G NR brings several fundamental improvements that directly enhance localization performance:

- **Increased bandwidth:** 5G supports channel bandwidths up to 400 MHz, providing fine time resolution that improves signal delay-based measurements such as Time of Arrival

ToA and TDoA. Wider bandwidths reduce the ambiguity in multipath-rich environments and enable sub-meter accuracy under favorable conditions.

- **Low latency:** With end-to-end latency in ultra-reliable low-latency communication (URLLC) modes, 5G enables real-time exchange of positioning signals and assistance data. This is critical for applications such as autonomous driving and industrial automation, where timely location updates are safety-critical.
- **Massive MIMO and beamforming:** Multiple Input Multiple Output (MIMO) with advanced antenna arrays allows highly directional transmission and reception. By exploiting AoA and AoD estimates from beamformed signals, the system can achieve high angular resolution, complementing time-based methods and improving robustness in challenging scenarios.
- **Dense network deployment:** The higher cell density expected in 5G—especially in Frequency Range 2 (FR2) mmWave bands, provides multiple antennas also known as Transmission Reception Points (TRPs) for triangulation. This redundancy increases coverage, geometric diversity, and resilience against blockages.
- **Flexible architecture and signaling:** 3GPP has standardized dedicated Positioning Reference Signals (PRS) in the DownLink (DL) and Sounding Reference Signals (SRS) in the UpLink (UL), along with the NR Positioning Protocol A (NRPPa) that governs signaling between the Location Management Function (LMF) and the 5G base stations (gNBs). The LMF is responsible for coordinating positioning procedures, collecting measurements, and estimating the UE's location in accordance with the standardized architecture.

Together, these capabilities open new possibilities for deploying high-accuracy 5G positioning systems in environments where traditional methods are impractical, such as factory halls, smart warehouses, and private industrial networks where no GPS or GNSS link is available.

While 3GPP-standardized measurements and methods for localization provide a strong foundation, their performance must be assessed under realistic deployment conditions. In practice, several challenges arise. Some techniques bring high implementation cost or complexity for industrial use cases. For example, deploying dense MIMO arrays for angle estimation or ensuring tight network-level synchronization across nodes. Others are constrained by unrealistic requirements, such as the need for the availability of Line of Sight (LoS) link or very wide signal bandwidths to achieve the expected accuracy. In scenarios where these conditions are difficult to satisfy, the research community has increasingly turned to advanced approaches that exploit richer information from the propagation channel, such as raw or processed Channel State Information (CSI). These methods are often data-driven, leveraging AI/ML models to improve robustness, adapt to non-ideal propagation environments, and capture features that traditional parametric models cannot easily represent.

1.4 O-RAN Flexible Framework for 5G Positioning

To support the development and evaluation of advanced techniques such as AI/ML-driven positioning, more flexible frameworks beyond the strict scope of 3GPP specifications are available, most notably the Open Radio Access Network (O-RAN) architecture and its standardized interfaces. O-RAN introduces an open and interoperable RAN design that decouples hardware and software components, enabling multi-vendor deployments and fostering innovation. It specifies functional splits between the Central Unit (CU), Distributed Unit (DU), and Radio Unit (RU), and connects RAN nodes with the Near-Real-Time RAN Intelligent Controller (RIC)

for control and optimization. The O-RAN framework extends the traditional 3GPP RAN by introducing intelligence and programmability into the network through the RIC. The Near-Real-Time RIC enables closed-loop control at timescales suitable for scheduling and measurement-based functions, while the Non-Real-Time RIC provides higher-level policy and long-term optimization. This layered design makes it possible to host third-party applications, such as xApps and rApps, that can be tailored to specific use cases, including AI/ML for positioning. For our research, O-RAN is particularly attractive because it grants access to measurement data and control functions that are typically not available with 3GPP specifications. Researchers can integrate localization algorithms directly into the RIC, experiment with synchronization and filtering methods, or deploy data-driven approaches in realistic environments. In this way, O-RAN serves as a bridge between standardized 5G architecture and the open, flexible experimentation required to advance beyond-5G positioning systems.

1.5 Objectives and Contributions

The activities of this dissertation are based on the objectives of the GEO-5G project. The GEO-5G project is part of the France 2030 investment plan, a national strategy aimed at strengthening France's technological leadership in critical areas such as digital infrastructure, energy, and industry. Within this framework, GEO-5G focuses on advancing 5G geo-location technologies and real-time control of industrial tools and assets in an industrial 5G network. As a partner in this project, Firecell [22], a provider of private 5G networks, contributes by deploying and managing dedicated 5G infrastructures that enable secure connectivity, support advanced industrial applications, and most importantly, provide precise geo-location capabilities.

Based on the background discussed above and the inherent properties of 5G systems, we were motivated to design and implement an end-to-end 5G positioning platform based on OpenAirInterface (OAI) software that delivers cost-efficient and accurate UE localization while maintaining seamless connectivity to smart tools and assets within a 5G network. OAI is an open-source implementation of 5G NR, providing a full software stack for the RAN and Core Network (CN) that supports real-time operation on open and Software Defined Radios (SDR), enabling end-to-end experimentation and standards-compliant prototyping.

Although the literature highlights the potential of 5G for positioning, the performance of a fully integrated end-to-end system has been only marginally investigated under realistic deployment conditions. To address this gap, we experimentally evaluated the standardized 5G positioning methods over the newly integrated positioning protocols and network components on OAI for the first time. In addition, we identified the practical limitations of these methods in real-world setups. Building on these insights, we propose novel methods and open frameworks that extend beyond current 3GPP standardization efforts, and we assess their performance in diverse real-world testbeds.

The main contributions of this dissertation are on the research and development of the state-of-the-art methods of a 5G NR positioning system. We begin by studying various methods of localization in simulation environments such as Matlab. The candidates for the best solutions are implemented and integrated into the OAI RFsimulator as a proof of concept for our proposed 5G positioning system. Next, the selected methods, specifically based on UL-TDoA, were implemented and integrated on OAI Next Generation NodeB (gNB) and CN to be run in a real-time system. We evaluated their performance in various setups by SDRs at the lab as well as commercial RUs in real testbeds. Therefore, we highlighted the potentials and weaknesses of a standard 5G positioning method. Ultimately, methods beyond 5G standards are investigated, implemented, and tested in both simulation and real-world testbeds. Specifically,

we emphasize the potential of deploying AI/ML models on O-RAN RIC, beyond-5G standards, where conventional positioning methods like TDoA may fail. The following list presents the contributions of this dissertation in the order of the chapters, highlighting the progressive evolution of our research toward the overall goal of developing accurate and practical 5G positioning solutions.

Chapter 2: 5GNR Indoor Positioning By Joint DL-TDoA and DL-AoD

The fundamentals of UE positioning in a 5G NR network is covered in this chapter. By focusing on TDoA of DL-PRS in a mm-Wave and MIMO simulation setup, we studied the potentials of 5G positioning in a simulated Indoor Factory Hall scenario by Ray-Tracing and 3-D map based channel modeling. The research presented in this chapter has led to the following publication:

- **Mohsen Ahadi**, Florian Kaltenberger, "5GNR Indoor Positioning By Joint DL-TDoA and DL-AoD," *2023 IEEE Wireless Communications and Networking Conference (WCNC), Glasgow, United Kingdom*, 2023.

Chapter 3: 5G NR UL SRS TDoA Positioning by OpenAirInterface

This chapter takes the first practical steps toward implementing a 5G NR positioning end-to-end system using the OAI RF-simulator. In this setup, a mobile UE is simulated in the RF-simulator environment, while the MQTT protocol is integrated to emulate NRPPa signaling. The UE's position is then estimated in real time by a positioning algorithm running on an LMF emulation implemented in Matlab. The work described in this chapter resulted in the following publication:

- **Mohsen Ahadi**, Adeel Malik, Florian Kaltenberger, Cedric Thienot, "5G NR UL SRS TDoA Positioning by OpenAirInterface.", *2023 Indoor Positioning and Indoor Navigation conference Work in Progress (IPIN-WiP), Nuremberg, Germany*, 2023.

Chapter 4: Experimental Insights From OpenAirInterface 5G Positioning Testbeds: Challenges and Solutions

The successful outcomes of the three positioning testbeds that integrate the first open-source NRPPA and LMF to the OAI are presented in this chapter. The localization pipeline on the LMF is the main contribution of this dissertation. The research outcomes of this chapter have been published as follows:

- **Mohsen Ahadi**, Adeel Malik, Omid Esrafilian, Florian Kaltenberger, Cedric Thienot, "Experimental Insights from OpenAirInterface 5G positioning Testbeds: Challenges and solutions" *The 19-th ACM Workshop on Wireless Network Testbeds, Experimental evaluation & Characterization (WiNTECH)*, Hong Kong, China, 2025.

Chapter 5: Global Scale Self-Supervised Channel Charting with Sensor Fusion

Unlike previous attempts on standard TDoA positioning, this chapter proposes a beyond-5G approach for localization using CSI data. While CSI can not be transferred over NRPPA to the LMF, this work emphasizes the potential of CSI in training data-driven positioning models. The findings of this chapter have been reported in the following publication:

- Omid Esrafilian[1], **Mohsen Ahadi**[1], Florian Kaltenberger, David Gesbert, "Global Scale Self-Supervised Channel Charting with Sensor Fusion", *2024 IEEE Globecom Workshops (GC Wkshps), Cape Town, South Africa*, 2024

Chapter 6: Uplink TDoA-Based Self-Supervised Channel Charting with NLoS Mitigation

This chapter covers the extension of the previous chapter on CC method. This work has a more practical approach by exploiting the TDoA measurements as well as TRP locations to obtain a position estimation function. The results in simulation and GEO-5G testbed demonstrate an accurate UE localization in a mixed LoS/None Line of Sight (NLoS) signal condition with CC. The contributions of this chapter have appeared in the following publication:

- **Mohsen Ahadi**, Omid Esrafilian, Florian Kaltenberger, "Uplink TDoA-Based Self-Supervised Channel Charting with NLoS Mitigation" *IEEE Transactions on Machine Learning in Communications and Networking*,2025.

Chapter 7: Conclusions

This chapter summarizes the main objectives, contributions, and achievements of this dissertation. It also outlines future research directions by envisioning the prospects and potential of positioning technologies beyond the current 5G standards.

Other Research Contributions

Publications:

Considerable effort was devoted in this project to the integration and testing of newly implemented network functions, such as NRPPa and the LMF, within the GEO-5G testbed at EURECOM. As a result of this work, a dedicated article describing the implementations has been published. Moreover, two of the resulting publications on this work have been invited for inclusion in the COST INTERACT book, within Working Group 2 (WG2) on Signal Processing and Localisation.

- Adeel Malik, **Mohsen Ahadi**, Florian Kaltenberger, Klaus Warnke, Nguyen Tien Thinh, Nada Bouknana, Cedric Thienot, Godswill Onche, Sagar Arora, "From concept to reality: 5G positioning with open-source implementation of UL-TDoA in OpenAirInterface", *2025 IEEE International Conference on Computer Communications (INFOCOM), London, United Kingdom*, 2025
- COST INTERACT book WG2 on localization including two of our publications [23, 24].

Demonstrations:

Throughout the course of this project, several demonstrations were carried out to showcase the evolution of our 5G positioning system and methodologies. These demos highlighted different milestones, ranging from early RF-simulator-based UL SRS TDoA positioning to the integration of NRPPa and LMF in OAI, and later to advanced AI-based techniques such as channel charting and UAV-based localization. The demonstrations were presented at leading international conferences and OAI community workshops, reflecting both the technical maturity and the growing impact of this work.

[1]The first two authors contributed equally.

- *Indoor Positioning Indoor Navigation (IPIN) Conference, 2023*, RFsimulator based UL SRS TDoA positioning demo,
- *OAI's 10th anniversary workshop, EURECOM France, 2024*, NRPPA and LMF in OAI positioning demo,
- *OAI's 11th summer workshop, Kista, Sweden,2025*, Channel Charting and TDoA positioning demo,
- *IEEE International Conference on Communications (ICC), 2025*, Drone localization based on Channel Charting demo at "Learning and Sensing in the Sky with UAV-aided 6G Networks",
- *First OAI U.S. Hands-on Workshop, University of Texas at Austin, 2025*, O-RAN 6G positioning based on channel charting with OpenAirInterface and FlexRIC demo.

Chapter 2

Methodology

This chapter presents two major 5G standard network architectures that employed in this work to investigate and validate advanced techniques for UE positioning. In both architectures, the fundamental problem consists of estimating the location of a UE with unknown position $\mathbf{u} = (x, y, z)$ based on the measurements collected by the network. The network infrastructure is composed of one or multiple gNBs connected to a 5G CN. Each gNB is equipped with one or several antennas, which can be abstracted as TRPs with known and fixed positions $\mathbf{x}_m = (x_m, y_m, z_m),\ m \in \{1, \ldots, M\}$. A schematic of Outdoor and Indoor scenarios for UE positioning are depicted in Figures 2.1 and Figure 2.2.

- The conventional 3GPP architecture for a 5G network,
- The flexible O-RAN architecture for a 5G network.

It is important to note that the two architectures are often used in a complementary manner.

Furthermore, our methodology for addressing the UE positioning problem in 5G networks follows a progressive approach. We began by studying state-of-the-art methods and assessing their strengths and limitations in simulated environments. Based on these insights, we implemented the necessary network components for the positioning procedure on OAI and developed an end-to-end proof of concept. After validating the procedure through both high-level and low-level simulations, we advanced to real-world evaluations by deploying experimental testbeds and testing the proposed methods under realistic conditions.

2.1 3GPP Standard 5G Network Architecture

The 3GPP specifies a comprehensive 5G network architecture that includes one or multiple gNBs and a CN, along with key positioning-related components such as the AMF and LMF, thereby enabling both UL and DL UE positioning [25]. In UL positioning, the UE transmits SRS [26] that are received by TRPs, then the UE-TRP channel parameters, such as power, time, or angle, are measured. These measurements are reported by the NRPPA [27] to the LMF [28] via Access and Mobility Management Function (AMF)[29] on the CN for further processing and estimating the UE's location. In case of DL, gNBs transmit the PRS [26]. The UE performs the channel estimation and reports the measured parameters to the LMF by LTE Positioning Protocol (LPP)[30]. These messages go through the gNB and AMF transparently. Figure 2.3 is an illustration of a simplified 3GPP positioning architecture.

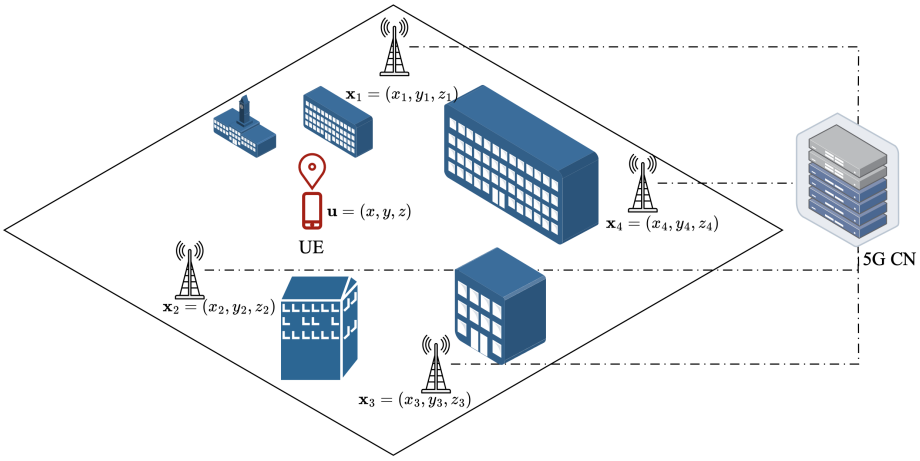

Figure 2.1: Outdoor UE positioning scenario with 5G system model

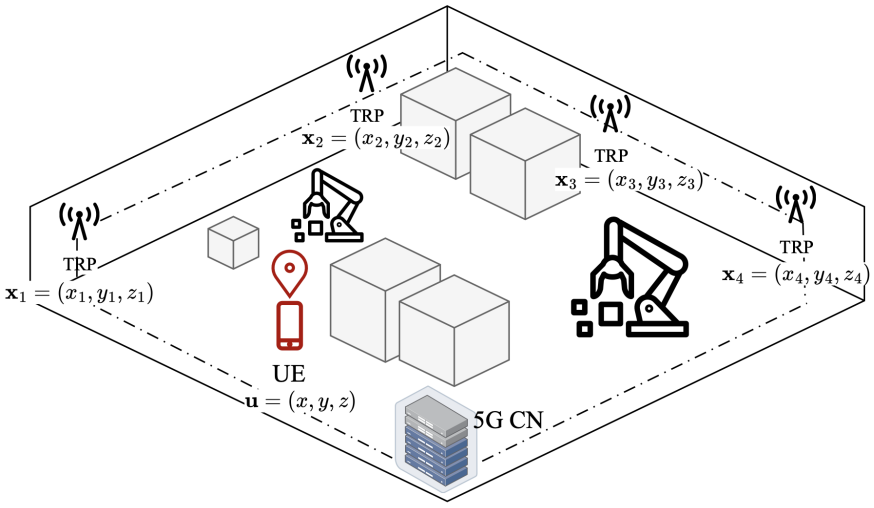

Figure 2.2: Indoor UE positioning scenario with 5G system model

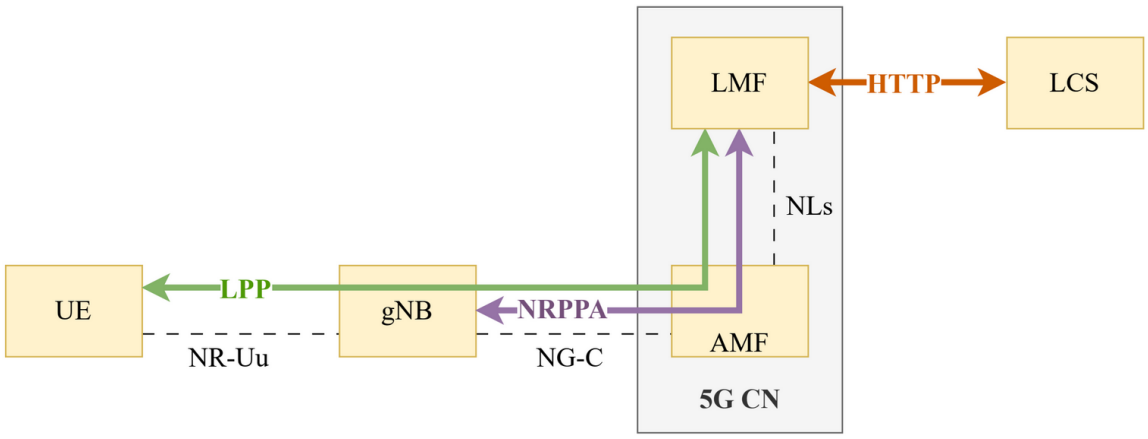

Figure 2.3: 3GPP 5G Network Architecture

2.1.1 NRPPA procedures

The NRPPa defines numerous message exchanges between the LMF and the gNB in support of NR positioning methods such as UL-TDoA, which is one of the main focuses of this dissertation. This procedure is designed to be initiated by a Location Services (LCS) API and finalized by receiving the LMF's estimated location at the LCS. A summary of this procedure in 10 steps is as follows.

Message 1: Initiation of Location Request, *External API →LMF* The process begins when an external LCS API, such as an advanced interface or simply a one-line *curl* command, sends an HTTP POST request to the *determine-location* API of the LMF. This request specifies the following;

- LMF IP address,
- The target UE's Subscription Permanent Identifier (SUPI),
- The gNB's NR Cell Global Identifier (NCGI).

Upon receiving this request for a specific UE, the LMF initiates the NRPPa procedure to retrieve the required information from gNBs for UL-TDoA positioning.

Message 2/3: TRP Information Request/Response, *LMF →gNB/ gNB →LMF* The LMF requests the configuration and coordinates of the TRPs from the serving gNB. The response includes:

- TRP ID,
- Geographical coordinates of each TRP.

Message 4/5: Positioning Information Request/Response, *LMF →gNB/ gNB →LMF* The LMF queries the gNB for the UE's reference signal configuration to support positioning. The response specifies:

- SRS configuration.

Message 6/7: Positioning Activation Request/Response, *LMF →gNB/ gNB →LMF* The LMF activates the positioning session by providing:

- NRPPa Transaction ID,

- System Frame Number,
- Slot Number.

Message 8/9: Measurement Request/Response, *LMF →gNB/ gNB →LMF* The LMF instructs the gNB to perform uplink measurements. The measurement results returned include:

- TRP ID,
- UL Relative Time of Arrival (RToA) measurements,
- gNB Rx–Tx time difference.

Message 10: Location Response, *LMF →External API* Finally, the LMF computes and returns the UE's estimated position, expressed as:

- Geographical coordinates (latitude, longitude, altitude),
- Relative Cartesian coordinate (x, y, z) with respect to the reference TRP set.

Figure 2.4 is a summary of the positioning procedure covering messages 1 to 10 as described above.

2.2 O-RAN 5G Network Architecture

O-RAN defines an open and intelligent RAN architecture [31] that separates the functionalities of the gNB into open CU, DU, and RU. This functional disaggregation not only provides flexibility in deployment but also allows the integration of vendor-neutral hardware and software solutions, which is a fundamental objective of the O-RAN Alliance. The CU generally handles higher-layer processing tasks, while the DU focuses on lower-layer real-time functions, and the RUs are responsible for the RF front-end operations.

A central innovation introduced by O-RAN is the possibility of hosting external control applications, referred to as xApps, on the RIC. These applications enable advanced functionalities such as dynamic resource allocation, interference management, and network-aware positioning. Among the interfaces defined by O-RAN, the E2 interface plays a crucial role in positioning. The E2 interface enables near-real-time control and bidirectional data exchange between the CU/DU components of the RAN and the Near-RT RIC. This connectivity makes it possible to extract detailed radio measurements and network statistics directly from the live RAN.

In the context of positioning, the E2 interface allows extended radio measurements, such as CSI, to be forwarded to the Non-RT RIC for offline processing, analytics, and the training of machine learning models. The same measurements can be simultaneously delivered to the Near-RT RIC, which is responsible for time-sensitive operations such as real-time position inference, decision-making, and dynamic adaptation of the positioning algorithms. This separation of roles ensures that computationally heavy tasks like training are offloaded to the Non-RT RIC, while fast inference and adaptation occur within the Near-RT domain.

Figure 2.5 illustrates the overall O-RAN architecture and its main components, highlighting the E2 interface as the key enabler for positioning-related data collection and control signaling. By leveraging this architecture, O-RAN creates an interoperable, flexible, and intelligent framework for deploying advanced 5G positioning solutions in both research and real-world networks.

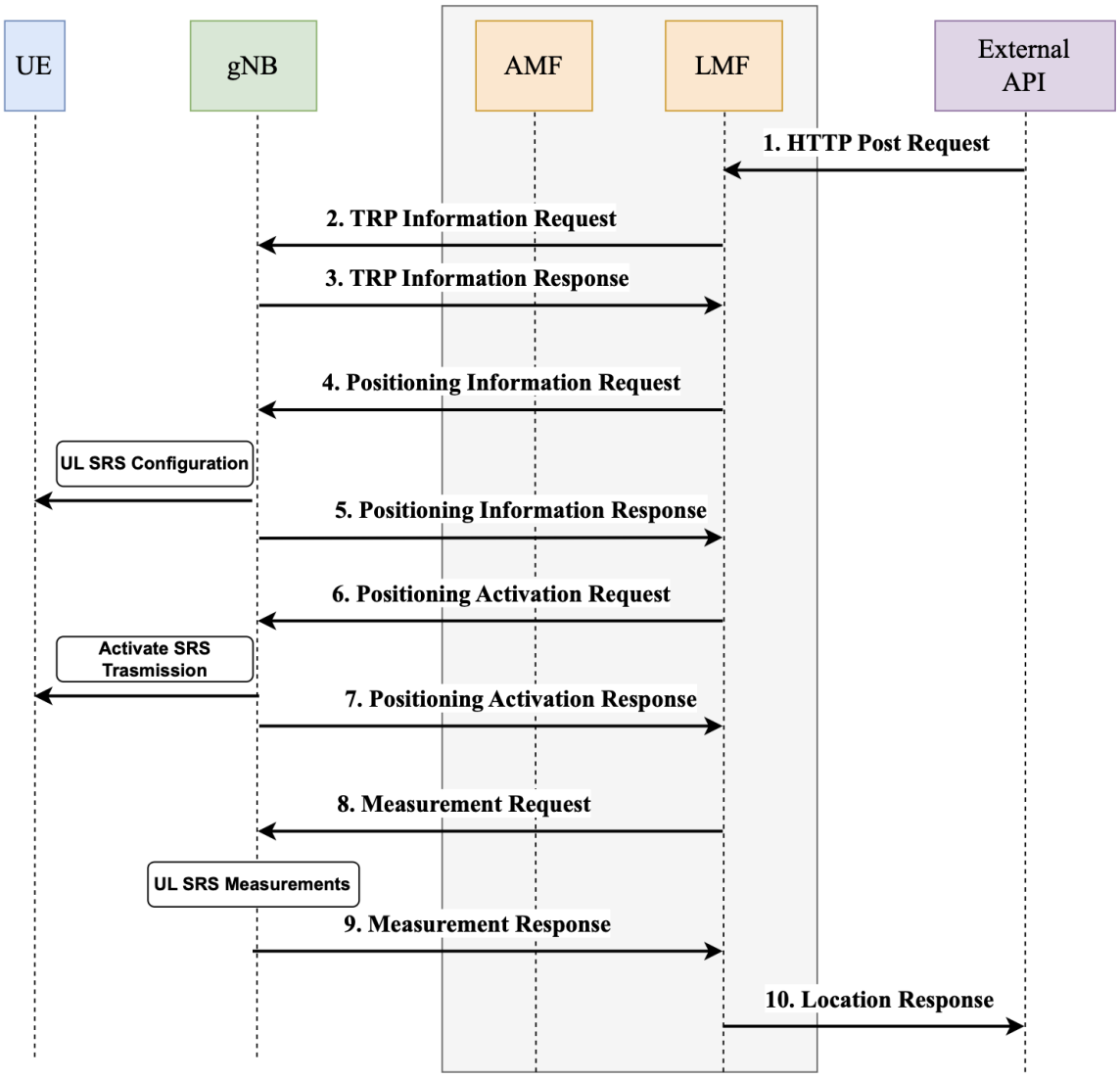

Figure 2.4: NRPPA positioning procedure

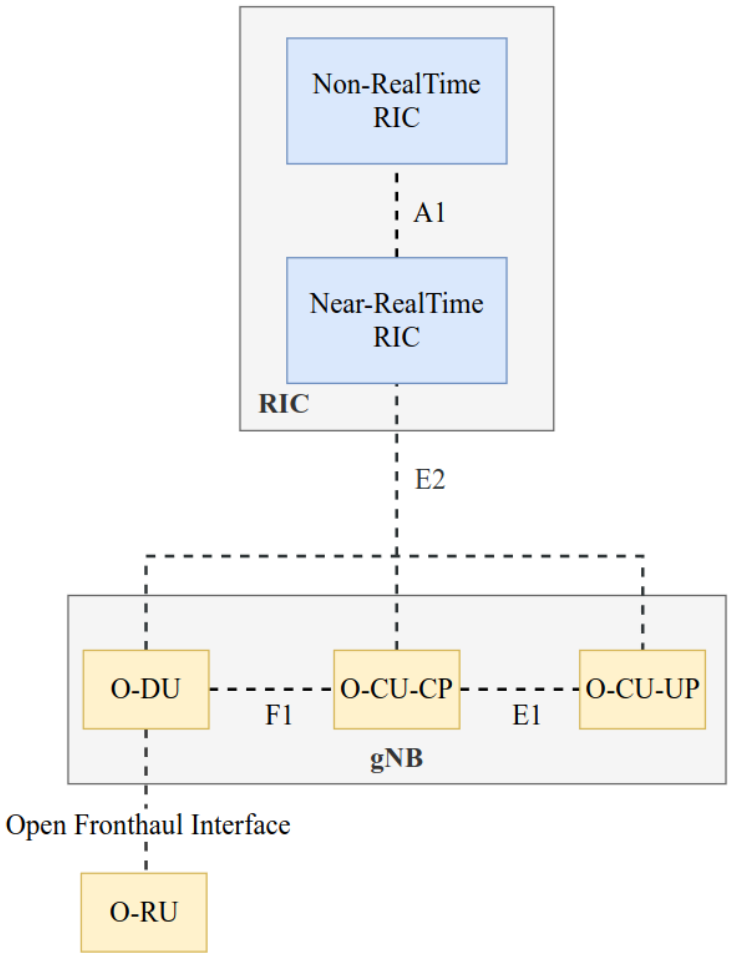

Figure 2.5: O-RAN 5G network architecture

2.3 Methodology

2.3.1 Matlab Simulations

Matlab simulations were employed as the first step in our methodology to validate positioning algorithms under controlled conditions. Using the 5G Toolbox together with ray-tracing techniques and 3D map-based propagation modeling, we created realistic channel environments that reflect the complexity of urban and indoor deployments. To ensure compliance with standard assumptions, we also integrated channel models specified in 3GPP [4] and [32]. These experiments enabled a high-level implementation of the proposed algorithms, allowing us to assess their feasibility, evaluate their performance, and identify potential limitations at low computational cost before moving to more detailed system-level integration.

2.3.2 OAI RF Simulator Environment

OAI provides an RF simulator (RFsim) that enables testing without the need for physical RF hardware [33]. Acting as a virtual RF board, it emulates the behavior of a real front-end by forwarding samples between the gNB and UE rather than transmitting them over the air. In this

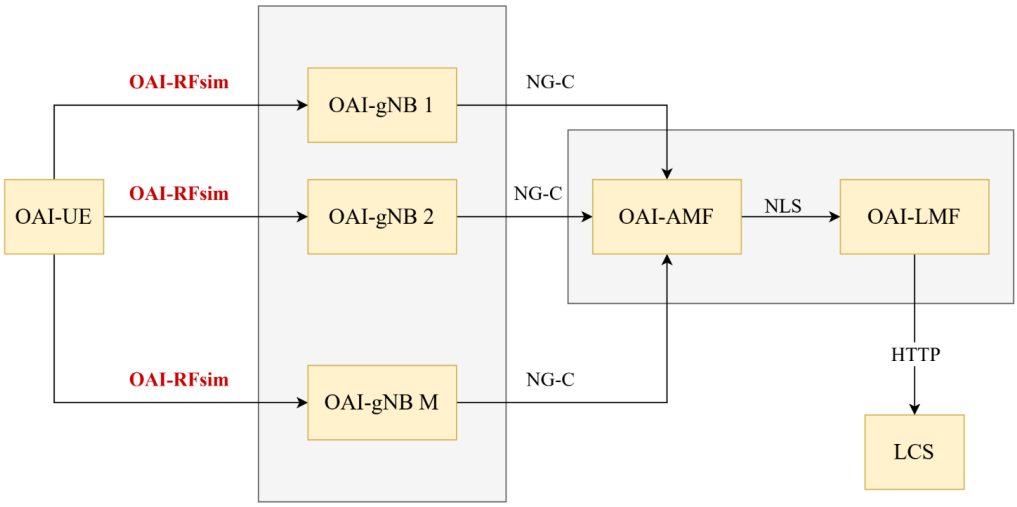

Figure 2.6: OAI RFsim positioning diagram

setup, the time-domain OFDM waveform is exchanged through a socket, allowing the simulation of simple channels such as AWGN and enabling end-to-end testing in a fully software-based environment. As shown in Figure 2.6, the over-the-air link between the OAI-UE and multiple OAI-gNBs is emulated by the OAI RFsim. In addition, our demonstrations showed that UE mobility can be simulated using a *telnet server*, which provides a simple interface to control the multiple gNB-UE channel parameters dynamically during the simulation. This functionality enables the evaluation of a simple mobility scenario without the need for physical hardware movement.

2.3.3 Experimental Positioning Testbed

While significant progress has been made in improving positioning accuracy using synthetic data within simulation environments, comparatively little effort has been dedicated to validating these approaches in a standardized and reproducible way on real-world testbeds. Such validation is crucial for revealing the practical challenges encountered during deployment. The experimental works in this dissertation are built upon the OAI platform to implement and evaluate positioning capabilities.

To the best of our knowledge, our work is the first to present positioning results from a fully open-source, 3GPP-compliant implementation on OAI, covering both the RAN and CN components, including a standard LMF and NRPPA for the first time. Furthermore, we validate this framework with commercial RUs across diverse testbeds, demonstrating its practical deployment readiness.

On the experimental evaluation of our 5G positioning system, we have deployed multiple real-world testbeds in various environments. Specifically, we test the UL-TDoA positioning system model where a UE transmits the UL-SRS signal to multiple O-RAN RUs provided by Firecell with distributed TRPs in a disaggregated gNB (CU-DU-RU) form. It is essential to achieve tight synchronization among the RUs. This is done in our setups by the Precise Timing Protocol (PTP) that distributes a timing signal from a GNSS PTP grandmaster to all RUs over a switch. Next, the gNB collects the ToAs from all TRPs and sends them along with the TRP coordinates to the LMF on the CN, where the localization algorithms take the TDoA and

estimate the UE's position. This system model is shown in Figure2.7.

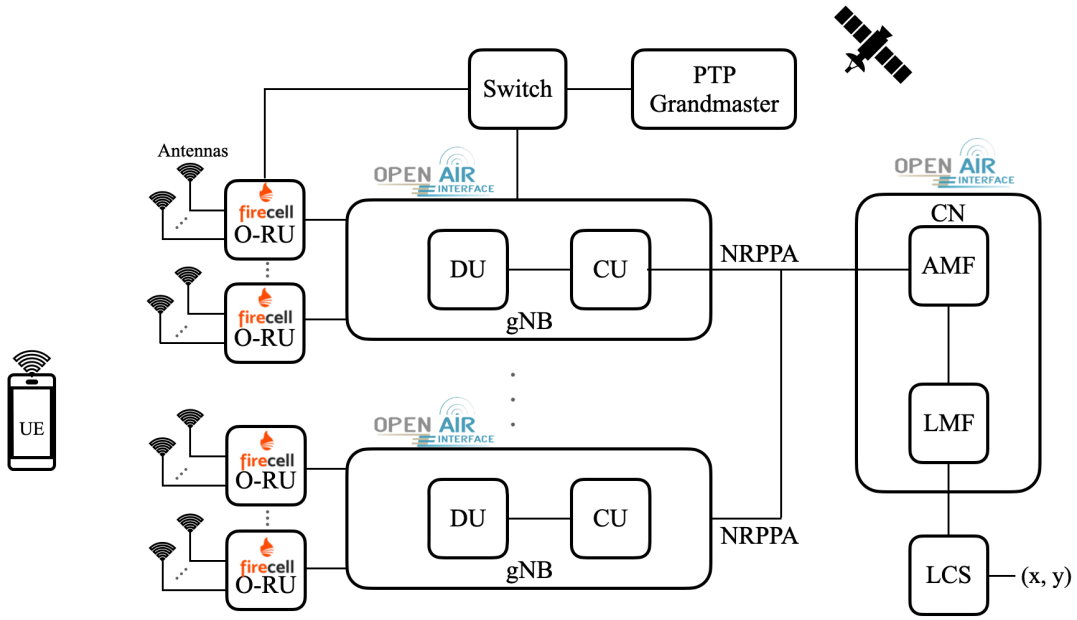

Figure 2.7: UL-TDoA positioning testbed generic architecture

Building on the UL-TDoA positioning model described above, this section introduces three distinct localization testbeds.

- Outdoor GEO-5G testbed at EURECOM,
- Indoor Stellantis testbed at MatternLab,
- Indoor Airbus testbed at Airbus Atlantic.

These testbeds cover both indoor and outdoor scenarios with diverse channel conditions and propagation characteristics. Each setup poses specific challenges related to time synchronization, TRP deployment, and channel estimation, among others. To address these, we design tailored LMF pipelines that enable accurate positioning across different environments. Moreover, our proposed AI/ML models in this dissertation are also trained and evaluated based on the collected data from these testbeds.

(a) GEO-5G testbed at EURECOM

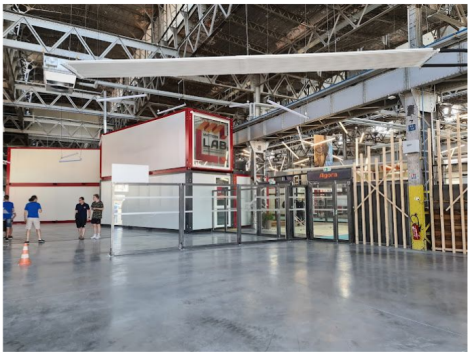

(b) Stellantis testbed

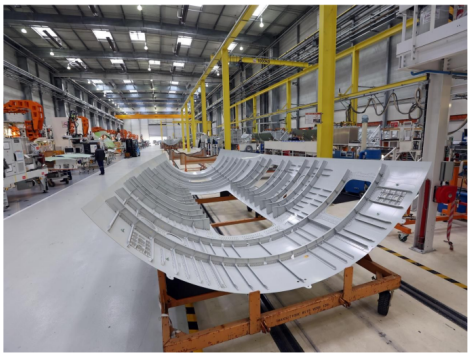

(c) Airbus testbed

Figure 2.8: Overview of 5G positioning testbeds

Chapter 3

5GNR Indoor Positioning By Joint DL-TDoA and DL-AoD

This chapter presents the fundamentals of UE DL positioning in a 5G NR network, including the 3GPP-defined architecture, PRS, NRPPa, and standard estimation methods. We further introduce a joint approach that combines DL-TDoA and DL-AoD for position estimation, which significantly improves accuracy in Multi-Input Multi-Output (MIMO) and mmWave simulation setups. The results demonstrate the potential of 5G NR positioning, particularly in indoor environments where high-precision GPS localization is unavailable.

3.1 Introduction

Location information of mobile devices enables a wide range of services, including Industry 4.0 and IoT, and also helps operators improve network performance [34]. Since GNSS cannot provide reliable estimates in indoor scenarios, 5G NR Stand Alone (SA) networks, particularly in FR2 with wideband signals, low latency, beamforming, and multi-antenna angle estimation, offer strong potential for accurate indoor positioning.

Several methods have been studied, including ToA [35, 36], TDoA [37], RSS [38, 39], and AoA/AoD [40]. Prior works address positioning from geometric formulations [41], TDoA refinements [42–45], and DL-AoD least-squares estimation [46], while other studies highlight limitations of AoA for UEs with few antennas. To overcome these challenges, we propose a joint DL-TDoA and DL-AoD positioning algorithm that leverages network-side reporting [47], avoids large UE antenna arrays, and achieves sub-meter accuracy in both horizontal and vertical domains for indoor scenarios without GNSS LOS.

The 5G positioning architecture in 3GPP Release 16 [47] introduces new functions in the RAN and Core, such as the LMF and NRPPA signaling, extending the LTE positioning model. Multiple TRP/antennas on gNBs and the availability of mmWave in NR enable new measurements, including DL-AoD and DL-TDoA of positioning reference signals [48]. By combining these angles and time measurements with gNB coordinates, accurate UE positioning in both horizontal and vertical planes can be achieved, as demonstrated in this chapter.

3.1.1 Positioning Reference Signal

3.1.1.1 PRS Resource Set and Resources

One positioning frequency layer is made of one or more PRS resource sets distributed over one or more sites, all of which use the same carrier frequency and OFDM numerology. Each PRS resource in a resource set corresponds to a beam from a single location. When configuring a device to measure on a specific PRS resource in a PRS resource set, the location server learns not only which site the reported measurements for this PRS resource set belong to, but also the specific beam from that site [49].

3.1.1.2 PRS Comb Size

PRS setup enables a permuted staggered comb. In this application, permuted indicates that the comb in each OFDM symbol has a distinct offset in the frequency domain. The comb factor can be adjusted to 2, 4, 6, or 12 sub-carriers, which means that the comb is used on every 2nd to every 12th sub-carrier. Using various combs, numerous simultaneous PRSs may be multiplexed.

3.1.1.3 PRS Bandwidth

A PRS resource in the frequency domain can be configured to have up to 264 Physical Resource Blocks (PRB) with Subcarrier Spacing (SCS) 120 KHz, which makes 400 MHz Band Width (BW) in FR2, with all PRS resources in a PRS resource set having the same bandwidth and frequency domain location. In the time domain, one PRS resource is represented by two, four, six, or twelve OFDM signals.

3.2 AoD Estimation

3.2.1 Phased Antenna Array

Uniform Rectangular Array (URA) is a system of identical antenna elements. Array elements are distributed in the yz-plane in a rectangular lattice. The array bore sight is along the x-axis. In this chapter, we used a 2×2 and a 4×4 transmit antenna arrays, which provide 4 and 16 beams, respectively. To estimate the AoD, each gNB goes through a beam training process with a code book containing a set of code words $C^P = \{\mathbf{w}^1, ..., \mathbf{w}^P\}$ [50]. Therefore, a coarse estimation for the AoD of the propagation path is described as:

$$p^* = \arg\max_{p \in \mathcal{P}} A^p \tag{3.1}$$

where the beam with code word $\mathbf{w}^p(\theta, \phi)$ maximizes the received power A^p on the UE. Without considering the noise, the ideal received signal strength is given by:

$$A^p = \sqrt{\left(\mathbf{h}\mathbf{w}^p\left(\theta, \phi\right)\right)^H \left(\mathbf{h}\mathbf{w}^p\left(\theta, \phi\right)\right)} \tag{3.2}$$

Thus, A^p can be used to estimate the beam index that refers to the elevation (θ), and azimuth (ϕ) of departure [50].

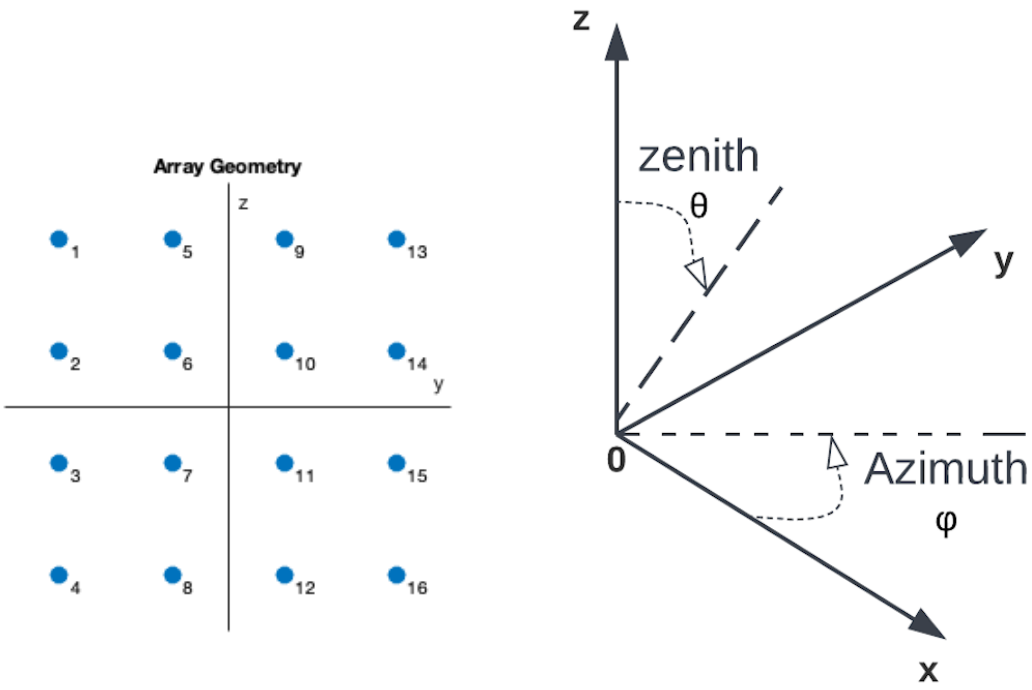

Figure 3.1: Array geometry and coordinate system

3.2.2 Beamforming

Beam management is a set of Layer 1 (PHY) and Layer 2 (MAC) procedures to acquire and maintain beam pair links [51], i.e., a transmit beam at the gNB's TRP paired with a receive beam at the UE. Beam sweeping is required at both TRP and UE sides to establish such a beam pair. On the TRP side, analog beamforming is applied to each PRS resource. The azimuth and elevation directions of the beams are determined by the number of antenna elements and the configured sweep ranges. Each PRS resource is beamformed in one of these directions and transmitted on the DL, while the UE sequentially measures the received power across its own receive beams.

In general, for B_{TX} transmit beams and B_{RX} receive beams, each of the B_{TX} beams is transmitted B_{RX} times so that all transmit beams are measured across the B_{RX} receive beams. For example, with a 4×4 TX antenna array, 16 beam pairs (φ, θ) are generated to transmit DL-PRS within the ranges $\varphi \in (-45°, 45°)$ and $\theta \in (-45°, 0°)$.

A wave propagating in the direction (φ, θ) is described by the wave vector

$$\mathbf{k}(\varphi, \theta) = \frac{2\pi}{\lambda}\big(\cos\theta\cos\varphi,\ \cos\theta\sin\varphi,\ \sin\theta\big), \tag{3.3}$$

where λ is the wavelength.

For an antenna array with E elements located at positions

$$\mathbf{r}_e = (x_e, y_e, z_e), \quad e = 1, \ldots, E, \tag{3.4}$$

The steering vector $\mathbf{s}(\varphi, \theta)$ is an $E \times 1$ complex vector representing the relative phase shifts

across the elements:

$$\mathbf{s}(\varphi,\theta) = \begin{bmatrix} e^{-j\mathbf{k}\cdot\mathbf{r}_1} \\ e^{-j\mathbf{k}\cdot\mathbf{r}_2} \\ \vdots \\ e^{-j\mathbf{k}\cdot\mathbf{r}_E} \end{bmatrix}. \tag{3.5}$$

Each PRS resource is multiplied by its corresponding steering vector to form a beam in the desired spatial direction.

3.2.3 RSRP Measurement

After the dual-end sweep has been completed over TX and RX antennas, the best beam-pair link based on the highest RSRP measurement has to be determined. In this case, with a single UE antenna, a TX beam has to be determined. The DL-PRS Reference Signal Received Power (DL-PRS-RSRP) is calculated as the linear average of power contributions of resource elements that are configured to carry DL-PRS reference signals. Within the NR Frequency Range 2 (FR2), DL PRS-RSRP is determined by combining the signals from antenna elements within a given receiver branch [52].

3.3 TDoA Estimation

Based on the RSRP measurements, the pair of TX and RX beams has been identified for further processing of the TDoA. The time difference calculation on the UE avoids exact time synchronization requirements to the gNB. Note that TDoA-based positioning schemes still require clock synchronization between all the gNBs in the system and frequency synchronization between the UE and the gNBs. The DL reference signal time difference (DL-RSTD) [52] is the DL relative timing difference between positioning node n and reference positioning node 1 to be assumed. In frequency range 2, the antenna of the UE shall be the reference point for the DL-RSTD.

3.3.1 Channel Estimation

To measure the DL-TDoA based on PRS resources, a channel estimation algorithm is used to calculate the timing offset between the reception and transmission of PRS resources. As Channel Estimation in OFDM Systems describes [53], the least-squares estimates of the channel frequency response at the pilot symbols are computed. To minimize any undesired noise from the pilot symbols, the least squares estimates are then averaged across time then frequency bandwidth, with a growing window size that is proportional to the channel coherence time. Later, the findings will be interpolated over the whole sub-carriers in the bandwidth. In the next step, the frequency domain channel estimation is converted into an impulse response using an inverse Fourier transform. This result leaves us with some peaks, which show when in time we received positioning reference signals. In this stage, as UE is synchronized with one of the gNBs, the timing difference between the provided channel estimation peaks is considered as the time difference of arrival or TDoA.

3.4 Joint AoD--TDoA Position Estimation

The trigonometric functions of the estimated azimuth φ and elevation θ angles of departure, together with the range differences $c \times TimeDifferenceofArrival(TDoA)$ between TRPs, are used in the positioning equations to compute the unknown UE coordinates. Taking $\mathbf{u} = (x, y, z)$

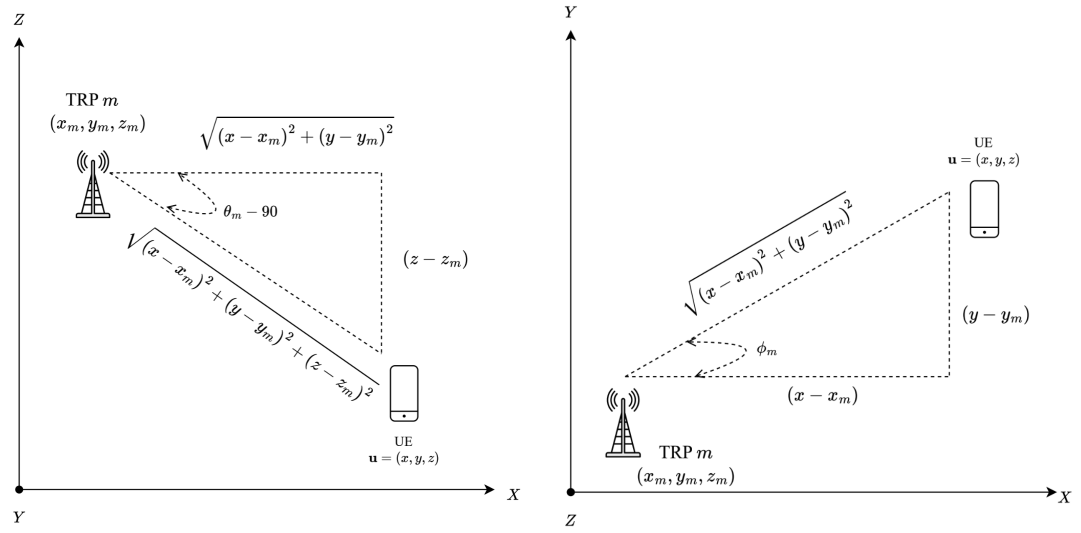

(a) Elevation (zenith) angle θ (b) Azimuth angle φ

Figure 3.2: Azimuth and elevation angles of departure.

as the UE position and $\mathbf{x}_m = (x_m, y_m, z_m)$ as the position of the m-th TRP, the system of equations can be expressed as

$$\mathbf{f}(\mathbf{u}) + \mathbf{e} = \mathbf{r}, \tag{3.6}$$

where $\mathbf{f}$ contains $(3M-1)$ equations for M TRPs (with $2M$ angle observations and $M-1$ time observations).

Elevation AoD constraint:

$$f_{AoD,2m-1}(\mathbf{u}) = \cos(\theta) = \frac{z - z_m}{\sqrt{(x-x_m)^2 + (y-y_m)^2 + (z-z_m)^2}}. \tag{3.7}$$

Azimuth AoD constraint:

$$f_{AoD,2m}(\mathbf{u}) = \sin(\varphi) = \frac{y - y_m}{\sqrt{(x-x_m)^2 + (y-y_m)^2}}. \tag{3.8}$$

TDoA constraint:

$$f_{TDoA,m}(\mathbf{u}) = d_m - d_1 = \|\mathbf{u} - \mathbf{x}_m\| - \|\mathbf{u} - \mathbf{x}_1\|, \qquad m = 2, \ldots, M, \tag{3.9}$$

where $d_m = \|\mathbf{u} - \mathbf{x}_m\|$ is the range between the UE and the m-th TRP. TRP 1 is chosen as the reference (assumed LoS with the strongest signal).

3.4.1 Taylor Series Decomposition

The set of non-linear equations at iteration i for point $\mathbf{u}^{(i)} = (x^{(i)}, y^{(i)}, z^{(i)})$ can be solved by applying a Taylor series decomposition and truncating to the linear term [54]:

$$\mathbf{f}(\mathbf{u}) \approx \mathbf{f}(\mathbf{u}^{(i)}) + \mathbf{D}^{(i)}(\mathbf{u} - \mathbf{u}^{(i)}), \tag{3.10}$$

where $\mathbf{D}^{(i)}$ is the $(3M-1)\times 3$ Jacobian matrix of partial derivatives at $\mathbf{u}^{(i)}$.

$$\mathbf{D}^{(i)} = \begin{bmatrix} \frac{\partial f^{(i)}_{AoD,1}}{\partial x} & \frac{\partial f^{(i)}_{AoD,1}}{\partial y} & \frac{\partial f^{(i)}_{AoD,1}}{\partial z} \\ \vdots & \vdots & \vdots \\ \frac{\partial f^{(i)}_{AoD,2m}}{\partial x} & \frac{\partial f^{(i)}_{AoD,2m}}{\partial y} & \frac{\partial f^{(i)}_{AoD,2m}}{\partial z} \\ \frac{\partial f^{(i)}_{TDoA,2}}{\partial x} & \frac{\partial f^{(i)}_{TDoA,2}}{\partial y} & \frac{\partial f^{(i)}_{TDoA,2}}{\partial z} \\ \vdots & \vdots & \vdots \\ \frac{\partial f^{(i)}_{TDoA,m}}{\partial x} & \frac{\partial f^{(i)}_{TDoA,m}}{\partial y} & \frac{\partial f^{(i)}_{TDoA,m}}{\partial z} \end{bmatrix}. \tag{3.11}$$

Substituting this into the system gives the linearized update:

$$\mathbf{D}^{(i)}\left(\mathbf{u}-\mathbf{u}^{(i)}\right)+\mathbf{n}=\mathbf{b}^{(i)}, \tag{3.12}$$

where $\mathbf{b}^{(i)}=\mathbf{r}-\mathbf{f}(\mathbf{u}^{(i)})$ is the difference between observations and the modeled values at iteration i.

3.4.2 Gauss-Newton Process

A Minimum Variance Unbiased (MVU) estimator exists if the error vector $\mathbf{n}$ has a Gaussian PDF with zero mean and covariance matrix $\mathbf{C}$ [55]. The update step for $\mathbf{u}$ is given by [56]:

$$\mathbf{u}-\mathbf{u}^{(i)}=\left(\mathbf{D}^{(i)T}\mathbf{C}^{-1}\mathbf{D}^{(i)}\right)^{-1}\mathbf{D}^{(i)T}\mathbf{C}^{-1}\mathbf{b}^{(i)}. \tag{3.13}$$

Thus, the iterative Gauss--Newton update is

$$\mathbf{u}^{(i+1)}=\mathbf{u}^{(i)}+\left(\mathbf{D}^{(i)T}\mathbf{C}^{-1}\mathbf{D}^{(i)}\right)^{-1}\mathbf{D}^{(i)T}\mathbf{C}^{-1}\mathbf{b}^{(i)}. \tag{3.14}$$

The covariance matrix $\mathbf{C}$ reflects measurement reliability, depending on LOS/NLOS identification. After beam determination, the channel impulse response power of the l-th TRP and its m-th path is denoted $\Lambda^2_{l,m}$. The test statistic for the first path is

$$u_l=\frac{\Lambda^2_{l,1}}{\sum_{m=1}^{N_m}\Lambda^2_{l,m}}, \tag{3.15}$$

and LOS is assumed if $u_l>\gamma$, with $\gamma=0.5$ giving the best trade-off between NLOS detection and false alarm. Accordingly,

$$C^{-1}_{l,l}=F(u_l)=\begin{cases}1 & \text{if } u_l>\gamma,\\ 0 & \text{if } u_l\le\gamma.\end{cases} \tag{3.16}$$

The updated ((3.14)) converges after a few iterations starting from an initial guess $\mathbf{u}^{(0)}$, and the final estimate $\mathbf{u}^{(i+1)}$ is used as the UE position.

3.5 Simulation Setup

To evaluate the proposed algorithm's performance, we created a simulation environment in Matlab, based on the 3gpp standard indoor scenario with a map-based channel [57], which

represents a $60m \times 120m \times 10m$ factory hall.
8 gNBs with known locations are installed above the clutter, which improves the availability of LOS. There are 12 metal clutter items with various dimensions, scattered on the ground. The clutter may block the LOS between the gNBs and the UE, as well as reflect the DL rays. UE can have a random horizontal position with a standard height of 1.5 m. Each of the gNBs transmits the DL-PRS with the configuration in table 3.1. To show the effect of transmitter antenna array size on the final positioning result, two different sizes of 2×2, and 4×4 are used.

Parameter	**Value**
Channel model type	InF (Indoor Factory)
Factory size	60x120x10
DL-PRS (carrier frequency, bandwidth)	26 GHz, 400MHz
Sub-carrier spacing	120 KHz
Total gNB TX power	24 dBm
gNB antenna configuration 1	2x2, dz = dy = $\lambda_c/2$
gNB antenna configuration 2	4x4, dz = dy = $\lambda_c/2$
gNB antenna radiation pattern	single sector, vertical
gNB antenna height	8 m
UE antenna configuration	Single element
UE antenna radiation pattern	omni-directional
UE antenna height	1.5 m
numBeams	4 or 16
PRSResourceSetPeriod	numBeams
NumRB	264 (400 MHz)
NumPRSSymbols	12 per slot
CombSize	12
NPRSID	[0,4095]
REOffset	NPRSID - 1

Table 3.1: Simulation parameters

3.5.1 Propagation Model

Our propagation model consists of a deterministic and a probabilistic part. First, we compute the delays and average amplitudes of all the multi-path components based on a site-specific ray-tracing model. Second, we use these parameters in a Clustered Delay Line (CDL) channel model to generate multiple instances of the channel.

3.5.1.1 Ray Tracing

This method employs ray tracing to display and compute propagation pathways with surface geometry provided by the 'Map' attribute. Each displayed propagation path is color-coded according to the received power (dBm) or path loss (dB) along the path. The ray tracing analysis includes surface reflections but does not include effects from diffraction, refraction, or scattering

3.5.2 Channel Model

To obtain the channel-impaired signal we pass the transmit signal through a Clustered Delay Line (CDL) MIMO link-level fading channel. CDL-delay profile is configured using the ray-tracing

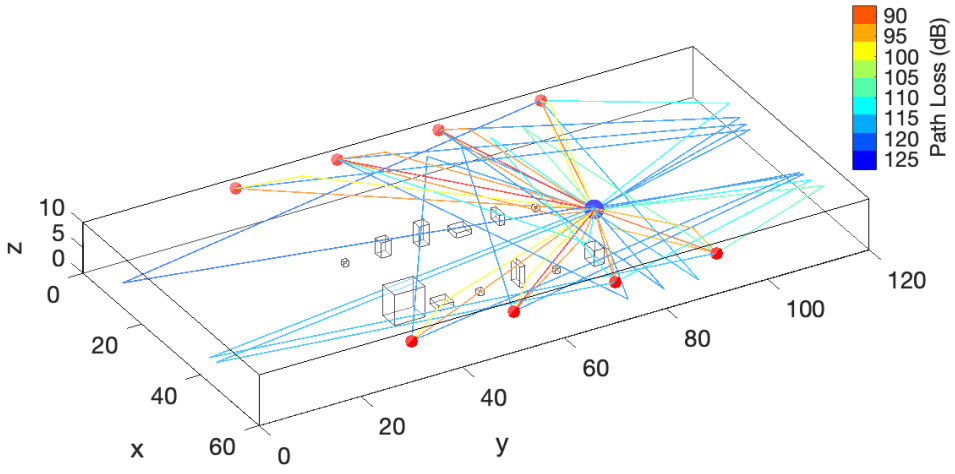

Figure 3.3: Factory hall simulation environment

propagation model outputs, including path delay and path gain, angle of departure, and arrival. The first path follows a Ricean fading distribution, which can point to LOS, and the other paths follow a Rayleigh fading distribution coming from multipath propagation.

3.6 Results

Figures 3.4 and 3.5 demonstrate the Cumulative Distribution of horizontal and vertical error for 200 randomly chosen user locations. TDoA and AoD positioning methods were employed both independently and jointly. As the results reveal, TDoA may achieve satisfactory horizontal precision, whereas AoD leads to proper vertical accuracy. The joint position estimation approach, on the other hand, produces a precise estimation of user coordinates in both directions. The graphs also show how a bigger antenna array enhances accuracy. This improvement is due to more beams produced by a bigger antenna array, as well as enhanced transmitter angle coverage and beamforming.
Table 3.2 presents an analytical comparison between two positioning results based on Horizontal Root Mean Square Error (HRMSE) and Vertical Root Mean Square Error (VRMSE), where P is the number of user positions in simulations. In this chapter, $P = 200$. Despite the mean squared error for vertical and horizontal being less than 1m in multi-antenna configurations, a larger antenna array enhances accuracy even further.

$$\text{HRMSE} = \sqrt{\frac{1}{P}\sum_{p=1}^{P}\left(\text{HPE}_p^2\right)}, \text{VRMSE} = \sqrt{\frac{1}{M}\sum_{p=1}^{P}\left(\text{VPE}_p^2\right)} \tag{3.17}$$

Methods and configurations	**HRMSE** [m]	**VRMSE** [m]
TDoA, Single TX antenna	1.8814	7.7363
AoD, 4×4 TX array	2.8754	0.4571
Joint TDoA-AoD, 2×2 TX array	0.4721	0.8119
Joint TDoA-AoD, 4×4 TX array	0.2909	0.5577

Table 3.2: RMSE comparison

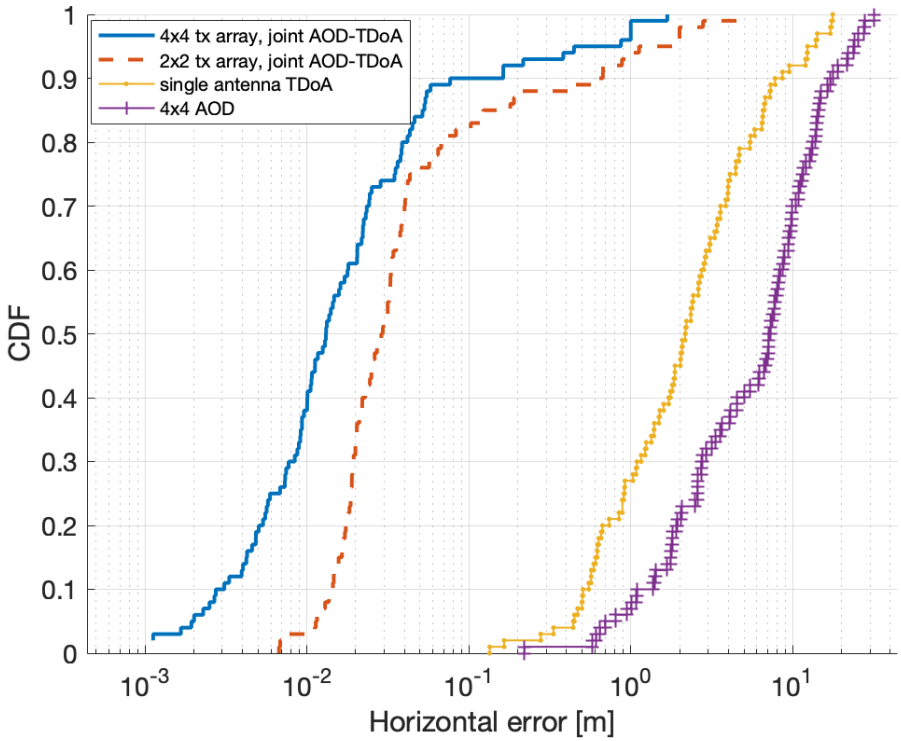

Figure 3.4: Horizontal positioning error

3.7 Conclusions

In this chapter, we derived a joint DL-AoD and DL-TDoA positioning algorithm for UE self-position estimation in 3GPP 5G NR release 16 mm-wave systems. The algorithm exploits the newly introduced possibility to broadcast assistance data to the UE that includes information about the exact location of the antennas and the angles of departure corresponding to different beam indices. The DL TDoA estimation exploits the DL-PRS, while the DL AoD is deduced from the index of the serving beam at the gNB. The proposed algorithm uses a LOS/NLOS link classification to filter out NLOS measurements that have a negative impact on the estimation performance. Simulations are carried out by a ray-tracing propagation model in an InF-H map-based channel model. We show that in a mm-wave scenario with 8 gNBs each using $4 \times 4 = 16$ element antenna array and 400MHz of channel bandwidth, the presented joint AoD-TDoA algorithm can achieve horizontal accuracy of <1m in 99% of the cases and <10cm in 90% of the cases.

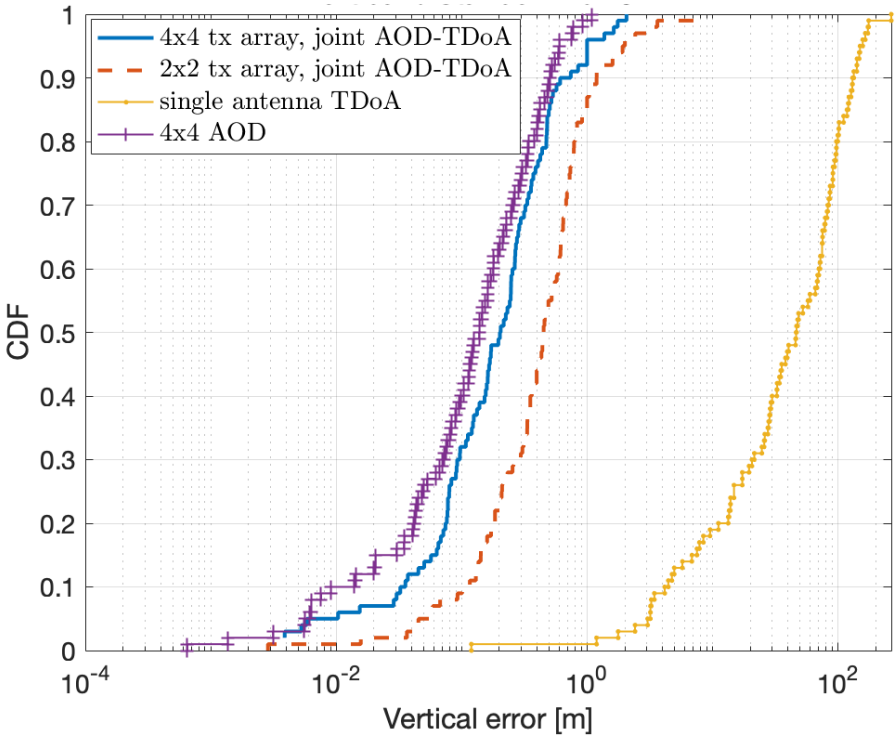

Figure 3.5: Vertical positioning error

Chapter 4

5G NR UL SRS TDoA Positioning by OpenAirInterface

After reviewing fundamentals of position estimation and standard 3GPP methodologies in the previous chapter, this chapter presents a proof-of-concept 5G NR positioning system implemented on the OAI RFsimulator. The essential components of a 3GPP standard positioning architecture are emulated as software in this work. Moreover, a position estimation algorithm based on PSO using UL-TDoA of SRS is implemented and compared with the conventional linear and non-linear least square methods. To build this PoC, our positioning algorithm is running on an emulation of LMF based on a Matlab environment that interacts with an emulation of the NRPPA protocol based on MQTT.

4.1 Introduction

As discussed in the previous chapter, mobile device location information enables numerous applications such as Industry 4.0 and IoT [58]. Since GNSS is unreliable in indoor scenarios, 5G NR Stand Alone (SA) capabilities combined with the standardized 3GPP Release 16 positioning architecture [59, 60] provide the basis for accurate localization. This architecture introduces the LMF and NRPPa signaling between gNBs and the core, supporting standardized collection of measurements such as DL-AoD and DL-TDoA from multi-TRP gNBs and mmWave resources [48], which highlights the importance of a common framework for interoperability and advancement of positioning systems.

This chapter takes the first steps to implement an OAI-based end-to-end prototype of a 5G NR positioning system and validates it on the OAI RFsimulator. For this, UL-SRS from an OAI UE is transmitted to multiple OAI gNBs. After channel estimation and peak detection, peaks and TRP locations are transferred to an emulated LMF in the Matlab environment via MQTT, acting as NRPPa. At the LMF, we propose a PSO-based solver for the nonlinear and non-convex TDoA positioning equations. This heuristic global search requires only the minimum number of LoS TRPs, converges rapidly, and enables real-time estimation. Evaluations on the RFsimulator with a hybrid geometry-based stochastic channel model show that PSO achieves 1 m accuracy in 80–90% of cases in FR1 and sub-meter RMSE with the minimum number of LoS TRPs. A demonstration of this prototype is provided at the end of the results section.

Several approaches have been proposed to solve non-linear and non-convex positioning equations at the LMF, including Maximum Likelihood Estimation (MLE), Semi-Definite Programming (SDP) [61], Second-Order Cone Programming (SOCP) [62], Extended Kalman Filtering (EKF) [63], and Particle Filtering (PF) [64], each with limitations in complexity, initialization, or

non-linearity handling. Related works on 3GPP-compliant implementations include simplified OAI-based multilateration [65], hybrid TDoA-fingerprinting for indoor scenarios [66], and an LMF aligned with 3GPP specifications [67], though these studies do not yet integrate advanced solvers or show performance within the OAI RAN.

4.2 OAI RFsimulator-Based 5G NR positioning prototype

4.2.1 Network Environment: OAI RFsimulator

OAI is an open-source software platform that provides a complete implementation of the 5G Radio Access Network (RAN) protocol stack. It is designed to be flexible, modular, and adaptable to a wide range of use cases and deployment scenarios. The platform includes software components that implement the physical layer (PHY), medium access control (MAC), radio resource management (RRM), and higher-layer protocol stack functions. RFsimulator is a software module within the OAI5G platform that simulates the behavior of the 5G radio frequency (RF) front end. It is a key component of the OAI5G system, as it enables researchers and developers to simulate the behavior of various RF parameters, such as carrier frequency, bandwidth, noise figure, and amplifier gain, without the need for physical hardware. In this work, nrUE and multiple gNBs with single TRPs can be simulated in the RFsimulator to transmit and receive UL-SRS over different available channel models. For each UL transmission, one slot containing SRS symbols is received on multiple gNBs simultaneously, which models the tight synchronization assumption among them. This can be verified by logging the equal peaks of the CIR on each gNB.

4.2.2 UE Mobility: OAI Telnet Server

Telnet server refers to a server that enables interaction with the OAI software components to configure parameters, monitor network performance, and perform various administrative tasks. Since it is possible to modify the channel time offsets corresponding to each UE-gNB pair by the telnet server, arbitrary UE positions in the network can be modeled. A simple script containing random UE positions and selected gNB coordinates enables the telnet server to change each gNB-UE channel time offset accordingly in RFsimulator. On each gNB, this can be observed as different impulse response peaks in the time domain, which account for the signal's ToAs. Each ToA is sent from OAI gNBs to the Matlab environment acting as the LMF using the MQTT protocol acting as NRPPA.

4.2.3 Emulating NRPPa

NRPPA transfers gNB channel estimations to the LMF, as well as useful information such as gNB's TRP coordinates that are assumed to be known for solving the positioning equations in LMF. The estimated position information can also be transmitted to the UE. Since the standard NRPPA is currently under development at EURECOM, here for the proof of concept, we use MQTT (Message Queuing Telemetry Transport), which is a lightweight messaging protocol designed for IoT and M2M (machine-to-machine) communication. It is designed to be simple, efficient, and reliable, and can be used over a range of network transports, including TCP/IP, Bluetooth, and other wireless networks. MQTT is based on a publish/subscribe messaging model, where clients (or devices) can publish messages to topics, and other clients can subscribe to those topics to receive the messages. This protocol consists of two main components: the broker and the clients. The broker is a server that acts as an intermediary between the publishers and

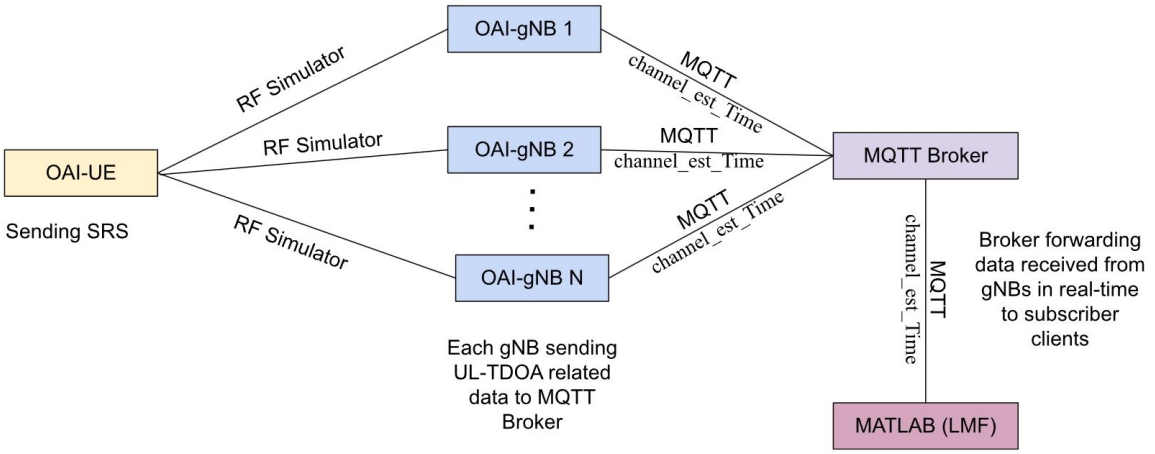

Figure 4.1: Proposed network and protocol diagram

the subscribers. It receives all messages from the publishers and routes them to the subscribers based on their subscriptions. Here, the UE acts as the server while multiple gNBs are subscribed to the "Channel Estimation" topic over a broker server that forwards the channel estimations containing ToAs from OAI gNBs to LMF in Matlab.

4.2.4 Emulating LMF

LMF refers to the collection of network functions in 3GPP standards that are responsible for estimating and tracking the position of mobile devices inside a cellular network. Since LMF was not integrated into OAI at the time of this work, we imitated its functionality and estimated the UE's position in the Matlab environment. In the UL-TDoA positioning method, the UE position is estimated based on multiple UL-ToA measurements from a UE on different gNBs along with other configuration information. To obtain UL measurements, the gNB needs to know the characteristics of the SRS signal transmitted by the UE for the period required to perform the UL measurement. These characteristics should be static over the periodic transmission of SRS during the UL measurements. Hence, the LMF requests the serving gNB to direct the UE to transmit SRS signals for UL positioning. It is up to the serving gNB to make the final decision on resources to be assigned and to communicate this SRS configuration information back to the LMF so that the LMF can forward the SRS configuration to the gNBs. The current OAI code does not support all the functionalities of LMF and localization-related protocols. Therefore, we adopted several simplifications and developed our prototype shown in Figure 4.1 to replicate the real functionalities described above.

4.3 Signal and System Model

4.3.1 TDoA Estimation with Oversampling

Given an SRS received at a gNB, let $\mathbf{y}$ denote the received frequency-domain vector, $\mathbf{x}$ the transmitted SRS symbols, and $\mathbf{w}$ the Channel Frequency Response (CFR), each of length N_{FFT}. The received signal model is

$$\mathbf{y} = \mathbf{w} \odot \mathbf{x} + \mathbf{n}, \tag{4.1}$$

where $\odot$ denotes element-wise multiplication and $\mathbf{n}$ is Additive White Gaussian Noise (AWGN). The LLS estimate of the CFR is

$$\hat{\mathbf{w}} = \frac{\mathbf{y}}{\mathbf{x}}, \tag{4.2}$$

To obtain a fine ToA estimate, an over-sampled inverse discrete Fourier transform (IDFT) of order L is applied with zero-padding:

$$\hat{\mathbf{h}} = \mathrm{IDFT}\Big([\hat{\mathbf{w}}(0 : \tfrac{N_{\mathrm{FFT}}}{2} - 1),\ \mathbf{0}_{1\times(L-1)N_{\mathrm{FFT}}},\ \hat{\mathbf{w}}(\tfrac{N_{\mathrm{FFT}}}{2} : N_{\mathrm{FFT}} - 1)]\Big), \tag{4.3}$$

where $\hat{\mathbf{h}}$ is the over-sampled CIR of length LN_{FFT}.

The ToA at the k-th gNB is estimated by locating the strongest CIR peak:

$$\hat{\tau}_k = T_s \cdot \arg \max_{0\le n<L(N_{\mathrm{FFT}}-1)} |\hat{\mathbf{h}}_k[n]|, \tag{4.4}$$

where $T_s = 1/(N_{\mathrm{FFT}} \cdot \mathrm{SCS})$ is the sampling period. Since no common reference time exists between UE and gNBs, the K ToAs are converted to $K-1$ TDoAs by selecting the first gNB as reference:

$$\Delta\tau_{k,1} = \hat{\tau}_k - \hat{\tau}_1, \qquad k = 2, \ldots, K. \tag{4.5}$$

4.3.2 System Model

Let $\mathbf{u} = (x, y)$ denote the UE coordinates. For K gNBs with known positions $\mathbf{x}_k = (x_k, y_k)$, the range from the UE to gNB k is

$$d_k = \|\mathbf{u} - \mathbf{x}_k\|_2. \tag{4.6}$$

With gNB 1 as the reference, the TDoA equations are

$$f_{TDoA,k}(\mathbf{u}) = d_k - d_1, \qquad k = 2, \ldots, K. \tag{4.7}$$

The UE position is obtained by minimizing the squared error between the measured and modeled distance differences:

$$\mathcal{L} = \sum_{k=2}^{K} \Big(\hat{d}_{k,1} - (\|\mathbf{u}_p - \mathbf{x}_k\|_2 - \|\mathbf{u}_p - \mathbf{x}_1\|_2)\Big)^2, \tag{4.8}$$

where $\hat{d}_{k,1} = c\hat{\Delta\tau}_{k,1}$ and c is the speed of light.

4.4 PSO Position Estimation on LMF

PSO solves the positioning non-linear equations from the previous section by employing a population of particles (swarm) in a D-dimensional search space [68]. Unlike other approaches that linearize equation (4.7), which may introduce extra noise in the position estimate, PSO directly minimizes the non-linear cost function.

Each particle $p \in \{1, \ldots, P\}$ represents a candidate UE position and is constrained within the bounding box defined by the antenna coordinates or testing area. At each iteration i, the velocity and position of particle p are updated as

$$\mathbf{v}_p^{(i+1)} = w\mathbf{v}_p^{(i)} + c_1 r_1(\mathbf{u}_p^{\mathrm{local}} - \mathbf{u}_p^{(i)}) + c_2 r_2(\mathbf{u}^{\mathrm{global}} - \mathbf{u}_p^{(i)}), \tag{4.9}$$

$$\mathbf{u}_p^{(i+1)} = \mathbf{u}_p^{(i)} + \mathbf{v}_p^{(i+1)}, \tag{4.10}$$

Parameter	Value
Channel Model	Ricean
Scenario	Indoor Factory Hall LoS
Simulation Size	$120m \times 60m \times 10m$
Carrier frequency	3.3 GHz
Sub Carrier Spacing	30 KHz
Number of PRBs 1	106
Number of PRBs 2	272
Sampling rate 1	61.44×10^6 Sample/sec
Sampling rate 2	122.88×10^6 Sample/sec
number of gNBs	$3, 4, 6, 8$
number of random UE positions	200

Table 4.1: Simulation configuration details

where $\mathbf{u}_p^{(i)}$ and $\mathbf{v}_p^{(i)}$ are the position and velocity of particle p, $w = 0.9$ is the inertia weight, $c_1 = 0.5$ and $c_2 = 0.9$ are acceleration coefficients, and $r_1, r_2 \sim U(0, 1)$ are uniform random numbers. $\mathbf{u}_p^{\text{local}}$ is the best position found by particle p, and $\mathbf{u}^{\text{global}}$ is the best position found by the swarm. The estimated UE position is given by $\mathbf{u}^{\text{global}}$ at the final iteration.

Algorithm 4.1 Particle Swarm Optimization (PSO) Algorithm

```
Initialize particles with random positions and velocities
Initialize the global best position u^global and cost L from (4.8)
while termination condition not met
    for all particles do
        Update particle's velocity using (4.9)
        Update particle's position using (4.10)
        Evaluate particle's cost L_p
        if L_p < L then
            Update u^global ← u_p^(i+1)
            Update L ← L_p
        end if
    end
end
Output: Best position u^global and corresponding cost L
```

4.5 Simulations and Results

To test the accuracy of the proposed positioning algorithm on LMF, UL SRS from 200 random UE positions are transmitted and their ToA on multiple gNBs are estimated on RFsimulator with the *phy-test* mode. The measurements are transferred to LMF and converted to TDoA to be used in PSO. Two different SRS configurations are used with 106 and 272 Physical Resource Blocks (PRBs), which give 61.44×10^6 samples/sec and 122.88×10^6 samples/sec, respectively. The details of signal and simulation configurations are presented in table 4.1.
Figure 4.2 compares the PSO positioning accuracy to the NLS solved by the Gauss-Newton's method[69] that is initialized by a LLS coarse estimation by UL TDoA measurements from the

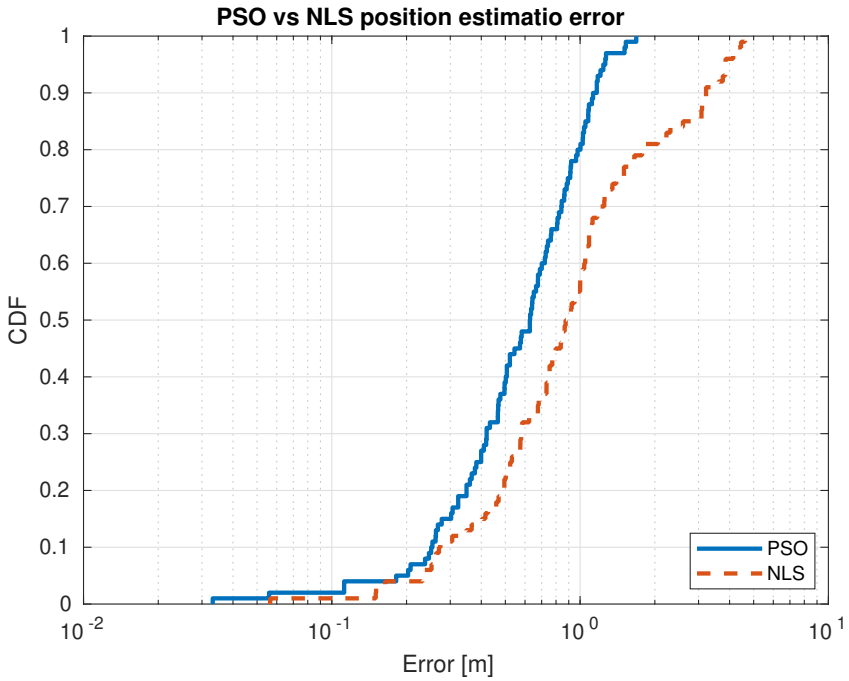

Figure 4.2: 4gNB PSO and NLS position estimation error

minimum number of LoS gNBs ($K = 4$) to have a unique solution. This shows that in the case of only a few LoS links available, PSO, as a stochastic optimization solution, overcomes the non-linearity and non-convexity of position equations better than the others. While conventional methods, either non-linear like WLS, NLS, EKF, or linear like LLS require initialization from GPS or a redundant number of links, PSO outperforms them in estimation error by utilizing a population of points in the search space to converge to the global minimum. Simulation results give $RMSE_{NLS} = 1.7047$ and $RMSE_{PSO} = 0.7463$ which shows a significant improvement.
Although with 3 gNBs and 2 TDoA measurements, the 2D position estimation is theoretically possible in many cases, according to the geometry of the problem, since three hyperbolae may intersect in two points, it can be shown that a unique solution for the position equations requires at least 4 gNBs in the TDoA method [70]. The results from adding redundant gNBs validate this in figure 4.3, where the 3 gNB setup has a major error difference in comparison to 4, 6, and 8 gNBs.
Finally, results from figure 4.4 confirm the fact that utilizing a larger signal BW to have a higher sampling rate gives a better TDoA estimation that ends up improving the UE position estimates significantly. A video demonstrating how OAI rfSimulator works with 4 gNBs and a UE, and how LMF on Matlab performs position estimation based on TDoAs, is available on this URL: `https://drive.google.com/file/d/1_C8lk3Yr27INYVdLomFUTELu3g5C2tK9/view?usp=sharing`

4.6 Conclusions

In this chapter, we derived an UL-TDoA position estimation system using the PSO method on OAI, which is a 5G NR 3GPP release 16 compliant software. The algorithm measures an accurate TDoA of SRS by oversampling from a nrUE with an unknown position to multiple synchronized gNBs with known positions and sends this information from gNBs in OAI to the LMF model implemented in Matlab using the MQTT protocol to act as NRPPA that shows

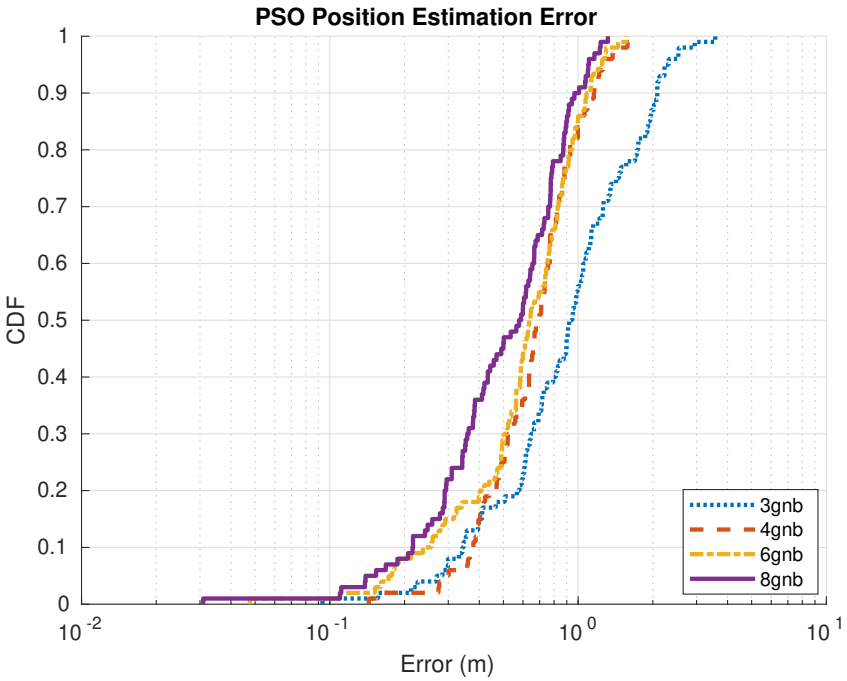

Figure 4.3: Positioning Improvement by redundant gNBs

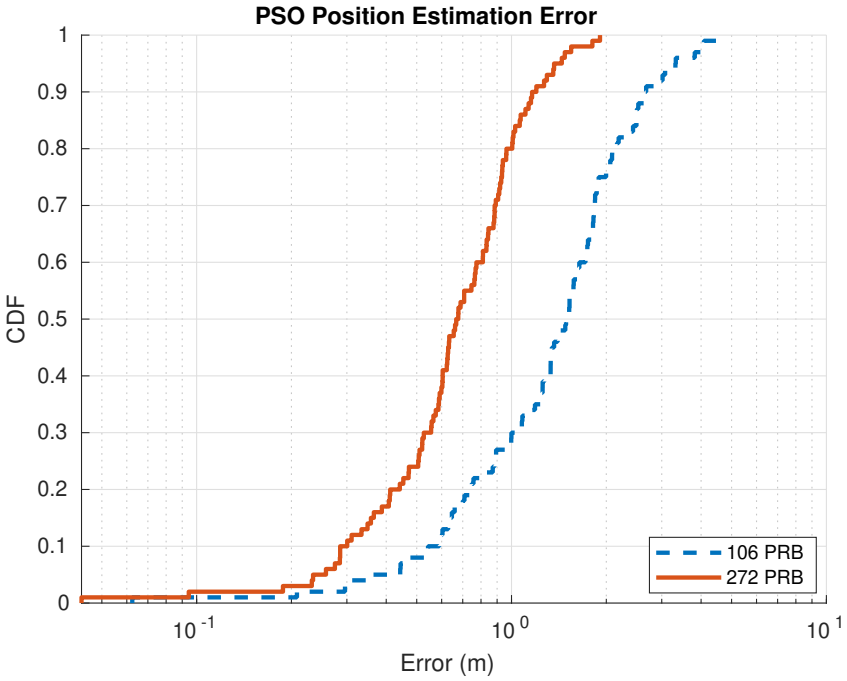

Figure 4.4: 4gNB with 106 and 272 PRB SRS configuration error

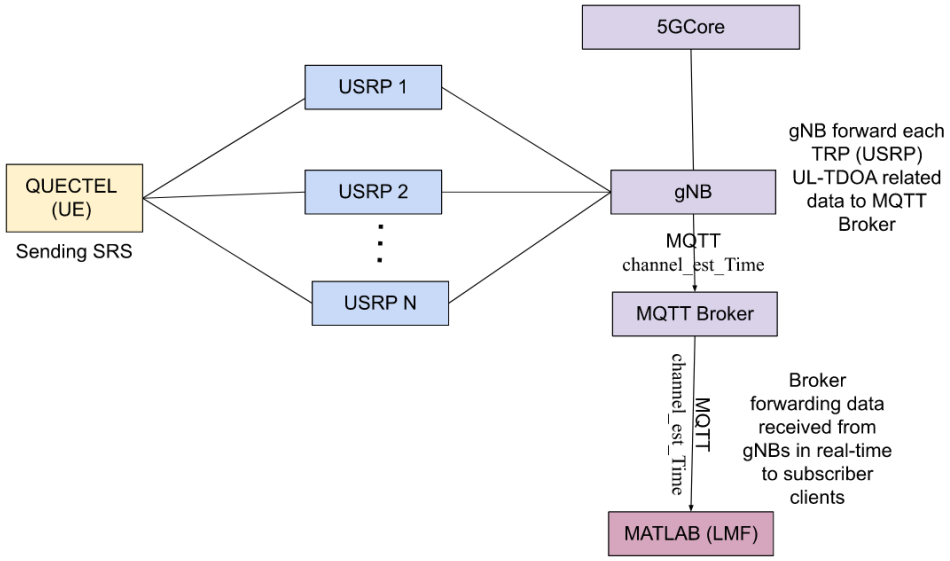

Figure 4.5: 4 USRP setup diagram

the standard behaviour of an online positioning system. The simulations carried out on OAI RFsimulator show that the PSO position estimation performance using the minimum number of LoS gNBs without GPS initialization or error statistics can achieve around 1-meter accuracy in 90% of cases.

Chapter 5

Experimental Insights From OpenAirInterface 5G Positioning Testbeds: Challenges and Solutions

After validating the end-to-end performance of our UL TDoA method on OAI RFsimulator, this chapter presents the contributions to the integration of a standard-compliant LMF to the OAI's 5G Core Network, besides the integration of the standard NRPPA procedures to the OAI's gNB and CN. Our LMF contains a positioning pipeline for the UL TDoA method that is tested on three testbeds in both outdoor and indoor factory hall scenarios. Multiple ToA and TDoA filters, as well as a position estimation algorithm, are designed to cover for the measurement noises as well as the synchronization impairments to achieve a desirable accuracy.

5.1 Introduction

In our previous work [71], we presented an open-source implementation of the new NRPPA [72] together with an LMF [73] running on OAI. OAI provides an open source implementation of the 5G protocol stack for the RAN and CN components [74]. We validated the end-to-end procedure for UL TDoA positioning, using an O-RAN–compliant testbed, including a mobile phone serving as UE and commercial O-RAN RUs.

In this paper, we present a complete positioning pipeline implemented on the OAI LMF, which includes filtering of ToA and TDoA measurements using empirical and geometric criteria, and a PSO-based position estimation algorithm. We evaluated its performance on three diverse testbeds: the outdoor GEO-5G testbed at EURECOM, and two indoor industrial sites at STELLANTIS' Mattern Lab and the Airbus factory hall. These environments pose distinct challenges, such as synchronization impairments in outdoor setups with widely distributed RUs, and severe multipath and NLoS conditions indoors. Our PSO-based estimator is designed to handle timing offsets in multi-RU deployments, while the ToA and TDoA filters help to discard unreliable measurements. We also introduce a beyond-3GPP framework for evaluating a data-driven positioning within the O-RAN framework, using CIR as input to improve robustness in challenging scenarios. The results demonstrate 1–2 meter accuracy in 90% of the cases in all testbeds. An extensive data set comprising measured CIRs, precise timestamps, and corresponding position labels is published alongside this work.

Looking at the literature, there are a range of studies investigating positioning capabilities on the OAI platform, utilizing various techniques and setups. For example, earlier work has

presented tools and initial frameworks to support positioning in OAI [75, 76], explored E-CID mechanisms [77], and proposed PRS-based hybrid GNSS and 5G NR downlink positioning for both UAVs and terrestrial gNBs [78]. Other research has focused on improving the accuracy of the RTT estimation [79], implementing fingerprinting approaches based on RSRP measurements [80], and evaluating sidelink-based localization strategies [81]. More experimental studies include a single-link testbed that emulates a multinode TDoA setup using software-defined radios (SDRs) [82]. Despite these contributions, to the best of our knowledge, our work is the first to report positioning results from a fully open-source, 3GPP-compliant implementation on OAI, including both OAI RAN and CN components, including LMF. Furthermore, our framework has been validated on commercial RUs in various environments, demonstrating its readiness for practical deployment. This chapter presents the signal processing methods and experimental outcomes from these deployments.

5.2 OAI Positioning System Model

We deploy 5G SA networks using OAI gNBs and CN, following a disaggregated O-RAN architecture (split option 7.2) with CU, DU, and multiple RUs per gNB. Each RU is equipped with multiple fixed antennas and synchronized via PTP using a Grandmaster clock over the GNSS, achieving nanosecond-level timing precision. A UE with fixed height moves in $t \in \{1, T\}$ timestamps with unknown position $\mathbf{u}_t \in \mathbb{R}^3$, always bounded within the convex frame of M antennas each having known location $\mathbf{x_m} \in \mathbb{R}^3$. At each timestamp, the UE transmits UL Sounding Reference Signal (SRS), received by antennas. The system operates under Orthogonal frequency-division multiplexing (OFDM) with N_{fft} subcarriers. The CIR vector $\mathbf{h}_{m,t}$ is computed via IDFT from the estimated CFR vector $\mathbf{w}_{m,t}$. The ToA of the signal at antenna m and time index t is estimated as the delay corresponding to the strongest multipath component, identified by the peak magnitude of the CIR vector. Specifically, the ToA in seconds is given by:

$$\tau_{m,t} = T_s \cdot \arg\max_n |\mathbf{h}_{m,t}[n]|\,, \tag{5.1}$$

where T_s is the sampling period in second/sample unit. The set of all ToAs and antenna locations are vectorized as $\boldsymbol{\tau}_t \in \mathbb{R}^M$ and $\mathbf{X} \in \mathbb{R}^{M\times 3}$ respectively, and retrieved by the LMF over the NRPPa positioning procedure. To eliminate the UE-side clock offset, the LMF calculates TDoA by differencing ToAs with respect to a reference antenna. These TDoA measurements, along with the antenna coordinates, are used to estimate the UE's position. Details on the TDoA-based estimation framework are presented in Section 5.4.

5.3 Our 5G Positioning Testbeds

Building on the aforementioned principles of the UL-TDoA positioning system model, this section presents three distinct localization testbeds.

5.3.1 GEO5G Outdoor Deployment at EURECOM

The GEO5G testbed is part of EURECOM's Open5G platform, featuring high-speed fiber infrastructure and supporting virtualized 5G with USRPs [83], O-RAN RUs, and OAI. To evaluate OAI's new localization features, we integrated two outdoor O-RAN RUs provided by Firecell [22] from VVDN [84] into the testbed. Our contributions in [71] allow flexible deployment using either single-gNB or multi-gNB configurations with multiple RUs. Antennas

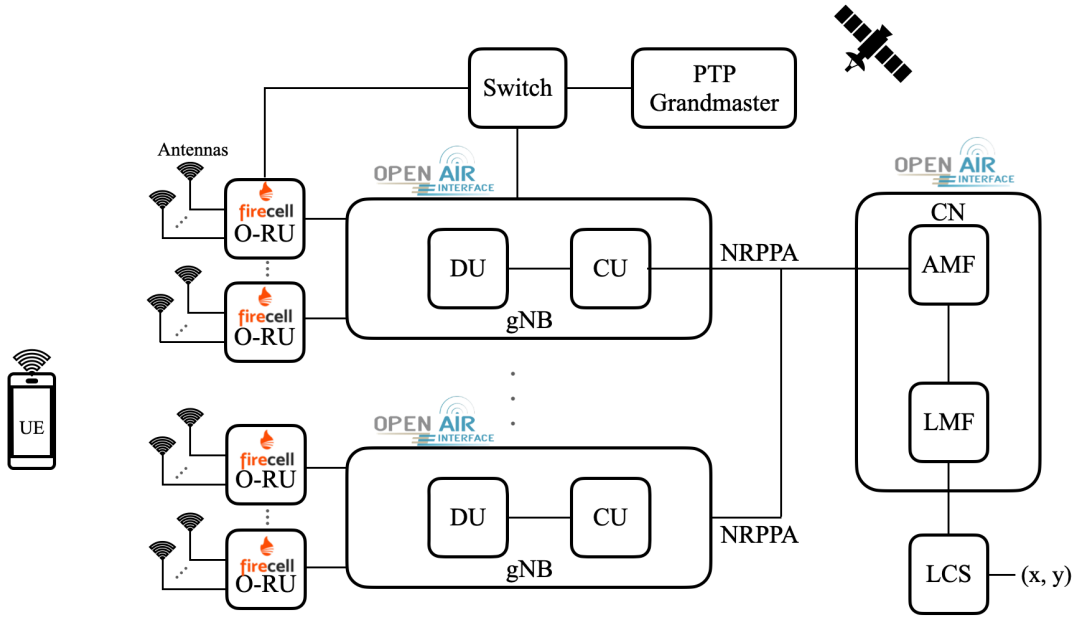

Figure 5.1: System model with OAI CN, multiple OAI gNBs, multiple RUs, and distributed antennas for UL-SRS TDoA positioning

are distributed across RUs and mounted on roof railings using low-loss cables, covering a 50 m×10 m area on EURECOM's north terrace (see Figure 5.2a). Ground truth positions at this testbed are determined using two methods. For static positioning scenarios, where the UE is mounted on a tripod to evaluate optimal performance, 16 test points from A to P in Figure 5.2 are distributed across the testbed. Their precise coordinates are measured using laser equipment by recording distances from each test point to all antennas and computing the positions through geometric triangulation. For a handheld mobile UE that takes a trajectory freely in the testing area, we set up a Real-Time Kinematic (RTK) setup that includes a base GPS module that is steady and a rover GPS module that moves closely with the UE. RTK positioning enables centimeter-level accuracy by using carrier-phase measurements and differential corrections from its base [85]. To convert RTK geographic coordinates from [lat, long, alt] to raw Cartesian coordinates [xEst, yNorth, zUp], we use open-source libraries such as *pymap3d* in real-time on Python. A linear transformation is then applied to align these with our local [x, y, z] coordinate system, with antenna 1 on RU 1 as reference [0,0,2.2]. The testbed follows an O-RAN architecture with synchronization option LLS-C3, using a GNSS-disciplined Qulsar Qg 2 Grandmaster. The CU/DU operates on a high-performance server connected via Cisco switches, while the CN runs in Docker on a separate server. Precise synchronization is critical for TDoA, as 1 ns error translates to 0.3 m inaccuracy. However, due to PTP switch impairments and RU long distances at this testbed, errors up to 40 ns are observed. To mitigate the propagation of clock drift from one RU to the other, we adopt a per-RU reference antenna strategy in calculating TDoAs instead of a common reference across all RUs, ensuring internal consistency and reducing cross-RU time drift. This modification alters the classical TDoA-based positioning, detailed in Section 5.4.

5.3.2 STELLANTIS Indoor Deployment

A similar deployment to EURECOM is installed at STELLANTIS, located in the Mattern lab (Sochaux, France), depicted in Figure 5.2b, with a network architecture similar to Figure 5.1.

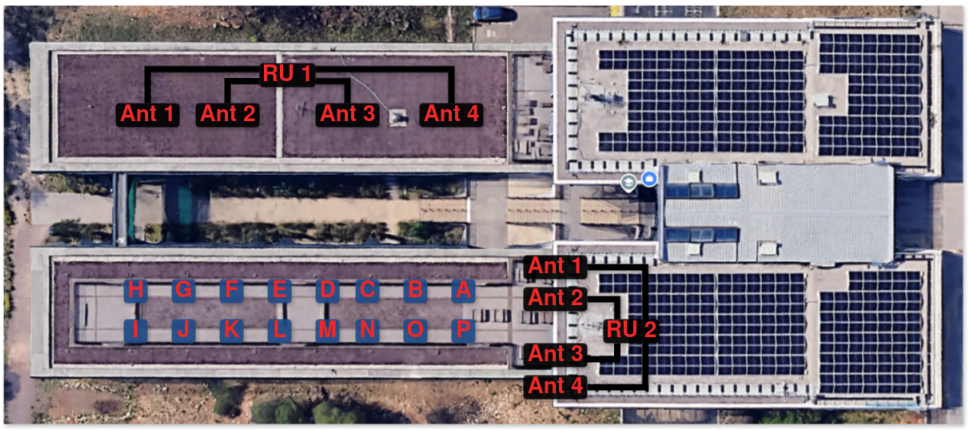

(a) GEO-5G testbed at EURECOM

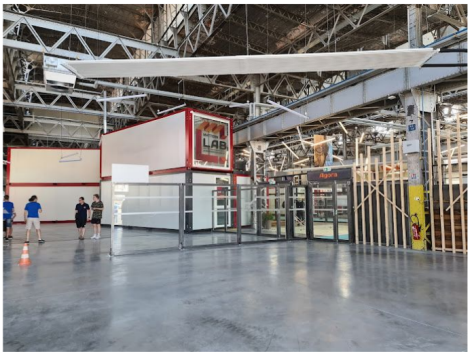

(b) Stellantis testbed

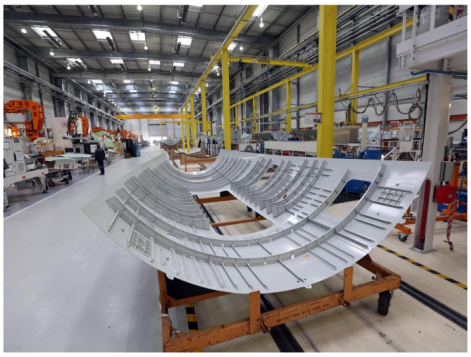

(c) Airbus factory

Figure 5.2: Overview of 5G positioning testbeds

This indoor setup includes 2 gNBs, 4 RUs and 8 antennas, covering a 20 m × 20 m area. While fewer nodes would cover the area, 2 gNBs and 4 RUs were deployed to test both single and multi-gNB configurations at scale. Despite LoS connectivity to all antennas, the small environment and indoor propagation pose challenges for positioning. Multipath components exhibit minimal delay separation, causing closely spaced peaks in the CIR—unlike the more separable multipath in outdoor environments (see Figure 5.3). In literature, super-resolution methods such as MUSIC [86] have been studied for ToA estimation in such dense environments, but their reliance on prior multipath knowledge and high computational cost limit their suitability for real-time tracking applications. In contrast, we propose a low-complexity, low-latency pre-processing step, detailed in Section5.4. While the legacy OAI channel estimation applies interpolation and oversampling before ToA estimation—helping to detect peaks in closely spaced multipath scenarios—we introduce additional ToA and TDoA filtering mechanisms at the LMF. These filters improve positioning robustness without incurring the computational overhead of super-resolution algorithms.

5.3.3 Airbus Factory Hall Deployment

Ultimately, the Airbus Atlantic factory hall in Méaulte, France, is deployed with a similar system model in Figure 5.1 and equipped with 2 gNBs, 4 RUs, and 16 antennas. Figure 5.2c has a sample image of the Airbus factory hall where the antennas are covering an area of

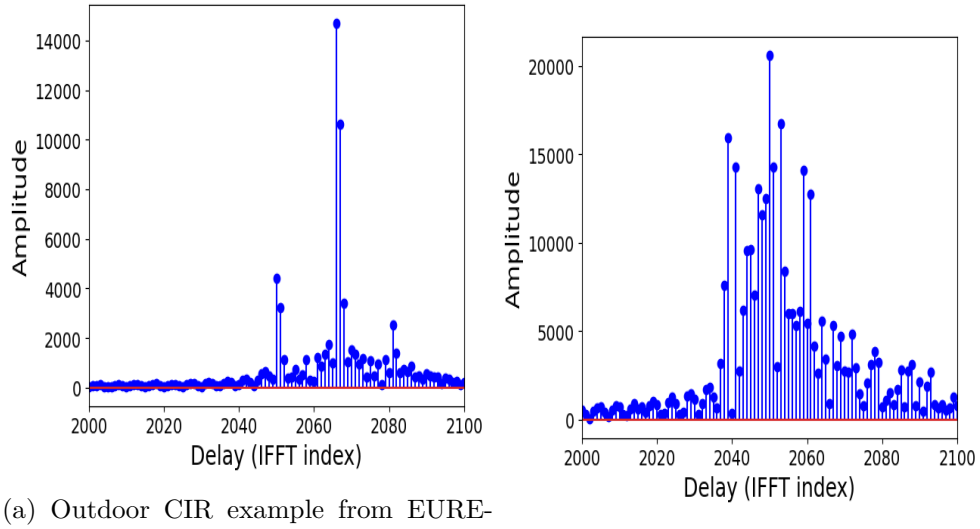

(a) Outdoor CIR example from EURECOM

(b) Indoor CIR example from Mattern lab

Figure 5.3: Outdoor/indoor multipath CIR

100m×50m. However, this deployment faces significant signal quality challenges. The long 50 m cables connecting the antennas to the RUs introduce considerable Signal-to-Noise Ratio (SNR) degradation. Additionally, the presence of large metallic structures and sizable airplane frames under construction further complicates the propagation environment. These obstructions severely limit the availability of LoS conditions, despite the high number of deployed antennas. As a result, the raw received signals and channel estimations are heavily affected by noise and multipath. Ensuring reliable positioning performance in such environments requires specialized measurement filtering techniques. In section 5.4, we introduce a set of filters designed based on the known positions of the antennas and the geometry of the testing area, as well as the delay spread and of favorable signals to suppress noisy or NLoS measurements. While the proposed processing pipeline yields accurate results at some testing points with enough LoS antennas, the TDoA-based method at the Airbus testbed exhibits high localization errors across the majority of the testing area.

To address this limitation, we propose a data-driven method based on Finger Printing, where in a large dataset, each set of CIRs from all antennas is labeled with its corresponding ground truth position calculated by a laser tool. Although this approach is inherently exhaustive and requires significant effort for data labeling and a large volume of training samples, it demonstrates improved positioning reliability compared to the traditional TDoA-based method. By leveraging the power distribution knowledge in LoS/NLoS CIRs, the Finger Printing method, enhanced by the feature extraction capabilities of Convolutional Neural Networks (CNNs), demonstrates greater robustness in complex environments, such as the Airbus testbed. The complete framework and the necessary pre-processing steps enabling the Finger Printing approach are detailed in Section 5.4.3.2

5.4 Position estimation with refined ToA and TDoA

5.4.1 ToA Filtering

Although absolute ToA is not available in our testbeds due to the lack of synchronization between the UE and RUs, an empirical distribution of the channel's delay spread can still be obtained

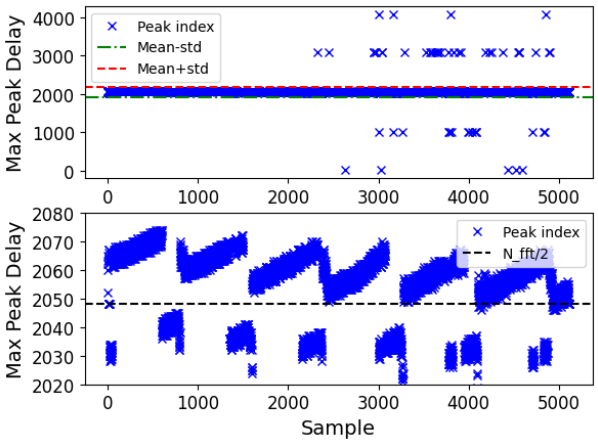

Figure 5.4: Filtering ToAs by statistical bounds based on max peak delay distribution concentrated around $\frac{N_{\text{fft}}}{2}$

by analyzing large CIR datasets. By applying an IDFT to the FFT-shifted CFR, we process CIRs so that dominant peaks typically align around the center index $\frac{N_{\text{fft}}}{2}$. However, we observe that some CIRs exhibit peaks with large offsets, leading to physically implausible TDoA values given the known geometry of the test environment. This is mainly attributed to synchronization impairments that introduce timing jitter. Figure 5.4 shows the distribution of maximum peak locations in the FFT-shifted CIR dataset. The majority of the peaks are concentrated around $\frac{N_{\text{fft}}}{2} = 2048$ while a noticeable portion exhibits significant offsets that indicate outliers.

Therefore, we design a ToA filter that preserves CIRs with peaks falling within the expected delay spread range and discards those with excessive temporal offsets. CIR is modeled as a sum of multipath components, each represented by a delayed Dirac delta function $\delta(.)$ scaled by a complex amplitude α_i, which captures both the attenuation and phase shift of the i-th path.

$$h(t) = \sum_{i=1}^{N_{\text{fft}}} \alpha_i \, \delta(n - \tau_i) \tag{5.2}$$

The delays τ_i correspond to the ToA of each path. To formalize the filtering process, let μ_τ and σ_τ denote the empirical mean and standard deviation of the max-peak delay distribution, respectively. A CIR is retained if its most significant peak τ_{peak} satisfies the condition:

$$\mu_\tau - \sigma_\tau \leq \tau_{\text{peak}} \leq \mu_\tau + \sigma_\tau. \tag{5.3}$$

This range captures typical delay spreads while excluding outliers inconsistent with the environment's propagation.

5.4.2 TDoA Filtering

The geometry between each antenna pair and their direct path to the UE determines whether the TDoA is positive, negative, or zero, depending on the relative positions of the UE and antennas. However, Theorem1 implies that the absolute value of TDoA is bounded regardless of sign.

Theorem 1. *Let points A and B be two antennas and C be a UE, such that the three points A, B, C form a non-degenerate triangle. Denote the distances between the points as $AB = c$,*

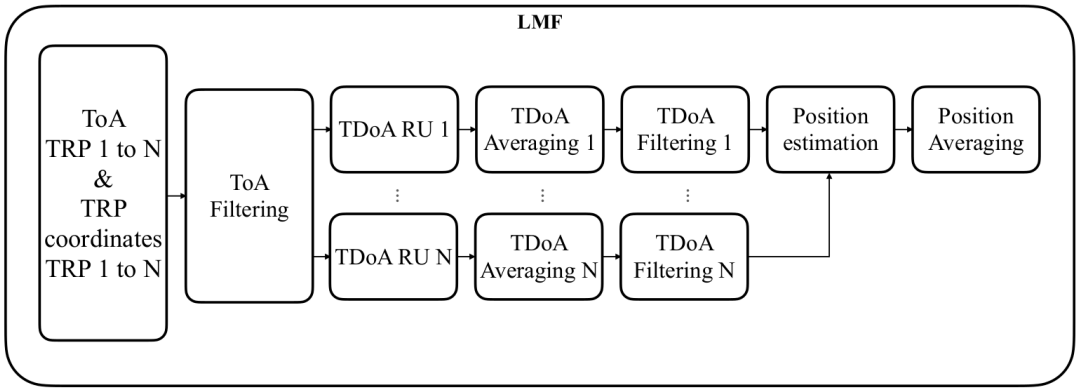

Figure 5.5: Our proposed positioning pipeline at LMF

$AC = b$, and $BC = a$. Then, the absolute difference $|a - b|$ is bounded as:

$$0 \leq |a - b| \leq c, \tag{5.4}$$

where the lower bound is trivial due to the non-negativity of absolute values, and the upper bound follows from the triangle inequality in Euclidean geometry [87]. Equality in the upper bound holds if and only if the points A, B, C are collinear (i.e., the triangle is degenerate).

In our setup with K RUs, each with M_k distributed antennas, we define $\Delta\tau_{k,m}^t$ as the TDoA at time t for the m-th antenna of the k-th RU, relative to a reference antenna within the same RU:

$$\begin{aligned} \Delta\tau_{k,m}^t &= \tau_{k,m}^t - \tau_{k,\text{ref}}^t, \\ &k \in \{1, \ldots, K\}, m \in \{1, \ldots, M_k\}, m \neq \text{ref}. \end{aligned} \tag{5.5}$$

Here, $\tau_{k,m}$ denotes the ToA at the m-th antenna $\mathbf{x}_{k,m}$, and $\tau_{k,\text{ref}}$ represents the ToA at the reference antenna $\mathbf{x}_{k,\text{ref}}$, both associated with the k-th RU. Based on the assumption in our system model, the UE's position is spatially bounded by the convex region of the antennas. In the edge cases where the UE is co-located with one of the antennas, the TDoA becomes

$$\Delta\tau_{k,m}^t(\mathbf{u}_t) = \begin{cases} -\dfrac{\|\mathbf{x}_{k,m} - \mathbf{x}_{k,\text{ref}}\|_2}{v}, & \text{if } \mathbf{u}_t = \mathbf{x}_{k,m}, \\ \dfrac{\|\mathbf{x}_{k,m} - \mathbf{x}_{k,\text{ref}}\|_2}{v}, & \text{if } \mathbf{u}_t = \mathbf{x}_{k,\text{ref}}. \end{cases} \tag{5.6}$$

Therefore, we can write

$$0 \leq |\Delta\tau_{k,m}| \leq \frac{\|\mathbf{x}_{k,m} - \mathbf{x}_{k,\text{ref}}\|_2}{c}. \tag{5.7}$$

Based on the theoretical bounds established in (5.7), from Theorem 1, we define a filtering criterion that systematically discards invalid TDoA values. In particular, this filter is designed to eliminate measurements that fall outside the physically feasible range, which typically arise from noisy conditions or NLoS propagation. By enforcing this constraint, we ensure that only reliable TDoA measurements are retained and passed to the positioning algorithm, thereby improving its robustness and accuracy.

5.4.3 Position Estimation

5.4.3.1 Standard TDoA method on LMF

To estimate the UE position $\hat{\mathbf{u}} = (\hat{x}, \hat{y})$, we define a TDoA-based loss function on the LMF by comparing the measured and expected TDoAs using known antenna coordinates. For a candidate position $\hat{\mathbf{u}}_t$, the loss function is defined as

$$\mathcal{L}(\hat{\mathbf{u}}_t) = \sum_{k=1}^{K} \sum_{m=1}^{M_k} \left(\Delta\hat{\tau}_{k,m}^{n} - \Delta\tau_{k,m}(\hat{\mathbf{u}}_t) \right)^2, \tag{5.8}$$

where $\Delta\hat{\tau}_{k,m}^{n}$ is the measured TDoA and

$$\Delta\tau_{k,m}(\hat{\mathbf{u}}_t) = \frac{\|\hat{\mathbf{u}}_t - \mathbf{x}_{k,m}\| - \|\hat{\mathbf{u}}_t - \mathbf{x}_{k,\text{ref}}\|}{v} \tag{5.9}$$

is the expected TDoA. To minimize this loss, based on the comparisons to state-of-the-art methods in our recent work[88], we employ PSO due to its efficiency and lack of dependence on gradient information, which makes it suitable for real-time applications on resource-constrained LMFs. Unlike gradient search or Least Squares methods in [89] and [90], PSO offers a favorable trade-off between latency and accuracy. Each particle $p \in \{1, P\}$ represents a candidate UE position and is constrained to move within the bounding box defined by the minimum and maximum antenna coordinates or testing area. At each iteration i, the particles' velocity and position are updated as

$$\mathbf{v}_p^{(i+1)} = w\mathbf{v}_p^{(i)} + c_1 r_1(\mathbf{u}_p^{\text{local}} - \mathbf{u}_p^{(i)}) + c_2 r_2(\mathbf{u}^{\text{global}} - \mathbf{u}_p^{(i)}), \tag{5.10}$$

$$\mathbf{u}_p^{(i+1)} = \mathbf{u}_p^{(t)} + \mathbf{v}_p^{(i+1)}, \tag{5.11}$$

where $\mathbf{u}_p^{(i)}$ is the position and $\mathbf{v}_p^{(i)}$ is the velocity of each particle, $w = 0.9$ is the inertia weight, $c_1 = 0.5$, $c_2 = 0.9$ are acceleration coefficients, and $r_1, r_2 \sim U(0, 1)$ are random variables. $\mathbf{u}_p^{\text{local}}$ is the best position found by particle p, and $\mathbf{u}^{\text{global}}$ is the best position found by the swarm. The estimated UE position is given by $\mathbf{u}^{\text{global}}$ at the final iteration. In addition, a moving average filter is applied to the output of the PSO to smooth the UE location estimate. The averaging window size plays a significant role in the latency of the position estimations, as larger windows make the response slower but result in smoother trajectories, while smaller windows reduce latency at the cost of increased noise. By incorporating prior knowledge of the deployment geometry, filtering noisy measurements, and explicitly accounting for hardware impairments in the loss function, the proposed PSO-based method demonstrates robust and reliable performance in real-world positioning testbeds. In Section 7.7, we present the positioning results of the proposed processing pipeline across our various testbed environments.

5.4.3.2 Data-Driven Method by Finger Printing

While TDoA is widely used for positioning, its accuracy drops in NLoS conditions. In contrast, ML-based methods leveraging richer inputs like full CIR have shown better performance in such environments. Although 3GPP NRPPa [72] does not support large-scale CIR transmission, the O-RAN architecture allows forwarding CIR from the CU-DU to the Near-RT RIC via the E2 interface and xApps, enabling the deployment of learning-based positioning approaches.

We present a positioning procedure inspired by the O-RAN framework, where CIR data is offloaded from gNBs to an external host for AI/ML-based inference. Instead of using E2,

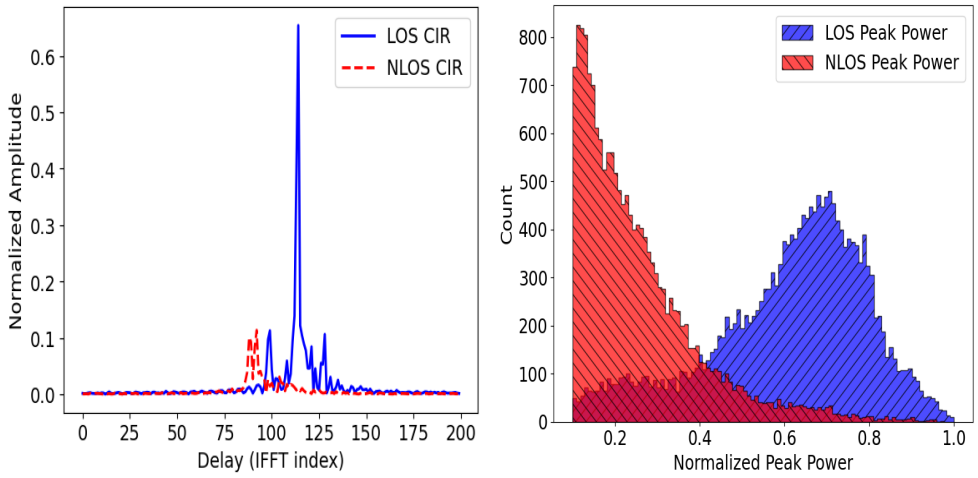

(a) LoS/NLoS sample CIR from testbeds (b) LoS/NLoS max peak power histogram

Figure 5.6: LoS/NLoS power distributions

our implementation relies on the MQTT protocol. Here, each gNB publishes a topic for CIR measurements to an MQTT broker. The broker can reside on a gNB, the CN, or a third server. An AI/ML host subscribes to this topic and collects CIR data in real time. A pretrained Finger Printing model is deployed on this host to infer the UE's position. To enable effective inference, raw CIR is first preprocessed into a format suitable for the Finger Printing model.

Let the matrix $\mathbf{H}_{k,t} \in \mathbb{C}^{M_k \times N_{\text{fft}}}$ be the collection of CIRs received from all M_k distributed antennas of RU k at timestamp t, where each row corresponds to a single antenna's element-wise absolute value of CIR

$$\mathbf{H}_{k,t} = \begin{bmatrix} |\mathbf{h}_{k,1,t}^T| \\ |\mathbf{h}_{k,2,t}^T| \\ \vdots \\ |\mathbf{h}_{k,M_k,t}^T| \end{bmatrix} \in \mathbb{C}^{M_k \times N_{\text{fft}}}. \tag{5.12}$$

On each RU, we compensate for the TDoA between antennas by introducing a peak-based alignment step. Let $\tau_{k,m,t}^{\text{peak}}$ denote the index of the maximum peak in the m-th CIR vector $\mathbf{h}_{k,m,t}$, and an offset index as the earliest peak among all antennas, $\eta_{k,t}^{\text{offset}} = \min_{m \in \{1,\ldots,M_k\}} \tau_{k,m,t}^{\text{peak}}$. This operation shifts the vector to the left and fills the tail with zeros

$$\mathbf{h}_{k,m,t}^{\text{shifted}}[j] = \begin{cases} \mathbf{h}_{k,m,t}[j + \eta_{k,t}^{\text{offset}}] & \text{if } j + \eta_{k,t}^{\text{offset}} < N_{\text{fft}}, \\ 0 & \text{otherwise}, \end{cases} \tag{5.13}$$

resulting in a TDoA-aligned CIR matrix $\mathbf{H}_{k,t}^{\text{shifted}} \in \mathbb{C}^{M_k \times N_{\text{fft}}}$. This procedure, during both training and testing phases, ensures that the CIRs are temporally aligned across antennas of the same RU, thereby respecting the assumption of tight time synchronization among them and the correctness of TDoA. The matrix $\mathbf{h}_{k,t}^{\text{shifted}}$ is further normalized by the maximum peak magnitude observed across the entire training dataset. To form a unified input dimension for model training and testing, CIRs are concatenated from all K RUs along the antenna (row) dimension and

Table 5.1: CNN Embedding Model Architecture Summary

Layer	Output Dimension	Kernel Size	Activation
Conv2D	(32, 16, 100)	(3, 3)	ReLU
Conv2D	(64, 16, 100)	(3, 3)	ReLU
Flatten	(1, 102400)	-	-
Fully Con.	(1, 512)	-	ReLU
Fully Con.	(1, 128)	-	ReLU
Fully Con.	(1, 2)	-	-

truncated to only contain the first C fft indices

$$\mathbf{H}_t^{\text{norm}} = \frac{1}{\alpha_{\text{norm}}}. \begin{bmatrix} \mathbf{h}_{1,t}^{\text{shifted } T} \\ \mathbf{h}_{2,t}^{\text{shifted } T} \\ \vdots \\ \mathbf{h}_{M,t}^{\text{shifted } T} \end{bmatrix} \in \mathbb{C}^{M \times C}, \tag{5.14}$$

where the normalization factor $\alpha_{\text{norm}} = \max_{k,m,t}(\mathbf{h}_{k,m,t}^{\text{shifted}})$ is computed from the training data and reused during testing to ensure consistency. Also, $M = \sum_{k=1}^{K} M_k$ is the total number of antennas across all RUs. To mitigate the impact of NLoS antennas, a binary masking vector $\mathbf{m} \in \{0,1\}^{M \times 1}$ is applied to the normalized CIR input matrix. The masking vector suppresses unreliable antennas by zeroing out the corresponding rows in the input matrix. The masked input $\tilde{\mathbf{H}}_t^{\text{norm}}$ is computed as

$$\tilde{\mathbf{H}}_t^{\text{norm}} = \mathbf{H}_t^{\text{norm}} \odot \mathbf{m}. \tag{5.15}$$

where $\odot$ is element-wise multiplication. It is constructed by comparing the maximum peak magnitude of each normalized CIR (per antenna) against a threshold γ. If the peak exceeds γ, the antenna is considered LoS ($m_i = 1$); otherwise, it is suppressed as likely NLoS ($m_i = 0$). The threshold γ is selected empirically based on analysis of a labeled dataset of both LoS and NLoS CIRs. As illustrated in Figure 5.6a, LoS measurements consistently exhibit stronger peaks than NLoS counterparts. Also, based on the normalized peak power histogram in Figure 5.6b, a threshold of $\gamma = 0.4$ proves to be reliable for distinguishing LoS from NLoS CIR in this dataset. This threshold can be adjusted as needed by analyzing the training data specific to each testbed. Subsequently, a mapping function $f_\theta(\cdot)$, realized by a multi-layer CNN encoder parameterized by θ, maps the filtered CIR input to a known 2D position label (x_t, y_t):

$$(x_t, y_t) = \hat{f}_\theta(\tilde{\mathbf{H}}_t^{\text{norm}}). \tag{5.16}$$

Table 7.1 describes the layers of the embedding CNN on AI/ML host of Figure 5.7 with results discussed in Section 7.7.

5.5 Results

This section presents experimental results from the three testbeds demonstrating the effectiveness of our proposed positioning pipeline at the LMF using TDoA and Finger Printing methods. Starting with the GEO-5G testbed at EURECOM, Figure 5.8 shows the benchmarking of our TDoA-based method against the RTK setup in a scenario where a person carries the UE along the depicted trajectory. Our method achieves 2.36m accuracy in 90% of the time in a mobile scenario.

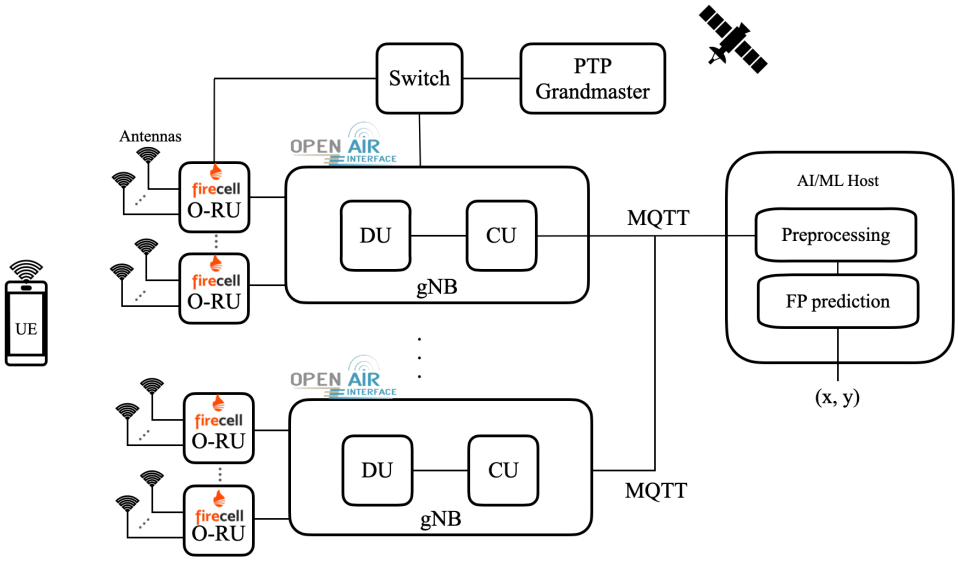

Figure 5.7: System model for AI/ML positioning

The mobile scenario dataset is available online at [1]. Figure 5.9a demonstrates that using per-RU TDoA references improves positioning accuracy under synchronization impairments by mitigating intra-RU timing offset. Figure 5.9b compares antenna placement strategies at EURECOM, showing that 2 RUs with 8 non-collinear antennas yield more diverse TDoA measurements along both x and y-axis and better positioning accuracy than a single RU with 4 collinear antennas.

Figure 5.10a presents results from Mattern Lab where dense multipath was observed. This figure shows that our TDoA filtering significantly reduces outlier measurements and improves overall positioning accuracy. These results support the importance of discarding unreliable TDoAs, especially under dense multipath conditions.

Figure 5.10b shows the performance gain of the proposed Finger Printing method with NLoS masking, tested on a mixed LoS/NLoS dataset collected at Airbus. Compared to conventional Finger Printing, masking NLoS CIRs improves accuracy by reducing noise in the training and inference stages. The figure also demonstrates the resilience of the Finger Printing model when trained with fewer antennas, showing only a moderate drop in performance. This highlights a major advantage of AI/ML-based methods as they are less dependent on antenna count and can generalize better from large, labeled datasets. The summary of all numerical results is presented with Mean Absolute Error (MAE) and 90 percentile in error CDF (CE90) in meters in Table 5.2.

5.6 Conclusions

This chapter presents an experimental evaluation of three OAI 5G positioning testbeds using uplink TDoA and newly integrated OAI functionalities, NRPPa and LMF, across diverse real-world scenarios as well as a public dataset. Our contribution is a complete positioning pipeline at LMF, including ToA and TDoA filtering and a novel PSO-based position estimator that handles timing offsets. In mixed LoS/NLoS conditions, a masked Finger Printing model is trained on CIR data and introduced within a beyond-3GPP, O-RAN-inspired framework. Results show

[1] `https://gitlab.eurecom.fr/ahadi/5g-srs-datasets`

Testbed	Conditions	MAE (m)	CE90 (m)
GEO-5G	4 collinear antennas TDoA	3.12	6.67
	8 non-collinear antennas TDoA	1.20	1.96
	Common reference TDoA	3.12	5.17
	Per RU reference TDoA	1.20	2.02
	Handheld mobile UE TDoA	1.32	2.36
Stellantis	Filtered TDoA	1.22	1.99
	Unfiltered TDoA	4.81	8.74
Airbus	16 antenna TDoA	5.78	8.94
	16 antenna Finger Printing	0.54	0.74
	8 antenna Finger Printing	1.14	2.21
	4 antenna Finger Printing	1.51	4.04

Table 5.2: MAE and CE90 across different testbeds and positioning conditions

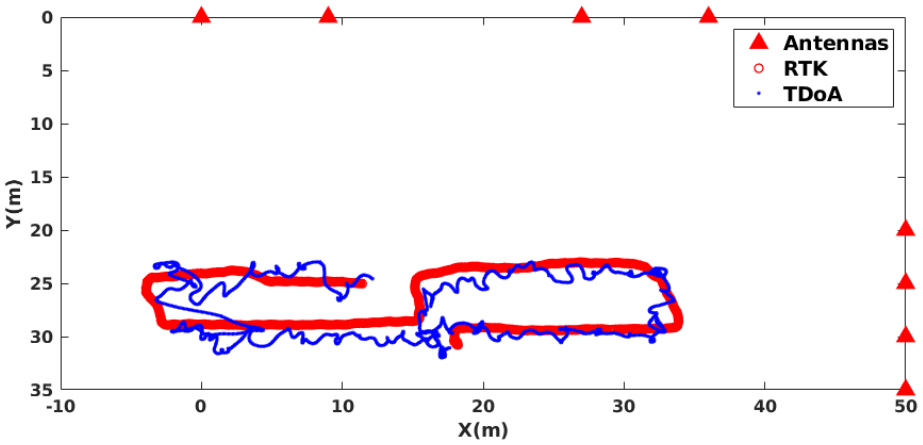

Figure 5.8: Benchmarking TDoA-based handheld mobile UE positioning against RTK at GEO-5G testbed

approximately 2m accuracy in 90% of cases under favorable conditions, while highlighting the need for richer data like CIR in challenging environments. Future work targets integration with RIC and the E2 interface for standard O-RAN deployments.

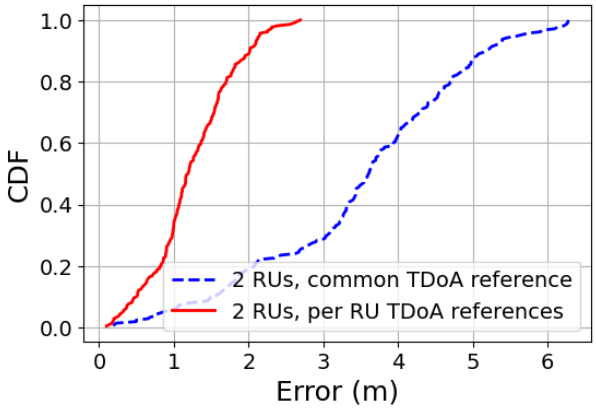

(a) Common vs per-RU TDoA reference

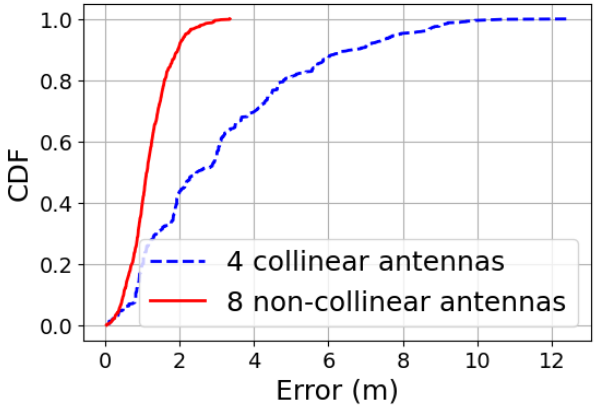

(b) Collinear and non-collinear antennas

Figure 5.9: Positioning performance at the EURECOM testbed

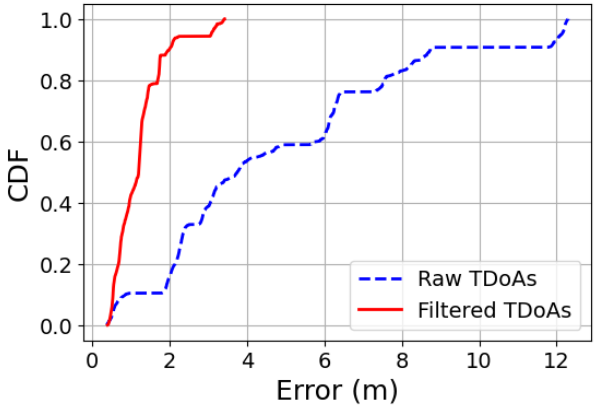

(a) Filtered TDoA positioning

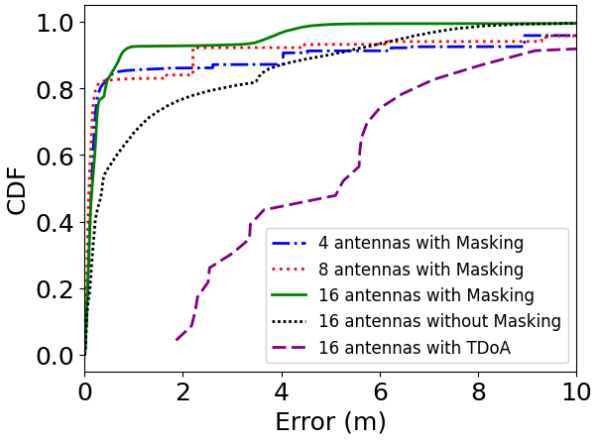

(b) Finger Printing

Figure 5.10: Positioning at (a)Stellantis and (b)Airbus

Chapter 6

Global Scale Self-Supervised Channel Charting with Sensor Fusion

In this chapter, a user localization method is proposed that, unlike conventional 3GPP standard methods, exploits the similarity of high-dimensional CIR data to train a Neural Network that maps each CIR into a 2D position. The dimensionality reduction methods like this are called Channel Charting (CC), which gained a lot of attention in 5G positioning literature in recent years. In this work, we combined CC with sensor fusion to improve its performance in scenarios where only a limited number of antennas (for example, 2 antennas) are available, where conventional methods based on TDoA fail to meet the standard indoor positioning requirements.

6.1 Introduction

Positioning techniques in wireless networks traditionally rely on channel parameter estimation methods like RSSI, ToA, TDoA, and AoA/AoD [23, 28]. These parameters help triangulate or trilaterate a device's position, while CSI offers a more comprehensive approach by considering detailed channel properties and environmental effects on the signal. This method is particularly effective in complex indoor environments where dense multi-path propagation and NLoS conditions are dominant. Direct CSI positioning methods are divided into two categories, supervised and unsupervised [91]. Supervised learning, particularly fingerprinting (FP) methods, relies on a pre-established database of signal characteristics like CSI or Multi Path Components (MPC) as features collected at known UE locations. This database is used to train a model that can later predict the location of a device based on its observed CSI or features, making it highly effective in environments with stable signal patterns. Unsupervised learning, on the other hand, does not require a pre-labeled dataset. Instead, it estimates a mapping directly from the collected data for an objective function. This approach is valuable in dynamic environments where it is impractical to create and maintain an extensive labeled dataset, offering the flexibility to adapt to changes in the environment over time.
Although CSI provides a comprehensive view of wireless signal propagation from the transmitter to the receiver, including the effects of environmental factors (e.g., scattering, fading, and reflection), this detailed information results in high-dimensional data, which makes analyzing positioning systems challenging. CC is an innovative approach in wireless networking, seeks to create a map or chart of the wireless medium using CSI, enabling the precise localization and tracking of devices within complex environments [92]. CC is one of the applications of manifold learning, a non-linear dimensionality reduction technique, that plays a vital role in interpreting CSI data. Manifold learning effectively uncovers the low-dimensional structures

hidden within high-dimensional CSI datasets. This refines signal propagation properties, resulting in more precise perceptions of wireless signal interactions with their surroundings. The primary objective in dimensionality reduction is to map data from a high-dimensional space (D) to a lower-dimensional space (d) (where $d << D$), with two key objectives: i) The mapping should maintain the proximal relationships among data points, and ii) It should effectively generalize to new and unseen data. Non-parametric CC techniques such as Multidimensional Scaling (MDS), Isometric Mapping (ISOMAP), and Principal Component Analysis (PCA) perform well in simplifying high-dimensional data while retaining critical structures [93]. MDS focuses on preserving pairwise distances, ISOMAP extends this by maintaining geodesic distances on a manifold, and PCA captures the maximum variance through orthogonal principal components. However, these methods often fail to accurately predict unseen data as they do not learn a general mapping function from the original high-dimensional space to the reduced space. Instead, they are entirely dependent on the specific dataset they are applied to, and any new data requires recalculating the entire model, making them unsuitable for prediction in dynamic environments. Conversely, parametric approaches like deep learning-based methods are adept at learning a mapping function that can be applied to novel, unseen data. This capacity to extend CC to previously unseen CSI data is a significant advantage over traditional strategies. Despite the recent advancements in self-supervised CC using deep metric learning in [94–106], (Explained in Section 7.2), they still struggle to match the precision achieved by supervised or traditional triangulation methods, even in Line-of-sight (LoS) (Evaluated in section 6.5). Thus, in this chapter, we developed a novel CC algorithm, leveraging a neural network and data fusion to accurately localize the user. Specifically, our contributions are:

- A neural network-based CC function to accurately localize users while preserving global geometry.
- We enhanced localization accuracy using data fusion with depth data only during the training phase.
- Our algorithm is self-supervised, utilizing nearby antenna a.k.a TRP locations, CSI, and depth data during training without requiring labels.
- Our method achieves a sub-meter localization accuracy using two LoS TRPs in 90% of the time, superior to the state-of-the-art and traditional triangulation methods.

6.2 Related work

CC for localization in wireless networks has been used for the first time in [94] from a single base station (BS) with multiple antennas, and in [95, 96] from multiple massive MIMO BSs in space. Since CC relies on dimensionality reduction of the CSI, [97] and [98] used autoencoders to improve this task. A Siamese neural network in [99, 102] is proposed that takes random pairs of CSI to first learn a local channel chart and then transform it to the global form using a subset of labeled data as reference points in a semi-supervised manner. In this method, the Euclidean distances of the CIR measurements are used as a dissimilarity metric. To overcome the limitations of the Siamese loss function with a Euclidean distance metric, a triplet-based loss is used in [100, 101] to learn the similarity between triplets of CSI data based on the distance of other side-informations such as the relative recording timestamps. Authors of [103, 104] combined CC with the classical localization approaches, taking ToA and AoA measurements to improve the global channel chart. Although the CSI measurements can contain rich information, none of these CC studies exploiting only CSI data have surpassed the performance of traditional

triangulation-based methods, even when LoS conditions are present. In [105], velocity estimation and topological map data are used for the global transformation of the CC. However, the global consistency of this algorithm relies on the length of the trajectory taken by the user. Also, the map-matching algorithm in this study works only if a unique match of the channel chart exists in the map. Finally, in [106], by proposing a loss function containing a bilateration loss including multiple BSs with known locations and a triplet loss, a self-supervised CC is made in real-world coordinates. Motivated by this, in this chapter, we leverage sensor fusion and the location of the nearby TRPs in the training phase to enhance localization accuracy.

6.3 System Model

In this chapter, we consider two phases of training and testing. For both phases, we assume an indoor scenario where a mobile user, a.k.a UE, transmits UL-SRS to a base station[1] with M distributed TRPs with fixed and known locations $\mathbf{x}_m \in \mathbb{R}^3, \forall m \in [1, M]$ placed in the environment. The UE follows a trajectory with a duration of N time steps. The UE location at each time step n is assumed unknown and denoted by $\mathbf{u}_t \in \mathbb{R}^3, n \in [1, T]$. The height of the UE is presumed to be fixed during its trajectory. The UE and TRPs are equipped with single antennas operating in Orthogonal Frequency-Division Multiplexing (OFDM) transmission mode with a total of C sub-carriers. The estimated CSI of the link between the m-th TRP and the UE location $\mathbf{u}_t$ (yet assumed unknown) at time step t over all sub-carriers is denoted by $\mathbf{w}_{m,t} \in \mathbb{C}^C$. We obtain the CIR vector $\mathbf{h}_{m,t} \in \mathbb{C}^C$ by applying an inverse discrete Fourier transform on each CSI vector. Consequently, we denote $\mathbf{H}_t \in \mathbb{C}^{M \times C}$ as the CIR matrix which is the concatenation of CIR vectors over all TRPs at time step t. During the training phase, the UE is equipped with a 2D laser scanner to collect depth measurements in addition to CSI, while during the test time, the algorithm only uses the CSI measurements, and no laser scanner is required, hence reducing the sensor requirements and the complexity, as well as saving energy in the testing phase. It is worth mentioning that the algorithm remains self-supervised during both the train and test phases, and the only difference is the type of measurements available at each phase. The depth measurements collected by the laser scanner at time step t during the training phase are denoted by $\boldsymbol{\ell}_t = \{(r_k, \phi_k), \forall k \in [1, K]\} \in \mathbb{R}^{K \times 2}$, where K is the number of points at each scan of the laser scanner, r_k, and ϕ_k are the relative distance and the angle of each scanned point, respectively, in the laser scanner body coordinate frame which we assume to be the same as the UE coordinate frame.

6.3.1 Data Preprocessing and Feature Extraction

To increase the robustness of the algorithm, we preprocess and extract certain features from the measured CIR. Since the majority of the received power is usually concentrated in the first few taps, we only consider the first $\bar{C}$ columns of the CIR matrix. The truncated CIR is denoted by $\hat{\mathbf{H}}_t \in \mathbb{C}^{M \times \bar{C}}$. Therefore, the main input of our algorithm is computed as $\mathbf{H}_t = |\hat{\mathbf{H}}_t| \in \mathbb{R}^{M \times \bar{C}}$, where $|.|$ is the element-wise absolute value operator. We assume that the UE and TRPs are synchronized, akin to [107] using RTT. We then estimate the ToA of the LoS path between UE and TRPs at time step t by detecting the largest peak among the columns of $\mathbf{H}_t$. Equivalently, we can write:

$$\tau_{m,t} \propto \arg \max_{c \in [1, \bar{C}]} y_t^{(m)(c)}, \tag{6.1}$$

[1] Our algorithm can be generalized to multiple BSs without a tight synchronization between them, as well as to multiple UE scenarios.

where $y_t^{(m)(c)}$ is the element of matrix $\mathbf{H}_t$ at row m and column c, and $\tau_{m,t}$ is the measured ToA corresponding to the LoS path (i.e. the largest pick of the CIR vector) between the UE and the m-th TRP at time step t. The ToA of all TRPs and the UE at time step t in a vectorized form is given by $\boldsymbol{\tau}_t = (\tau_{1,t}, \cdots, \tau_{M,t}) \in \mathbb{R}^M$. Furthermore, we exploit the additional measurements provided by a 2D laser scanner, which is available only during the training phase, to estimate the UE displacement between two different time steps. To this end, we employ the well-known Iterative Closest Point (ICP) algorithm for processing the laser scanner data. Due to limited space, we omit the details of the ICP algorithm and we refer to [108] for more information. We denote the estimated UE displacement between time steps t and t' using the ICP algorithm and utilizing laser scanner data by $\hat{T}_{t,t'}$.

6.3.2 Deep Channel Charting

Given the CIR dataset, it is possible to find a mapping function $f_{\boldsymbol{\theta}} : \mathbb{R}^{M \times \bar{C}} \to \mathbb{R}^D$ that transforms the CIR matrix $\mathbf{H}_t$ to a lower dimension $D \leq 3$ as a proxy to the locations, a.k.a pseudo-position, of the user as $\tilde{\mathbf{u}}_t = f_{\boldsymbol{\theta}}(\mathbf{H}_t)$. Deep neural networks have proven to be a good candidate for estimating the mapping function $f_{\boldsymbol{\theta}}$, as $f_{\boldsymbol{\theta}}$ is a complicated and nonlinear function. Various methods have been introduced in the literature to find the mapping function using deep neural networks. These methods range from supervised to unsupervised [94–106]. In this chapter, we build a channel chart algorithm upon the bilateration loss function akin to [106] and by capitalizing on ToA measurements and the location of the TRPs. We extend this method further by incorporating laser scanner data to improve the accuracy of localization. Note that the TRP locations and laser scanner data are only required during the training phase. Moreover, our approach is self-unsupervised and will provide a global-scale representation of the user's location in the global coordinate frame very close to the ground truth, as opposed to the pseudo-position of the user. In the following section, we elaborate on our approach.

6.4 Channel Charting Using Data Fusion

In this section, we seek to learn a channel chart function $f_{\boldsymbol{\theta}}$ given a training dataset $\mathcal{D}_{\text{tr}} = \{\mathbf{H}_t, \boldsymbol{\tau}_t, \mathbf{x}_m, \boldsymbol{\ell}_n; \forall t, m\}$. We assume that the pilot signal sent by the UE is received at all TRPs. As expressed in [106], from the received CSI, when we compare the relative received powers at TRPs for a given UE, the TRPs closer to the UE tend to receive a signal with higher power under LoS conditions. Let's denote the received power at TRP m from the UE at time step n with $\gamma_{m,t} = 20 \log(\|\mathbf{h}_{t,m}\|_F)$, where $\|.\|_F$ is the Frobenius norm. Therefore, we can write:

$$\gamma_{m,t_c} > \gamma_{m,t_f} + \Gamma, \forall t_c, t_f \in [1, T], \tag{6.2}$$

where t_c, t_f are time steps chosen such that the UE location at time step t_c is closer to TRP m than when the UE is at time step t_f. In other words, t_c, t_f should satisfy the following:

$$\|\mathbf{x}_m - \mathbf{u}_{t_c}\| < \|\mathbf{x}_m - \mathbf{u}_{t_f}\|, \tag{6.3}$$

where $\|.\|$ is the Euclidean norm. The constant Γ imposes that the received power differs at least by Γ. From (6.3), we can construct the following bilateration loss function:

$$\mathcal{L}^b_{m,t_c,t_f} = \max(\|\mathbf{x}_m - f_{\boldsymbol{\theta}}(\mathbf{H}_{t_c})\| - \|\mathbf{x}_m - f_{\boldsymbol{\theta}}(\mathbf{H}_{t_f})\| + d, 0), \tag{6.4}$$

where $d > 0$ indicates that the UE at estimated location $f_{\boldsymbol{\theta}}(\mathbf{H}_{t_c})$ is closer to TRP m than the UE estimated location $f_{\boldsymbol{\theta}}(\mathbf{H}_{t_f})$ by at least d meters. Assuming that the TRPs are LoS to the UE at all time steps, finding a $f_{\boldsymbol{\theta}}$ that minimizes (6.4) will ideally satisfy inequality (6.2). However, in a realistic scenario, there is no guarantee that the power-distance relation holds, as also indicated in [106]. Moreover, the loss in (6.4) might be equal to zero for a vast majority of (t_c, t_f) pairs, depending on the value chosen for d, rendering it sample inefficient for learning $f_{\boldsymbol{\theta}}$. To tackle this problem, since we can estimate the ToA at each TRP, we can have an estimate of d per measurement at each time step. Consequently, we can reformulate the loss function in (6.4) as follows

$$\mathcal{L}^b_{m,t_c,t_f} = (\|\mathbf{x}_m - f_{\boldsymbol{\theta}}(\mathbf{H}_{t_c})\| - \|\mathbf{x}_m - f_{\boldsymbol{\theta}}(\mathbf{H}_{t_f})\| + d_{m,t_c,t_f})^2, \tag{6.5}$$

with

$$d_{m,t_c,t_f} = |\tau_{m,t_f} - \tau_{m,t_c}|\, \nu, \tag{6.6}$$

where ν is the speed of light, and $|.|$ represents the absolute value operator. Please note that the loss function in (6.5) is specified for each measurement pair and is not sparse, resulting in a more sample-efficient training process. However, the expression in (6.5) is a differential loss function with respect to the UE location in two time steps can bring ambiguity to the UE location estimate, hence not preserving the global geometry features. To solve this issue, we redefine $\mathcal{L}^b_{m,t_c,t_f}$ by splitting it into two additive parts as follows:

$$\mathcal{L}^b_{m,t_c,t_f} \triangleq \mathcal{L}_{m,t_c} + \mathcal{L}_{m,t_f}, \tag{6.7}$$

where

$$\mathcal{L}_{m,n} = (\|\mathbf{x}_m - f_{\boldsymbol{\theta}}(\mathbf{H}_n)\| - \tau_{m,n}\, \nu)^2. \tag{6.8}$$

Furthermore, we can formulate a separate loss function for the UE locations at time steps t_c, t_f as follows:

$$\mathcal{L}^\ell_{t_c,t_f} = (\|f_{\boldsymbol{\theta}}(\mathbf{H}_{t_c}) - f_{\boldsymbol{\theta}}(\mathbf{H}_{t_f})\| - \|\mathbf{u}_{t_c} - \mathbf{u}_{t_f}\|)^2, \tag{6.9}$$

where the first part of this loss function ($\|f_{\boldsymbol{\theta}}(\mathbf{H}_{t_c}) - f_{\boldsymbol{\theta}}(\mathbf{H}_{t_f})\|$) represents the displacement between two estimated UE locations at time steps t_c, t_f, and the second part ($\|\mathbf{u}_{t_c} - \mathbf{u}_{t_f}\|$) is equivalent to the true UE displacement. Therefore, minimizing (7.14) will result in preserving the relative displacement between the estimated UE locations in two different time steps. However, the second part of this loss function is not available. To tackle this problem, we exploit the measurements obtained from the laser scanner. We reformulate the loss function (7.14) by incorporating the laser scanner data as follows:

$$\mathcal{L}^\ell_{t_c,t_f} = (\|f_{\boldsymbol{\theta}}(\mathbf{H}_{t_c}) - f_{\boldsymbol{\theta}}(\mathbf{H}_{t_f})\| - \hat{T}_{t_c,t_f})^2, \tag{6.10}$$

where $\hat{T}_{t_c,t_f}$ is the estimated UE displacement between two time steps t_c, t_f using laser scanner data and the ICP algorithm [108].

Finally, the total loss function, including the CIR radio measurements and the laser scanner data, is given by:

$$\mathcal{L}_{m,t_c,t_f} = \mathcal{L}^b_{m,t_c,t_f} + \lambda_{t_c,t_f} \mathcal{L}^\ell_{t_c,t_f}, \tag{6.11}$$

where λ_{t_c,t_f} is a coefficient that determines the impact of the loss pertaining to the laser scanner data. It is worth mentioning that the ICP algorithm might fail to estimate the displacement between two time steps if the depth measurements in two corresponding scans are very different. Therefore, to mitigate this error, we choose the value for λ_{t_c,t_f} to be small when t_c and t_f are far in time.

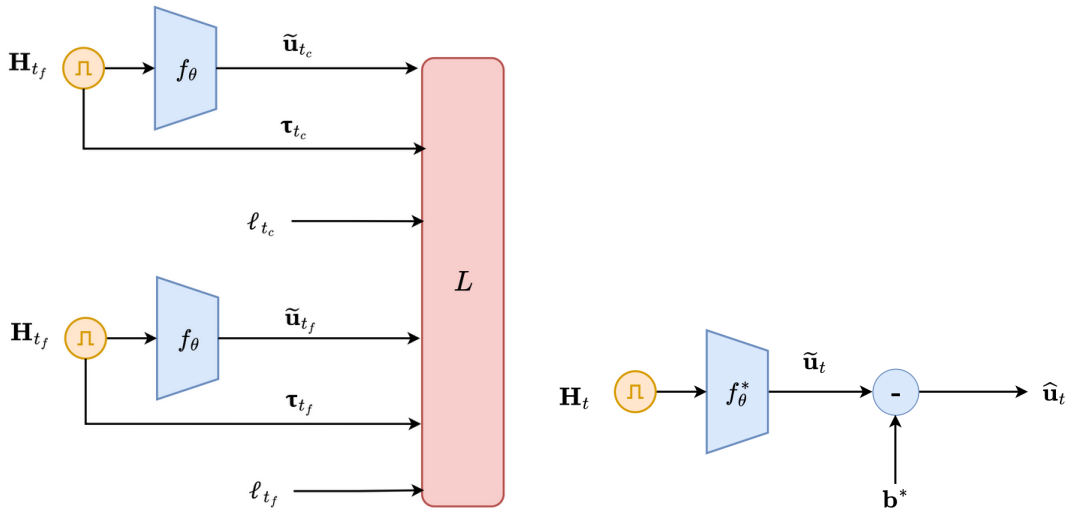

(a) Training phase (b) Test phase

Figure 6.1: Diagram of training and test phases of our algorithm.

Finally, the total loss function for all TRPs and overall time steps is given by:

$$\mathcal{L} = \sum_{\substack{t_f, t_c \in [1,T] \\ t_f \neq t_c}} \sum_{m=1}^{M} \mathcal{L}_{m,t_c,t_f}. \tag{6.12}$$

A neural network can then be trained to obtain a channel chart function $f_{\boldsymbol{\theta}}$ by minimizing $\mathcal{L}$ and using the training dataset $\mathcal{D}_{\text{tr}}$. We denote the trained channel chart neural network model by $f_{\boldsymbol{\theta}^*}$, where θ^* is the optimized parameters of the neural network model after training. Consequently, the trained channel chart function can be used to estimate the UE location in a global scale coordinate frame owing to (6.7). This approach is self-supervised as it does not require labeling during the training or evaluation/test phases.

6.4.1 Offset Estimation

The UE location estimated using the channel chart neural network model ($f_{\boldsymbol{\theta}^*}$) trained in the last section might deviate from the ground truth by an offset. This might happen when a small set of TRPs (fewer than 3 TRPs) is available, which can introduce an ambiguity to the UE location estimate and result in getting stuck in a local minima. To tackle this problem, given a trained channel chart model, we formulate the following optimization problem to calculate the offset in the estimation:

$$\mathbf{b}^* := \arg\min_{\mathbf{b}} \sum_{t=1}^{T} \sum_{m=1}^{M} |\hat{\tau}_{m,t}(\mathbf{b}) - \tau_{m,t}|, \tag{6.13}$$

where $\mathbf{b} \in \mathbb{R}^3$ is a bias vector to be estimated, and $\hat{\tau}_{m,t}(\mathbf{b})$ is the estimated ToA between the m-th TRP and the UE location at time step t and taking into account the bias vector $\mathbf{b}$. Using the trained channel chart model, $\hat{\tau}_{m,t}(\mathbf{b})$ is given by:

$$\hat{\tau}_{m,t}(\mathbf{b}) = \frac{\| \left(f_{\boldsymbol{\theta}^*}(\mathbf{H}_t) - \mathbf{b}\right) - \mathbf{x}_m \|}{\nu}. \tag{6.14}$$

Solving (6.13) will find a bias vector, minimizing the error between the estimated ToA and the measured ToA, thus improving the localization accuracy. We solve (6.13) using the training dataset $\mathcal{D}_{\text{tr}}$ and employing the Particle Swarm Optimization (PSO) technique [109]. We denote the optimized bias vector by $\mathbf{b}^*$.

Finally, the UE location estimate at time step n by taking into account the bias vector is given by

$$\hat{\mathbf{u}}_t = f_{\boldsymbol{\theta}^*}(\mathbf{H}_t) - \mathbf{b}^*. \tag{6.15}$$

Note that ($\mathbf{H}_t$, $\mathbf{b}^*$) are sufficient to estimate the UE location during the test time. A diagram illustrating the overall procedure of our proposed CC algorithm during the training and test phases is shown in Fig. 6.1.

6.5 Evaluations and Results

To evaluate our proposed method against existing state-of-the-art approaches, the following benchmarks were employed:

- **Classical PSO**: We compared the results with an extension of the classical TDoA-based localization algorithm in [89], where the PSO technique [109] is instead used to triangulate and estimate the UE location given the TDoA measurements from the surrounding TRPs.
- **Siamese Neural Network** [102]: Uses pairs of CSI measurements and their corresponding Euclidean distances as a dissimilarity metric, preserved in a 2-D encoded latent space. This technique is semi-supervised since the estimated latent space requires a linear transformation to the global coordinate frame using a subset of CSI data labeled with true UE locations.
- **Triplet-based Neural Network** [100]: It encodes triplets of CSI into a 2-D latent space and, similar to Siamese, is semi-supervised and utilizes some labeled data.
- **Triplets + Bilat.** [106]: Employs a self-supervised approach using known TRPs locations and their received power in a combined triplet and bilateration loss function to train a model in the global scale coordinate frame.

The performance of the CC models is assessed through both quantitative and qualitative methods. Quantitative key metrics include Continuity (CT) (ensuring spatial relationships are preserved in lower-dimensional space), and Trustworthiness (TW) (ensuring charted similarities reflect true proximities) as detailed in [110]. In addition, the CDF of the localization error at the 90th percentile (CE90), indicates localization accuracy and the spread of errors across locations. Qualitatively, evaluating the charted space through visual inspections against expected wireless environment geometries helps verify if the model accurately identifies meaningful patterns and relationships within the data.

In our simulations, we consider an indoor factory scenario where a UE is transmitting UL-SRS signals with 100MHz bandwidth and 122.88 MSamples/sec sampling rate in sub-6 GHz frequency to $M = 2$ LoS TRPs with a fixed height of 8 m. For the sake of comparison, the training and testing trajectories are similar to the datasets from [102] and IPIN competition 2023 Track 7, both recorded in the Fraunhofer IIS L.I.N.K. hall, where the measurements are taken in an approximately $20 \times 15\,\text{m}^2$ area. Nevertheless, we reconstructed the CIR data from the above trajectories in Matlab using a 3D map-based Ray-Tracing toolbox to simulate the laser data in the same environment. In Fig. 6.2a, we depicted the actual trajectory followed during the training phase, and Fig. 6.2b shows the reconstructed training trajectory using only the laser scanner data incrementally and using the ICP algorithm [108]. It's important to note that the

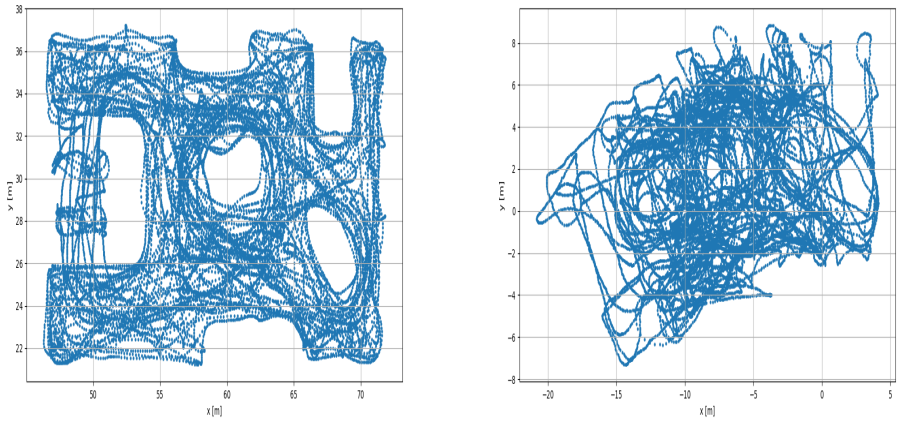

(a) Ground truth (b) Laser scanner

Figure 6.2: True trajectory (a) vs. the estimated trajectory using only the laser scanner data (b), during the training phase.

reconstructed trajectory based on laser scanner data is prone to errors due to measurement drift and coordinate differences as the true user locations are unknown (see Fig. 6.2). Consequently, this trajectory cannot be used directly, making approaches like fingerprinting infeasible. In Fig. 6.3a and 6.3f, we illustrated the true trajectories followed by the mobile UE during the testing phase. We also define the global coordinate frame as the coordinate frame used for recording ground truth trajectories. The test datasets corresponding to the test trajectories shown in Fig. 6.3a and 6.3f are denoted by Dataset 1 and Dataset 2, respectively. We choose the first 49 elements of the CIR matrix, therefore the dimension of the input to our CC network is as $\mathbf{H}_t \in \mathbb{R}^{2\times 49}$. The height of the UE is assumed to be known and equal to 1.5 m and remains constant during both the training and test phases. Therefore, we estimate the UE location in the 2D space. [2] We simulated a 2D laser scanner during the training phase, which provides depth measurements with a resolution of 0.6 degree in the angular domain, and an accuracy of 5 cm for ranging. Both depth and CIR measurements are collected every 20 ms. The architecture of the encoder-based neural network used for the CC function is similar to [102] and summarized in Table 7.1. In addition, We selected $\lambda_{t_c,t_f} = 5$ when $|t_c - t_f| \leq 500$, otherwise $\lambda_{t_c,t_f} = 0$.

In Fig. 6.3b to 6.3e, the results of channel charts for test Dataset 1, and in Fig. 6.3g to 6.3j, the results related to test Dataset 2 for different benchmarks are shown. For better visualization, plots are color-coded in RGB values normalized between $[0, 1.0]$, whereby points with color values closer to 1.0 indicate more accuracy or smaller error in position estimate compared to the ground truth. It is worth mentioning that the location estimate provided by our proposed algorithm is in the global coordinate frame, very close to the ground truth. This is owing to using the ToA measurements along with the TRP locations and the laser scanner data during the training phase.

Furthermore, the value metrics introduced in Sec. 6.5 for the test datasets and different benchmarks are compared in Table 6.2, which clearly shows that our proposed algorithm outperforms the benchmarks. Also, we compared the results with the Classical PSO benchmark, which is a classical TDoA-based localization method as described in Sec. 6.5. It is worth mentioning that, to triangulate the UE using such traditional algorithms, at least 3 TRPs are

[2] Our algorithm can be generalized to 3D UE localization without limit.

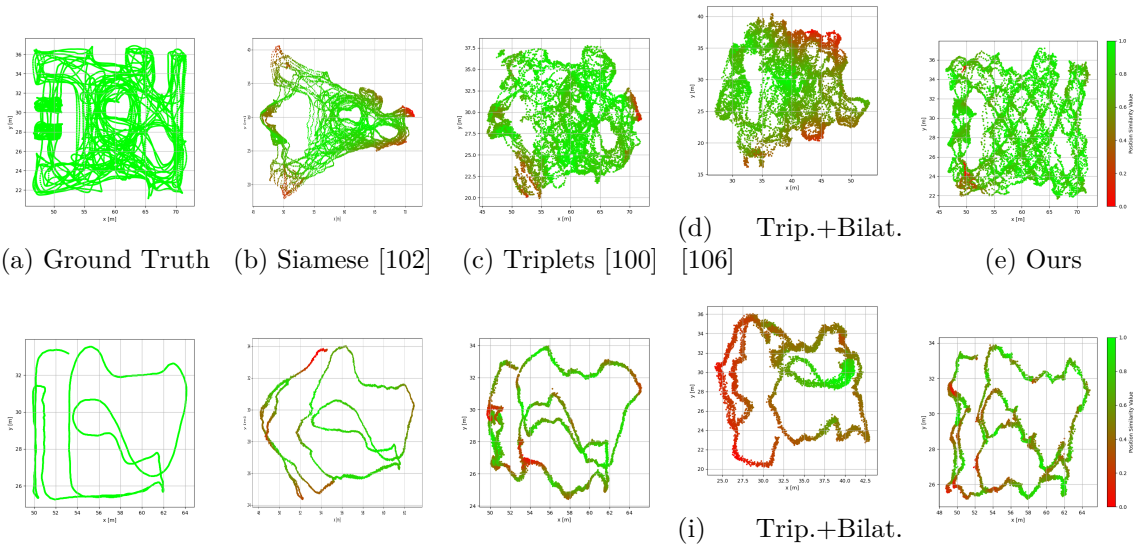

(a) Ground Truth (b) Siamese [102] (c) Triplets [100] (d) Trip.+Bilat. [106] (e) Ours

(f) Ground Truth (g) Siamese [102] (h) Triplets [100] (i) Trip.+Bilat. [106] (j) Ours

Figure 6.3: Figures (a) to (e) are the results for test Dataset 1, and figures (f) to (j) are the results for test Dataset 2.

required, as opposed to 2 TRPs used in our algorithm. Despite using 3 TRPs, the localization accuracy of the classical method is inferior to our algorithm.

In Table 6.2, we also present the results related to an additional experiment that we conducted by running our algorithm without utilizing the laser scanner data, which is equivalent to setting $\lambda_{t_c,t_f} = 0, \forall t_c, t_f$. The results confirm that the incorporation of laser scanner data can significantly improve the accuracy of localization.

Table 6.1: Embedding Model Architecture Summary

Layer	Output Dimension	Kernel Size	Activation
Conv2D	(8, 2, 49)	(3, 3)	ReLU
Conv2D	(8, 2, 49)	(5, 5)	ReLU
Conv2D	(8, 2, 49)	(8, 8)	ReLU
Conv2D	(16, 2, 49)	(10, 10)	ReLU
Flatten	(1, 1568)	-	-
Fully Con.	(1, 200)	-	ReLU
Fully Con.	(1, 100)	-	-
Fully Con.	(1, 2)	-	-

6.6 Conclusions

In this chapter, we presented a novel CC method that uses ToA measurements from nearby TRPs along with their locations. In addition, we leveraged sensor fusion by incorporating laser scanner data during the training phase of the algorithm. Our algorithm is self-supervised during the training and test phases, requiring no geometrical models or user position ground truth. Simulation results demonstrated that our algorithm achieves sub-meter level localization accuracy 90% of the time, surpassing the state-of-the-art CC techniques and the traditional

Table 6.2: 2 TRPs Comparison of Our Model with State-of-the-Art over Datasets 1 and 2

	CT		TW		CE90 [m]	
Model	1	2	1	2	1	2
Classical PSO	0.987	0.978	0.986	0.984	1.59	1.45
Siamese [102]	0.996	0.994	0.994	0.991	3.08	2.24
Triplets [100]	0.993	0.994	0.992	0.994	2.29	1.35
Triplets+Bilat. [106]	0.991	0.980	0.990	0.964	24.14	22.16
Ours (no Laser)	0.995	0.992	0.995	0.991	3.98	3.81
Ours	0.998	0.996	0.997	0.995	0.94	0.97

triangulation-based approaches. CC leveraging data fusion is still in its infancy and requires further investigation. For future research, we will extend this work by exploring NLoS scenarios as well as exploiting additional measurements, such as AoA. Moreover, λ_{t_c,t_f} can be selected more dynamically.

Chapter 7

Uplink TDoA-Based Self-Supervised Channel Charting with NLoS Mitigation

7.1 Introduction

Standard 5G NR methods for positioning a UE in a wireless network rely on estimating channel parameters such as ToA, TDoA, and AoA/AoD [23, 28]. These measurements enable triangulation or trilateration of a device's position, while CSI provides a richer representation by capturing detailed channel properties and environmental influences. CSI is particularly valuable in challenging conditions, such as multi-path propagation and NLoS scenarios common in dense urban or indoor environments.

Direct CSI-based positioning methods are broadly categorized into supervised and unsupervised approaches [91]. Supervised learning, especially fingerprinting, leverages a database of signal features (e.g., CSI or Multi-Path Components, MPC) collected at known locations to train a model that can later predict positions. This works well in environments with relatively stable channel characteristics and if a large dataset with labels is available. In contrast, unsupervised methods bypass labeled datasets by directly inferring position from collected data through loss functions, making them more adaptable to dynamic environments where maintaining large labeled datasets is impractical.

While CSI offers comprehensive insights into wireless propagation, in OFDM systems, it represents high-dimensional data, posing challenges for direct use in positioning tasks. Channel Charting (CC) is a dimensionality reduction method that addresses this by learning a map of the wireless environment from CSI or CIR to an embedding space with a lower dimension, enabling device localization and tracking even in complex propagation scenarios [92]. The CC goal is to transform data from a space of dimension D to a lower dimension $d \ll D$, while preserving the physical relationships of the original space in the embedding space.

Non-parametric CC methods such as Multidimensional Scaling (MDS), Isometric Mapping (ISOMAP), and Principal Component Analysis (PCA) have shown effectiveness in reducing dimensionality while retaining key structural information [93]. However, these methods are unable to generalize a mapping function to handle unseen data without recomputation. This limits their applicability in dynamic scenarios. Parametric approaches, on the other hand, particularly deep learning-based methods, overcome this limitation by learning mappings that generalize to unseen inputs, offering a significant advantage for practical deployment. Recent advances in parametric methods, also called self-supervised CC with deep metric learning [94–106]

(see Section 7.2) have pushed the field forward. Nonetheless, these methods still fall short of the accuracy achieved by supervised fingerprinting or classical triangulation approaches, even under LoS conditions.

In our earlier work [111], we introduced a CC with a sensor fusion algorithm that outperformed the state-of-the-art CC approaches and classical TDoA methods under LoS conditions. While the results were promising, they were obtained in a simulated environment and relied on the assumptions of ToA availability and LoS propagation.

The present work advances this approach by evaluating a new CC method. Specifically, we extend the CC with a sensor fusion framework to incorporate TDoA measurements, which can be obtained through tight synchronization among RAN nodes without requiring precise RAN-UE synchronization. Furthermore, by leveraging the known positions of antennas, a.k.a. TRPs, we achieve global-scale predictions of UE locations within a common local Cartesian coordinate system. To address multipath effects, we exploit the empirical power distributions of CIR datasets to distinguish between LoS and NLoS conditions, and mask NLoS measurements during training and testing. Finally, by integrating synthetic displacement measurements into CC predictions, we enable smooth localization and tracking in mobile scenarios.

The performance of the proposed CC is evaluated first by synthetic data from the Matlab Ray-Tracing environment, and secondly by a real-world positioning setup called "GEO-5G testbed" at EURECOM. For this, we deployed an O-RAN 5G network and tested our new CC model. We will discuss how hardware impairments and practical considerations in our testbed affect the position estimation and how we manage to solve them. Our CC predictions are compared with the Real-Time Kinematic (RTK) positioning, which is an enhanced solution to the Global Positioning System (GPS) [112]. The main contributions of this chapter are;

- A novel CC method that predicts UE's position in mixed LoS/NLoS conditions with 2-4 m accuracy,
- A practical approach by incorporating CIR, TDoA measurements, TRP locations, and displacement measurements to achieve a self-supervised and global-scale position estimation in mobile scenarios,
- Evaluating the performance in both simulation and real 5G O-RAN testbed,
- Publicly providing the 5G CIR dataset of the UE's trajectory as well as ground truth positions. [1]

The remainder of this chapter is organized as follows. Section 7.2 reviews the related work. Section 7.3 introduces the system model. Section 7.4 presents the proposed CC approach based on TDoA knowledge and sensor fusion with NLoS mitigation. Sections 7.5 and 7.6 report the evaluations in simulated and real-world environments, respectively. The results are discussed in Section 7.7, and Section 7.8 concludes the chapter and outlines directions for future work.

7.2 Related works

CC for localization in wireless networks has been used for the first time in [94] from a single base station (BS) with multiple antennas, and in [95, 96] from multiple massive MIMO BSs in space. Since CC relies on dimensionality reduction of the CSI, [97] and [98] used autoencoders to improve this task.

A Siamese neural network is proposed in [99] and [102] that takes random pairs of CSI first to learn a local channel chart and then transform it into the global form using a subset of labeled

[1] `https://gitlab.eurecom.fr/ahadi/5g-srs-datasets`

data as reference points in a semi-supervised manner. In this method, the Euclidean distances of the CIR measurements are used as a dissimilarity metric. To overcome the limitations of the Siamese loss function with a Euclidean distance metric, a triplet-based loss is used in [100, 101] to learn the similarity between triplets of CSI data based on the distance of other side information, such as the relative recording timestamps.

Authors of [103, 104] combined CC with the classical localization approaches, taking ToA and AoA measurements to improve the global channel chart. Although the CSI measurements can contain rich information, none of these CC studies exploiting only CSI data have surpassed the performance of traditional triangulation-based methods, even when LoS conditions are present. In [105], velocity estimation and topological map data are used for the global transformation of the CC. However, the global consistency of this algorithm relies on the length of the trajectory taken by the user. Also, the map-matching algorithm in this study works only if a unique match of the channel chart exists in the map. Finally, in [106], by proposing a loss function containing a bilateration loss including multiple BSs with known locations and a triplet loss, a self-supervised CC is made in real-world coordinates.

Motivated by the literature, in this chapter, we extended our last CC with a sensor fusion algorithm in [111] to a more practical model. In this chapter's algorithm, instead of ToA, we incorporate TDoA measurements as well as the TRP locations to the CC loss function to map CIR data into 2D UE locations. TDoA measurement is easier to obtain as the network only requires synchronization among RAN and not with the UE. Moreover, we show that sensor fusion can enhance the performance of CC in scenarios with limited LoS availability.

7.3 System Model

7.3.1 O-RAN Network Architecture

Figure 7.1 shows a system model for our AI/ML 5G positioning solution where we deploy an O-RAN network architecture with 7.2 functional split [113]. In this framework, the gNB is disaggregated into O-CU, O-DU, and O-RU. For localizing the UE in this framework, we consider two phases of training and testing of AI/ML models over the Non-Real Time RIC and Near-Real Time RIC, respectively. The required measurements for AI/ML models are carried over the E2 interface from O-CU-DU to RIC.

For both phases, we assume a mobile UE that transmits Up Link Sounding Reference Signals (UL-SRS) to all TRPs on RUs $k \in \{1, ..., K\}$ of a gNB (while this could be generalized to multiple gNBs). Let TRPs of the k-th RU have index $m_k \in \{1, ..., M_k\}$. The TRPs are distributed in the environment with fixed and known locations $\mathbf{x}_{m_k} \in \mathbb{R}^3$. We measure the SRS channel at time steps of $t \in \{1, ..., T\}$. To achieve an accurate position estimation based on time measurements, a PTP grandmaster provides a synchronization signal that is distributed to the RAN over a switch. The UE follows a trajectory, and its location at each transmission time is assumed unknown and denoted by $\mathbf{u}_t \in \mathbb{R}^2$, while its height is assumed to be fixed. The UE and RUs are operating in OFDM with a total of N_{fft} sub-carriers. The estimated Channel Frequency Response (CFR) of the link between the m_k-th TRP of k-th RU, and the UE at time step t over all sub-carriers is denoted by $\mathbf{w}_{k,m_k,t} \in \mathbb{C}^{N_{\text{fft}}}$. The RU obtains the CIR $\mathbf{h}_{k,m_k,t} \in \mathbb{C}^{N_{\text{fft}}}$ by applying an Inverse Discrete Fourier Transform (IDFT) to the corresponding CFR. Collecting all M_k TRPs of RU k

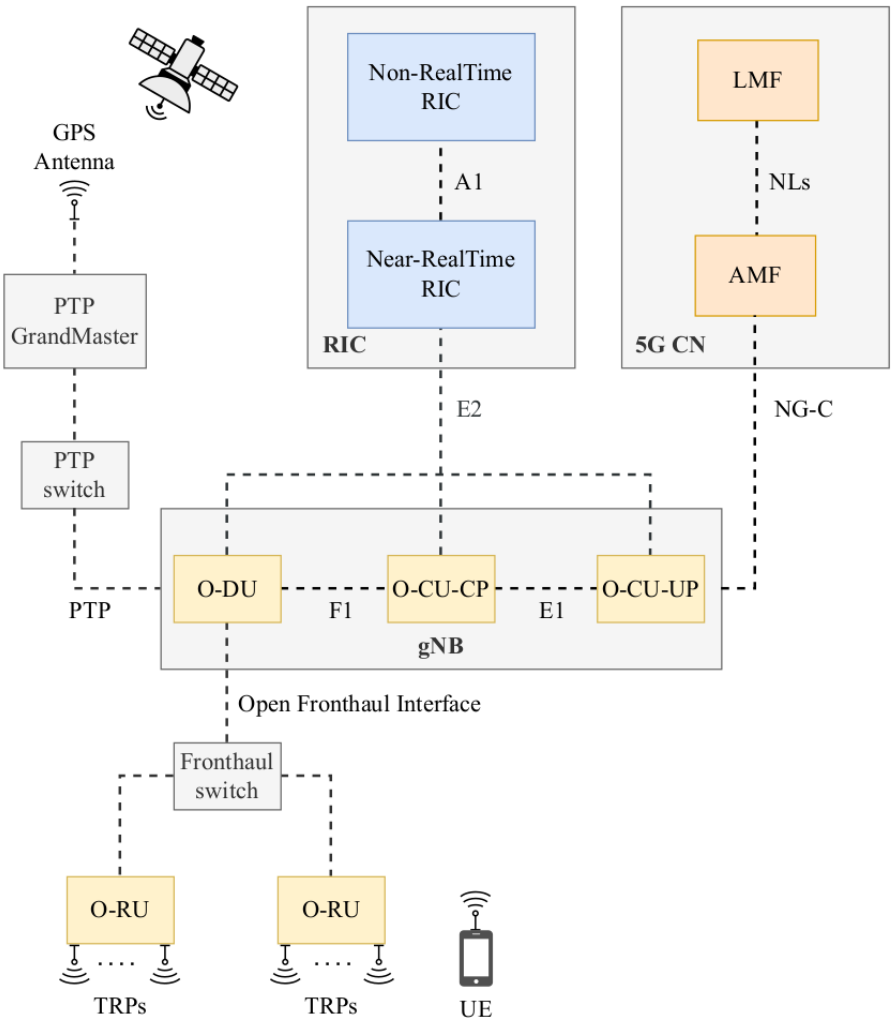

Figure 7.1: 5G AI/ML positioning system model.

yields the RU-level CIR matrix

$$\mathbf{H}_{k,t} = \begin{bmatrix} \mathbf{h}_{k,1,t} \\ \mathbf{h}_{k,2,t} \\ \vdots \\ \mathbf{h}_{k,M_k,t} \end{bmatrix} \in \mathbb{C}^{M_k \times N_{\text{fft}}}, \tag{7.1}$$

Finally, a global CIR matrix of all RUs is defined as

$$\mathbf{H}_t = \begin{bmatrix} \mathbf{H}_{1,t} \\ \vdots \\ \mathbf{H}_{K,t} \end{bmatrix} \in \mathbb{C}^{M \times N_{\text{fft}}}, \tag{7.2}$$

where $M = \sum_{k=1}^{K} M_k$ is the total number of TRPs across all RUs. $\mathbf{H}_t$ is carried to the Near-Real Time RIC for further processing and position estimation.

Moreover, only during the training phase, we assume that the UE's displacement $d_{i,j}$ between times t_i and t_j is available (e.g., measured using an onboard sensor such as an IMU, laser odometry, or LiDAR). We model this displacement as

$$d_{i,j} = (\mathbf{u}_{t_j} - \mathbf{u}_{t_i}) + b_{i,j} + w, \tag{7.3}$$

where w denotes zero-mean Gaussian noise and $b_{i,j}$ represents a slowly varying bias term that accounts for systematic sensor drift. While the variance of w typically grows with the elapsed interval $|t_j - t_i|$, the bias term $b_{i,j}$ also accumulates over time, leading to an increasing deviation between the true and measured displacement. To mitigate this drift, displacement data are considered only within a maximum interval ϵ, such that $|t_j - t_i| \leq \epsilon$.

It is important to note that the algorithm operates in a fully self-supervised manner during both the training and testing phases. Consequently, no ground-truth position label needs to be associated with the CIR measurements for either position estimation or coordinate alignment. The only difference between the two phases is the input data; while displacement information is assumed to be available and leveraged during training, the model is able to generalize and function without displacement data during testing.

7.3.2 Data Pre-Processing and Feature Extraction

To enhance the robustness of the learning model, we apply several pre-processing steps to the measurements before feature extraction. For the first step in the pipeline, it is essential to apply an IFFT shifting as well as the IDFT to the CFR to reposition the zero-frequency component at the center of the time-domain CIR output. Without this step, due to hardware-specific FFT implementations and synchronization signal drift over time, the most significant peak of the CIR may appear wrapped around the beginning or the end of the CIR vector. This leads to inconsistent peak estimation over time and across RUs. Next, on each RU separately, we compensate for the TDoA between TRPs by introducing a peak-based alignment step. Let $\tau^{\text{peak}}_{k,m,t}$ denote the peak index of the CIR vector magnitude on RU k, TRP m_k, at time t:

$$\tau^{\text{peak}}_{k,m_k,t} = \arg \max_{n \in \{1,\ldots,N_{\text{fft}}\}} |\mathbf{h}_{m_k,t}[n]|, \tag{7.4}$$

where $|\cdot|$ denotes the element-wise absolute value operation. In real-world setups with synchronization impairments, an additional pre-processing step is required for outlier peak detection.

This is achieved by applying valid ToA and TDoA bounds derived from the geometry of the testing area, similar to the filters proposed in our earlier work [114]. It is important to note that such synchronization impairments and outliers are not typically present in simulations or in every testbed scenario. An offset index is selected as the earliest peak among TRPs of each RU by.

$$\eta_{k,t}^{\text{offset}} = \min_{m \in \{1,\ldots,M_k\}} \tau_{k,m_k,t}^{\text{peak}}. \tag{7.5}$$

The following operation shifts the vector to the left and fills the tail with zeros:

$$\mathbf{h}_{k,m_k,t}^{\text{shifted}}[j] = \begin{cases} \mathbf{h}_{k,m_k,t}[j + \eta_{k,t}^{\text{offset}}] & \text{if } j + \eta_{k,t}^{\text{offset}} < N_{\text{fft}}, \\ 0 & \text{otherwise}, \end{cases} \tag{7.6}$$

resulting in a TDoA-aligned RU-level CIR matrix $\mathbf{H}_{k,t}^{\text{shifted}}$.

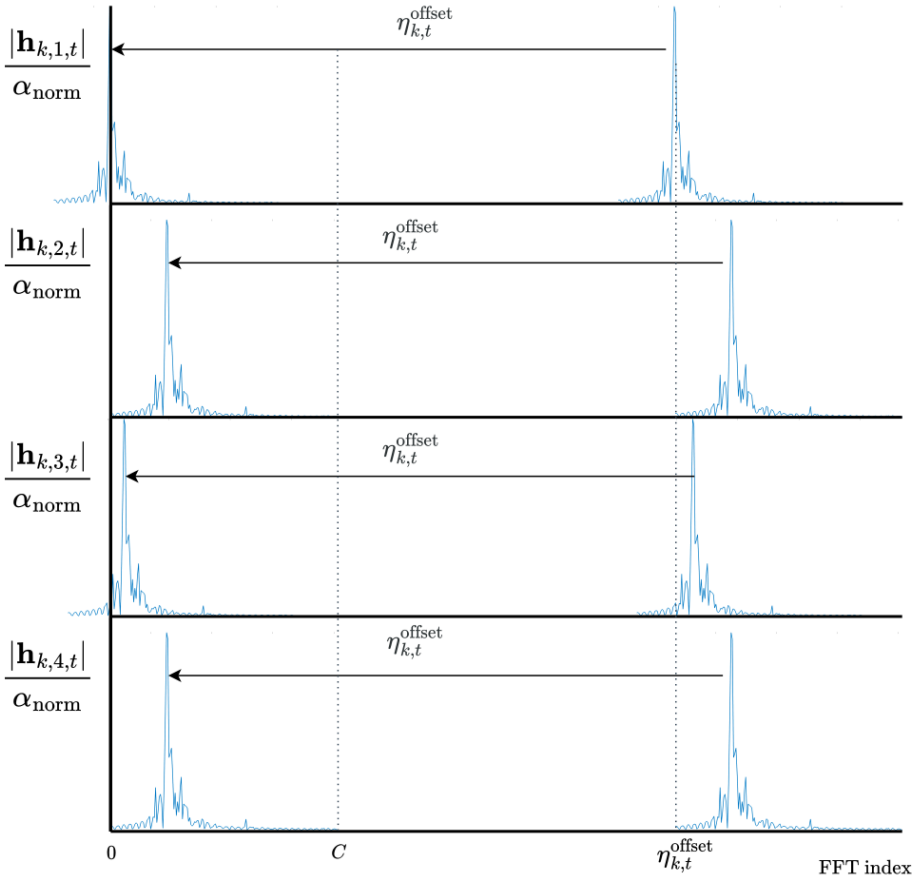

Figure 7.2: CIR shifting, truncation, and normalization in pre-processing while keeping the TDoA integrity

This procedure, during both training and testing phases, ensures that the CIRs are temporally aligned across TRPs of the same RU, thereby respecting the assumption of tight time synchronization among them and the correctness of TDoA.

The TDoA vector is then obtained by subtracting a $\tau_{k,m_{\text{ref},k},t}^{\text{peak}}$ from all M_k TRPs $\tau_{k,m_k,t}^{\text{peak}}$;

$$\boldsymbol{\Delta}\tau_{k,t} = \Big[\, \tau^{\text{peak}}_{k,1,t} - \tau^{\text{peak}}_{k,m_{\text{ref},k},t},\ \ldots,\ \tau^{\text{peak}}_{k,M_k,t} - \tau^{\text{peak}}_{k,m_{\text{ref},k},t} \,\Big], \tag{7.7}$$

where $\tau^{\text{peak}}_{k,m_{\text{ref},k},t}$ denotes the peak index at a predefined reference TRP $m_{\text{ref},k}$ on each RU. Unlike the classical TDoA method, where all TDoAs have the same reference, our approach in selecting a per-RU reference $m_{\text{ref},k}$ is to mitigate hardware synchronization impairments in real-world testing. This is further discussed in Section 7.6. The global CIR shifted matrix $\mathbf{H}^{\text{shifted}}_t$ is further normalized by the maximum peak magnitude observed across the entire training dataset. Also, to form a unified input dimension for model training and testing, CIRs are truncated to only contain the first C fft indices:

$$\mathbf{H}^{\text{norm}}_t = \frac{1}{\alpha_{\text{norm}}} \begin{bmatrix} |\mathbf{h}^{\text{shifted}}_{1,t}| \\ |\mathbf{h}^{\text{shifted}}_{2,t}| \\ \vdots \\ |\mathbf{h}^{\text{shifted}}_{M,t}| \end{bmatrix} \in \mathbb{R}^{M\times C}, \tag{7.8}$$

where the normalization factor $\alpha_{\text{norm}} = \max_{k,m_k,t}(|\mathbf{h}^{\text{shifted}}_{k,m_k,t}|)$ is computed from the training data and reused during testing to ensure consistency. In the following sections, we leverage the training dataset

$$\mathcal{D}_{\text{tr}} = \{(\boldsymbol{H}^{\text{norm}},\, \boldsymbol{\Delta\tau},\, \boldsymbol{X},\, \boldsymbol{D}, \boldsymbol{T})\},$$

where $\boldsymbol{H}^{\text{norm}}$ denotes the normalized CIR matrix at time t, $\boldsymbol{\Delta\tau} \in \mathbb{R}^{M-K}$ is the vector of observed TDoA measurements across all TRPs, $\boldsymbol{X} \in \mathbb{R}^{M\times 3}$ contains the all TRP positions, $\boldsymbol{D}$ is the set of displacement measurements derived from UE's sensors during training, and $\boldsymbol{T}$ timestamps of the measurements. This dataset is used to learn a spatial mapping function that captures the geometric features of the environment. A summary of the pre-processing is depicted in Figure 7.3.

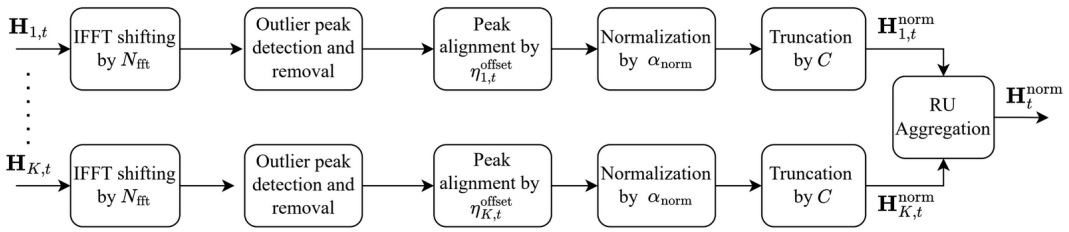

Figure 7.3: CIR pre-processing diagram

7.4 AI/ML Position Estimation

7.4.1 TDoA Channel Charting with Sensor Fusion and NLoS Mitigation

In this section, we seek to learn a self-supervised (no labeled data used) CC function $f_{\boldsymbol{\theta}}(.)$ that transforms each CIR matrix into a 2-dimensional embedding;

$$f_{\boldsymbol{\theta}} : \mathbb{R}^{M\times C} \to \mathbb{R}^2.$$

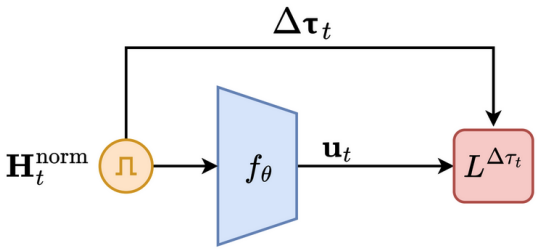

Figure 7.4: CC training with CIR and TDoA

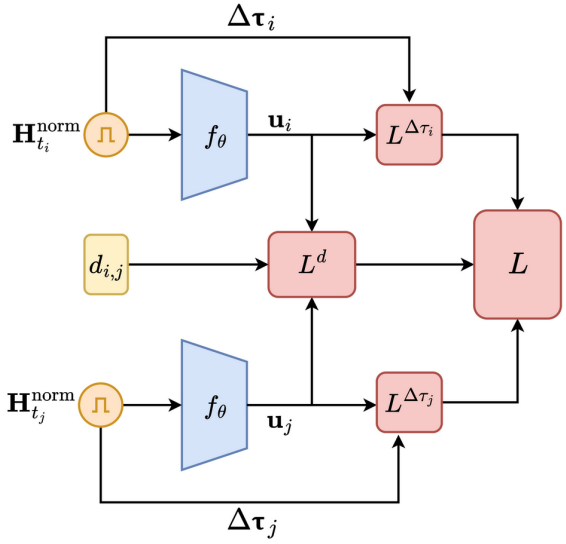

Figure 7.5: CC training with CIR and TDoA+displacement

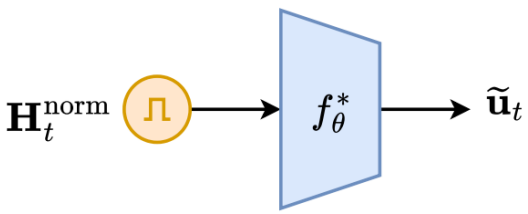

Figure 7.6: CC testing

The mapping is learned such that similarities in the radio channel domain (i.e., channel similarity induced by spatial proximity in the physical environment) are preserved in the embedded space, given our training dataset $\mathcal{D}_{\text{tr}}$. Deep Neural Networks (DNNs) have proven to be powerful nonlinear function approximation and effective tools for dimensionality reduction, making them particularly well suited for learning $f_{\boldsymbol{\theta}}$ mapping [94–106]. Therefore, we employ an embedding DNN model with the architecture described in Table 7.1. The embedding model consists of two convolutional layers for feature extraction, followed by a flattening stage and three fully connected layers. The network gradually reduces the feature dimensionality and projects the CIR input into a compact two-dimensional embedding space suitable for CC.

We assume that the pilot signal sent by the UE is received at all TRPs and the pre-processing step is completed. We begin by randomly selecting pairs of sub-samples from the dataset. A pair with timestamps t_i and t_j is retained if the temporal interval satisfies $|t_j - t_i| \leq \epsilon$; otherwise, it is discarded, and a new pair is drawn. This procedure is repeated P times, yielding a collection of P CIR matrix pairs $\{(\mathbf{H}_{t_i}^{\text{norm}}, \mathbf{H}_{t_j}^{\text{norm}})\}_{p=1}^{P}$, $(P \times (M-2))$ TDoA measurement pairs $\{(\Delta\hat{\boldsymbol{\tau}}_{t_i}, \Delta\hat{\boldsymbol{\tau}}_{t_j})\}_{p=1}^{P}$, and P displacement measurements $\{\hat{d}_{i,j}\}_{p=1}^{P}$. Choosing ϵ on the order of a few seconds provides a reasonable trade-off between displacement estimation accuracy and the level of additive noise. For each $\Delta\hat{\boldsymbol{\tau}}_t$ in a pair, we write a TDoA loss function

$$\mathcal{L}^{\Delta\tau} = \frac{c}{KM_k} \sum_{k=1}^{K} \sum_{m_k=1}^{M_k} |\Delta\tau_{m_k,t} - \Delta\hat{\tau}_{m_k,t}| \tag{7.9}$$

Where c is the constant speed of light. By incorporating UE and TRP locations $\mathbf{u}_n$ and $\mathbf{x}_{m_k}$ we get

$$\begin{aligned}\mathcal{L}^{\Delta\tau} = \frac{1}{KM_k} \sum_{k=1}^{K} \sum_{m_k=1}^{M_k} \Big| &(\mathbf{x}_{m_k} - \mathbf{u}_t - (\mathbf{x}_{\text{ref}_k} - \mathbf{u}_t)) \\ &- c\,\Delta\hat{\tau}_{k,m_k,t} \Big|\end{aligned} \tag{7.10}$$

As $\mathbf{u}_t$ is unknown, we equivalently replace it by CC function $f_{\boldsymbol{\theta}}(\mathbf{H}_t^{\text{norm}})$ in (7.10) to have

$$\begin{aligned}\mathcal{L}^{\Delta\tau} = \frac{1}{KM_k} \sum_{k=1}^{K} \sum_{m_k=1}^{M_k} \Big| &(\mathbf{x}_{m_k} - f_\theta(\mathbf{H}_t^{\text{norm}})) \\ &- (\mathbf{x}_{\text{ref}_k} - f_\theta(\mathbf{H}_t^{\text{norm}})) - c\,\Delta\hat{\tau}_{k,m_k,t} \Big|\end{aligned} \tag{7.11}$$

In practical scenarios, LoS paths may be obstructed by obstacles or diffraction, leading to noisy TDoA estimates. This noise degrades the performance of the CC function. Therefore, we introduce an additional coefficient to $\mathcal{L}^{\Delta\tau}$ to mitigate the impact of NLoS. By applying a NLoS TDoA binary mask on both $\mathcal{L}^{\Delta\tau_i}$ and $\mathcal{L}^{\Delta\tau_j}$, ultimately we have;

$$\mathcal{L}^{\Delta\tau_{i,j}} = \sum_{t=1}^{T} \nu_{t_i}.\mathcal{L}^{\Delta\tau_i} + \nu_{t_j}.\mathcal{L}^{\Delta\tau_j}. \tag{7.12}$$

Considering that two LoS TRPs, $\mathbf{x}_{m_k}$ and $\mathbf{x}_{\text{ref}_k}$, must be involved in a valid LoS TDoA

measurement, the coefficient ν_m is defined as

$$\nu_m = \mu_{m_k,t}.\mu_{ref_k,t} = \begin{cases} 1 & \mu_{m_k,t} = \mu_{ref_k,t}, \\ 0 & \mu_{m_k,t} \neq \mu_{ref_k,t}. \end{cases} \tag{7.13}$$

This requires learning a function $g_{\boldsymbol{\phi}}(\mathbf{H}_t^{\text{norm}}) = \mu_{m_k,t}$ that maps CIR measurements from each TRP to a binary LoS/NLoS state. In the next section, we describe a method for distinguishing between LoS and NLoS propagation conditions.

To further stabilize the CC predictions where only a limited LoS TDoA measurements are left unmasked, we integrate a new loss function $\mathcal{L}^d_{t_i,t_j}$ based on the displacement of the UE during certain intervals of ϵ.

$$\mathcal{L}^d_{t_i,t_j} = (\|f_{\boldsymbol{\theta}}(\mathbf{H}^{\text{norm}}_{t_i}) - f_{\boldsymbol{\theta}}(\mathbf{H}^{\text{norm}}_{t_j})\| - d_{i,j})^2. \tag{7.14}$$

Adding a displacement term to (7.12) helps stabilize CC predictions against fluctuations along a trajectory:

$$\mathcal{L} = \sum_{t=1}^{T} \mathcal{L}^{\Delta\tau_{i,j}} + \beta \mathcal{L}^d_{t_i,t_j}, \tag{7.15}$$

where β is a weighting factor that controls the relative importance of the displacement term. Figures 7.4 and 7.5 illustrate the CC training process using TDoA alone by (7.12) and TDoA combined with displacement by (7.15), respectively, together with the corresponding processed CIR inputs. In contrast, Figure 7.6 depicts the testing phase, where only the processed CIR data are used as inputs.

7.4.2 NLoS Mitigation by Masking

By leveraging the empirical distribution of peak power values in a dataset of CIRs, we adopt a simple yet effective thresholding approach to distinguish between LoS and NLoS conditions and mask out the NLoS measurements. This method is motivated by the masking method introduced in [115] and the observation that LoS components typically exhibit significantly higher peak magnitudes than their NLoS counterparts. The contrast in their power distributions thus serves as a reliable discriminative feature, as illustrated in Figure 7.7.

Each single CIR $\mathbf{h}_{k,m_k,t}$ from dataset $\mathcal{D}_{\text{tr}}$ is normalized by the common factor α_{norm} as described in (7.8) of Section 7.3. This normalization effectively scales down the NLoS CIR power, bringing it close to zero. The CIR state is then classified according to a fixed threshold $\lambda \in (0, 1)$:

$$\mu_{m_k,t} = \begin{cases} 1, & max(\mathbf{h}^{\text{norm}}_{k,m_k,t}) > \lambda \quad \text{(LoS)} \\ 0, & max(\mathbf{h}^{\text{norm}}_{k,m_k,t}) \leq \lambda \quad \text{(NLoS)}. \end{cases} \tag{7.16}$$

Here, $max(\mathbf{h}^{\text{norm}}_{k,m_k,t})$ denotes the maximum peak power of a normalized CIR, and the threshold λ is selected based on the empirical distribution of this variable. This yields a lightweight and interpretable criterion for LoS/NLoS classification that can be tuned based on each environment. The effect of fine-tuning the λ on the CC prediction accuracy is further discussed in Section 7.5.

7.5 Matlab Simulations

To evaluate the performance of our proposed CC method, we first develop a Matlab-based simulation environment that models the 5G positioning scenario under controlled conditions. This allows us to generate synthetic CIRs, introduce noise and multipath effects, and systematically

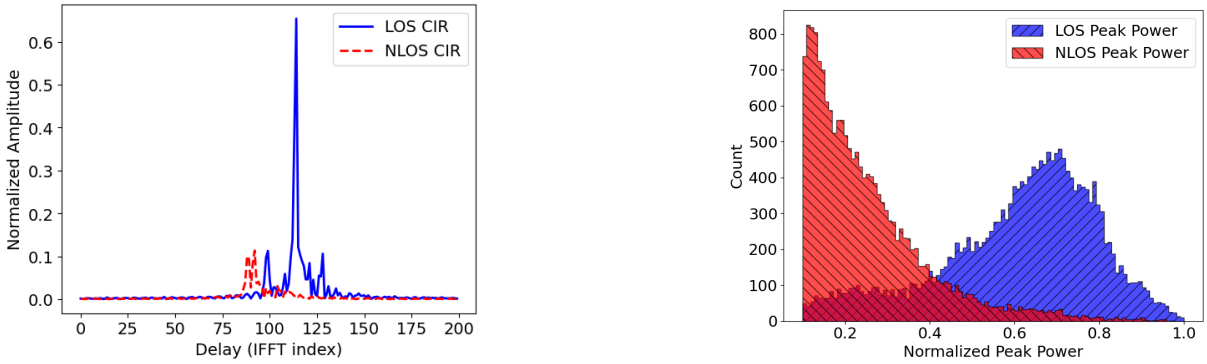

(a) (b)

Figure 7.7: Sample LoS/NLoS data (a) normalized CIR traces, and (b) normalized peak power histograms

Layer	Output Dimension	Kernel Size	Activation
Conv2D	(32, 16, 100)	(3, 3)	ReLU
Conv2D	(64, 16, 100)	(3, 3)	ReLU
Flatten	(1, 102400)	-	-
Fully Con.	(1, 512)	-	ReLU
Fully Con.	(1, 128)	-	ReLU
Fully Con.	(1, 2)	-	-

Table 7.1: DNN embedding model architecture Summary

vary parameters such as the number of antennas, bandwidth, and signal-to-noise ratio. Using this setup, we assess the accuracy, robustness, and convergence behavior of the proposed method before validating it on the real testbed.

In this simulation, a 3D-map of an Indoor Factory Hall (InFH) environment as depicted in Figure 7.8 is created, where a UE transmits UL-SRS signals with a bandwidth of 100 MHz and a sampling rate of 122.88×10^6 Samples/s in the sub-6 GHz band. The signals are received by $M = 4$ TRPs positioned at a fixed height of 8 m that often become NLoS to the UE because of the present clutter in between. The LoS/NLoS state from each TRP's point of view during the training trajectory is illustrated in Figure 7.9. Based on this trajectory, the CIR data as well as the displacement data are reconstructed in Matlab using a 3D map-based Ray-Tracing toolbox.

7.6 GEO-5G Testbed at EURECOM

The GEO-5G localization testbed is part of EURECOM's Open5G testbed, featuring high-speed fiber-connected computing and switching infrastructure. It supports virtualized 5G deployment with USRP and O-RAN radios, integrating OpenAirInterface for virtualized network functions. Thanks to our latest contributions on OAI RAN in [116], we can choose between a single-gNB with multi-RUs or a multi-gNB with multi-RUs architecture. To evaluate OAI's new localization features, we deployed two VVDN O-RAN RUs [84], provided by Firecell [22] with a single gNB (CU-DU) and integrated them into the EURECOM 5G testbed. Furthermore, we have four distributed Panorama directional antennas [117] as TRPs on each RU, which are mounted on the roof railings with low-loss cables, giving us a total of eight TRPs to cover a testing area of

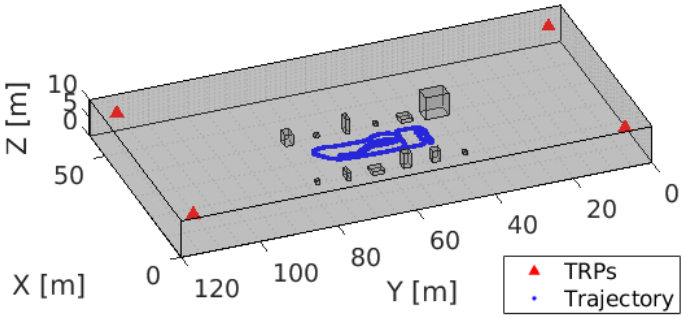

Figure 7.8: Simulated 3D-map InFH in Matlab environment

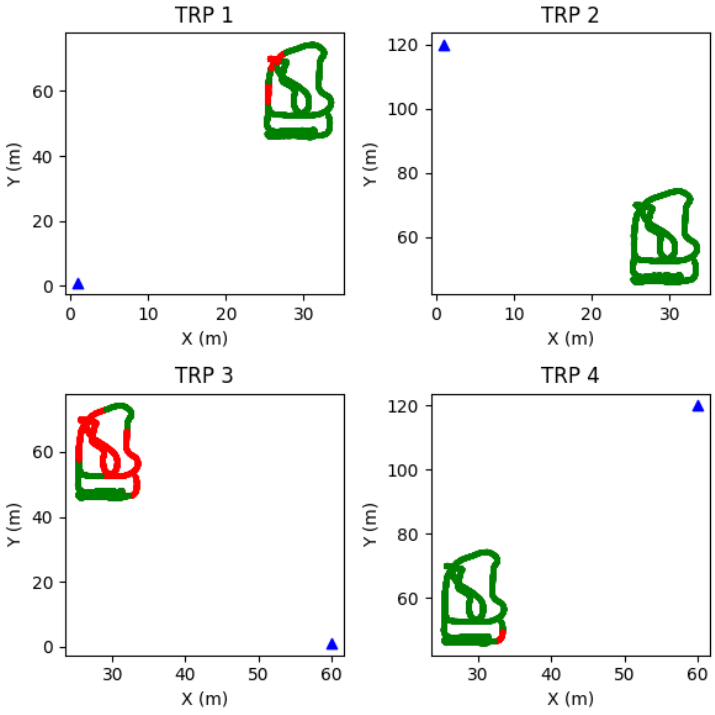

Figure 7.9: Simulated LoS/NLoS state from each TRP's point of view

Figure 7.10: GEO-5G testbed: Deployment of 2 O-RUs each with 4 distributed TRPs on the south terrace and the north rooftop of EURECOM, with a testing area of size 50x10 on the north terrace

50m×10m on the north terrace of EURECOM building, see Figure 7.10. While the integration of the E2 interface and RIC was still in progress during the preparation of this chapter, the performance evaluation was conducted using the MQTT protocol instead of E2. CIR data were transferred from the CU-DU to an AI/ML host machine via MQTT to enable real-time prediction of UE positions. At the same time, the host machine collects RTK position measurements and their corresponding timestamps from the RTK rover over Wi-Fi. These measurements are then used to assess the real-time error of the model's predictions against the RTK ground truth.

In the remainder of this section, we discuss the key practical considerations involved in the implementation and operation of our 5G positioning testbed.

7.6.1 Synchronization

To achieve precise synchronization among distributed RUs and DU, we employ the IEEE 1588-based PTP over the Fronthaul Synchronization Plane (S-Plane) via Ethernet between the DU and RU [118]. A Qulsar Qg2 Grandmaster Clock serves as the central timing source, which locks its timebase to GNSS (Global Navigation Satellite System) signals, ensuring nanosecond-level absolute time accuracy. The Grandmaster then distributes this timing information over fiber to all RUs via a PTP-compatible switch. Each RU operates as a PTP worker, adjusting its local oscillator to align with the Grandmaster's reference clock. This synchronization is critical for coherent UL-TDoA measurements.

However, due to PTP switch impairments and RU long distances at this testbed, errors up to 40 ns are observed. To mitigate the propagation of clock drift from one RU to the other, we adopted a per-RU reference TRP strategy in calculating TDoAs instead of a common reference across all RUs, ensuring internal consistency and reducing cross-RU time drift. A tailored pre-processing pipeline is proposed in our earlier work on GEO-5G testbed experimentation in [114] to discard outlier measurements based on their ToA and TDoAs. These modifications alter the classical TDoA-based positioning. Therefore, a conventional TDoA-based positioning algorithm suffers from these impairments.

7.6.2 Error Measurement

RTK enhances conventional GPS measurements by resolving the carrier-phase ambiguities between a fixed *Base* module and a mobile *Rover* module, enabling a promising centimeter-level accuracy in localization. Therefore, we employed RTK to benchmark our positioning system and use its data to calculate the error of our CC predictions. Although RTK provides accurate absolute positions in geographic coordinates (latitude, longitude, altitude), our system operates in a relative Cartesian reference frame. To bridge this, we transformed the geographic coordinates into local $[u_x, u_y, u_z]$ Cartesian coordinates by applying appropriate projection and translation techniques. Open-source geospatial libraries such as *pymap3d* in Python facilitate the conversion of geographic coordinates into raw Cartesian coordinates x-East, y-North, z-Up (ENU) through standard projection methods.

Furthermore, to align these raw Cartesian coordinates with our system's local reference frame, we perform an additional linear transformation. Specifically, we compute an affine transformation matrix based on a set of predefined anchor points with known correspondences in both geographic and local coordinate systems. This matrix is then used to map all future positions consistently into the local reference frame, ensuring spatial alignment with the experimental environment. We align the raw Cartesian coordinates $\mathbf{u}_{\text{raw}} \in \mathbb{R}^3$, converted from geographic coordinates, with our local coordinate system $\mathbf{u}_{\text{local}} \in \mathbb{R}^3$ using an affine transformation of the form:

$$\mathbf{u}_{\text{local}} = \mathbf{A} \cdot \mathbf{u}_{\text{raw}} + \mathbf{b} \tag{7.17}$$

where $\mathbf{A} \in \mathbb{R}^{3\times3}$ is a linear transformation matrix, and $\mathbf{b} \in \mathbb{R}^3$ is a translation vector. $\mathbf{A}$ and $\mathbf{b}$ are estimated simply by a few known local and raw points using the Linear Least Squares estimator and recorded to be used in real-time testing.

7.6.3 Spatial Power Profile

There are three main sources of power decay in the SRS received signal and consequently channel gain. Distance, multipath and TRP's beam pattern. While in theory we expect the received power to be attenuated with the larger distances of UE, the UL power control in realistic 5G systems plays an essential role in providing a steady channel gain between transmitter and receiver. Specifically, OAI software makes this power control on port 1 of the RUs, which is equivalent to TRPs 1 and 5 in our setup. Figure 7.11 validates this on TRPs 1 and 5, who experience steady normalized peak power as the UE is placed at various distances to them.

However, a NLoS path can show a significantly lower received power than we expect. This is observed on points A and P that are under the building and NLoS to TRP 5 and 6, where the normalized mean peak power is significantly lower.

Moreover, each TRP has a certain angle coverage in azimuth and elevation. The 3dB beamwidth or Half Power Beam Width (HPBW) is the angular width of the main lobe between the two directions where the gain falls by 3 dB, or equivalently, where the power is half of the maximum value. In this testbed, we deployed TRPs with 50° beamwidth in (Azimuth, Elevation). This effect can be observed when the UE is located near the center of the testing area, around points BCDEF and KLMNO, where the TRPs receive a steady and higher normalized peak power. In contrast, TRPs 2, 5, and 6 experience reduced power when the UE is positioned at points ABPO, and a similar reduction is seen for TRPs 3 and 4 when the UE is at points GHIJ, which lie outside of their beam coverage.

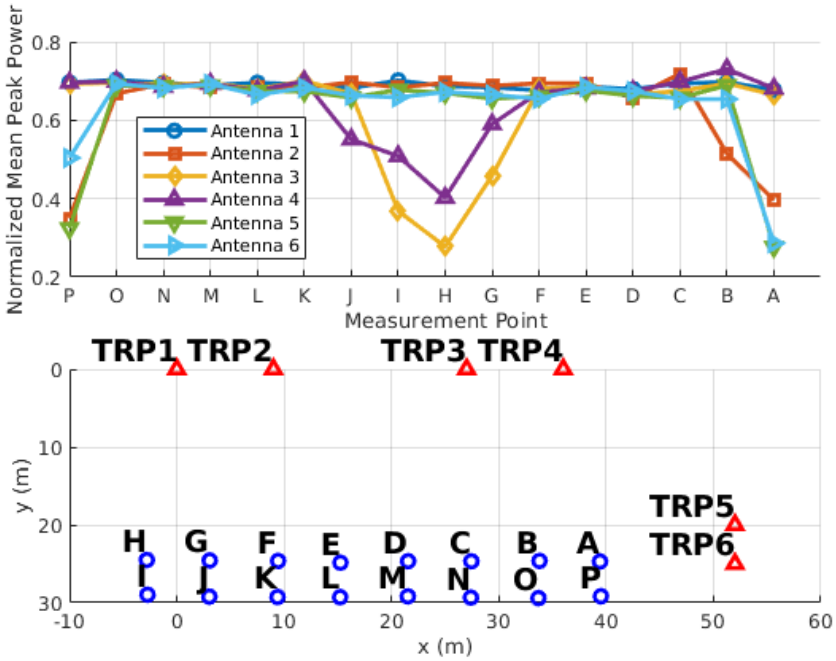

Figure 7.11: GEO-5G tesbed: TRPs spatial power profile

7.6.4 Synthetic NLoS Measurements

The dataset employed in this work was collected using a handheld mobile phone, which was subject to undesired self-shadowing effects caused by the person carrying it. Since no additional clutter existed between the user and the TRPs in the measurement environment, we refer to it as a LoS dataset for generality. To assess the algorithm under controlled NLoS conditions and to regulate the proportion of LoS/NLoS occurrences, we synthetically modify portions of the LoS CIR dataset to emulate NLoS behavior. Specifically, this is achieved by randomly attenuating the signal power and shifting the indices of the dominant peaks within the LoS CIRs. This way, we evaluate the performance of the CC TDoA and TDoA+Displacement losses in different LoS ratios denoted with $r_{\text{LoS}=\{25\%,50\%,75\%,100\%\}}$. For instance, $r_{\text{LoS}} = 50\%$ means 50% of the measurements during the whole trajectory on all TRPs are LoS, and the rest of the trajectory are synthetically behaved as NLoS by random attenuations and random peak shiftings. See Figure 7.12.

7.6.5 Displacement Measurements

Due to the absence of sensors to provide displacement measurements in our testbed, we generated RTK-assisted synthetic displacement data. To avoid the influence of RTK accuracy on the synthetic displacement measurements, additive noise and growing bias were applied to the displacements over longer intervals as detailed in (7.3) of Section 7.3. Therefore, the displacement measurements were estimated in maximum intervals of $\epsilon = 4$ seconds, without explicitly incorporating the RTK positions into the loss function.

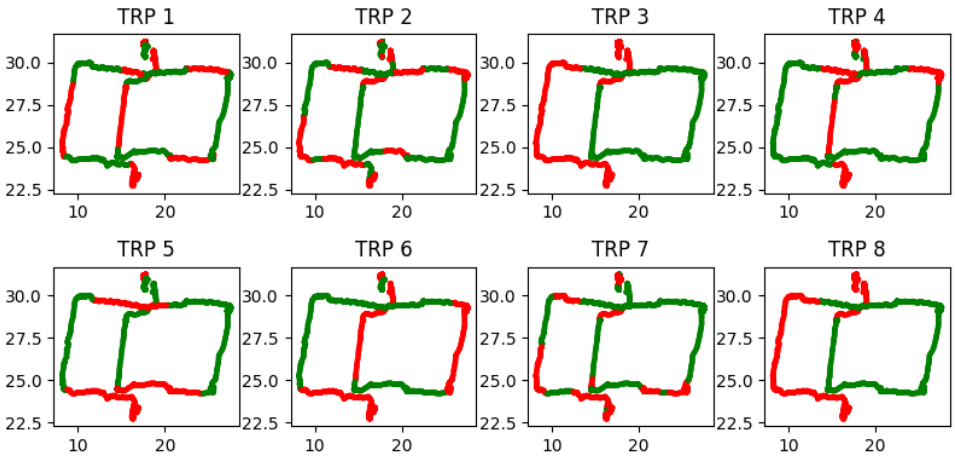

Figure 7.12: GEO-5G testbed: LoS (green) and NLoS (red) state of TRPs at GEO-5G testbed with $r_{\text{LoS}} = 50\%$

7.7 Results

7.7.1 Matlab Simulations

In this subsection, we evaluate the performance of the proposed CC method using TDoA and displacement models in the simulation environment, along with a masking technique designed to mitigate NLoS errors. We first examine the effectiveness of masking in a mixed LoS/NLoS scenario by applying different threshold values and comparing them to the case without masking.

Figure 7.13 shows the heatmap of NLoS masking for several threshold values of λ. The results indicate that $\lambda = 0.2$ provides the closest match to the perfect NLoS identification. Higher thresholds, such as $\lambda = 0.4$ or $\lambda = 0.5$, tend to overestimate the NLoS regions.

The positioning performance of the CC method with TDoA under different masking thresholds is presented in Figure 7.14. For comparison, the results of a conventional TDoA approach using Particle Swarm Optimization (PSO) are also included. The proposed TDoA-based CC method with NLoS masking at $\lambda = 0.2$ achieves an accuracy of approximately 2.5 m at the 90% point of the CDF. In contrast, when $\lambda = 0.5$ leads to overestimation of NLoS measurements, the CC performance degrades noticeably.

Moreover, the conventional TDoA method using PSO without masking suffers from the largest errors, as it lacks robustness against NLoS conditions. By fixing $\lambda = 0.2$ and adding the displacement loss with $\beta = 2$ to the TDoA CC loss function in (7.15), we get a smoother tracking with less fluctuations over the trajectory where only limited LoS TDoAs are available. This is shown in Figure 7.15 and Figure 7.16 with estimated trajectories and error CDF of only TDoA CC and combined TDoA+Displacement CC training.

7.7.2 GEO-5G Testbed

For the experimental evaluation of our proposed models in a real-world channel, we train and test the CC models using data collected from the GEO-5G testbed. As in the simulation study, we analyze the contributions of TDoA and displacement measurements both separately and jointly. This comparison ensures that the main performance gains of the final model originate from CIR and TDoA, rather than from RTK-assisted displacement data.

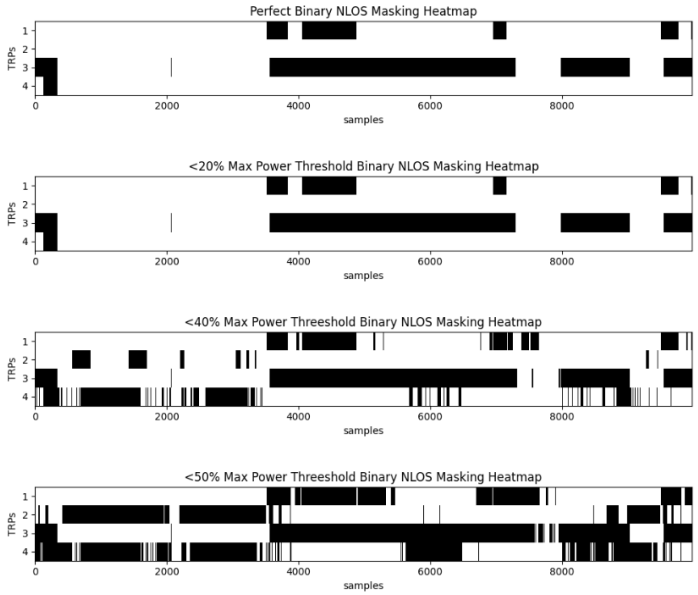

Figure 7.13: Simulated NLoS masking heatmap

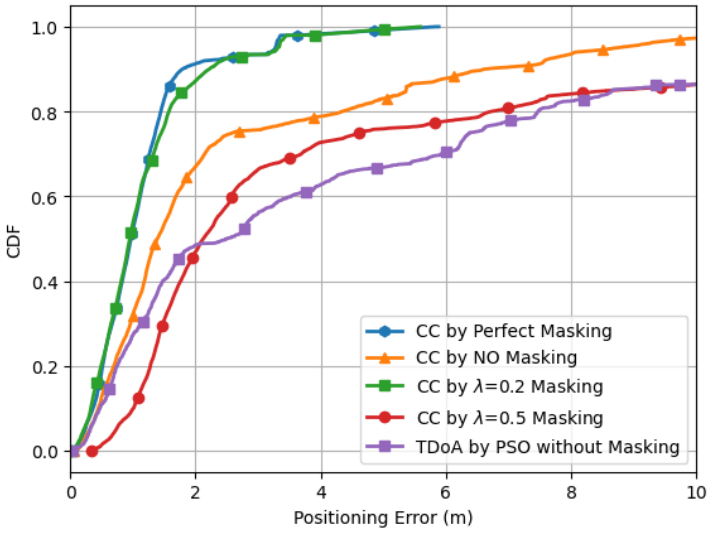

Figure 7.14: Simulated positioning error CDF of TDoA CC with NLoS masking

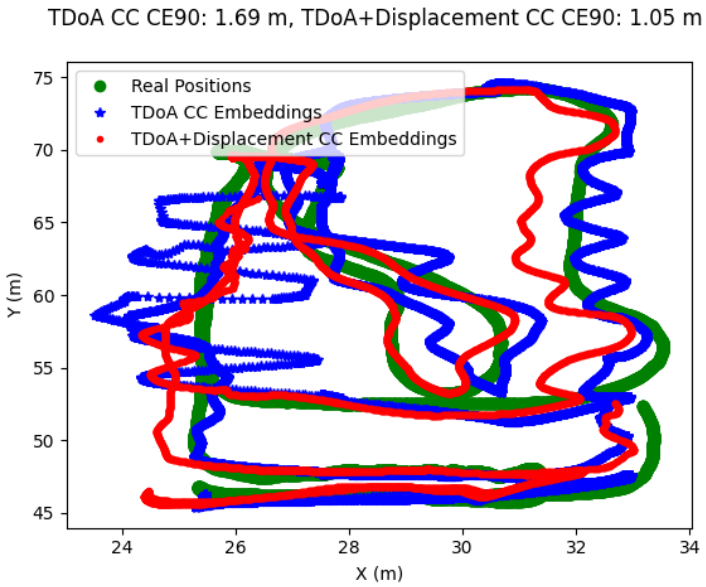

Figure 7.15: Simulated CC embeddings with NLoS masking fixed at $\lambda = 0.2$

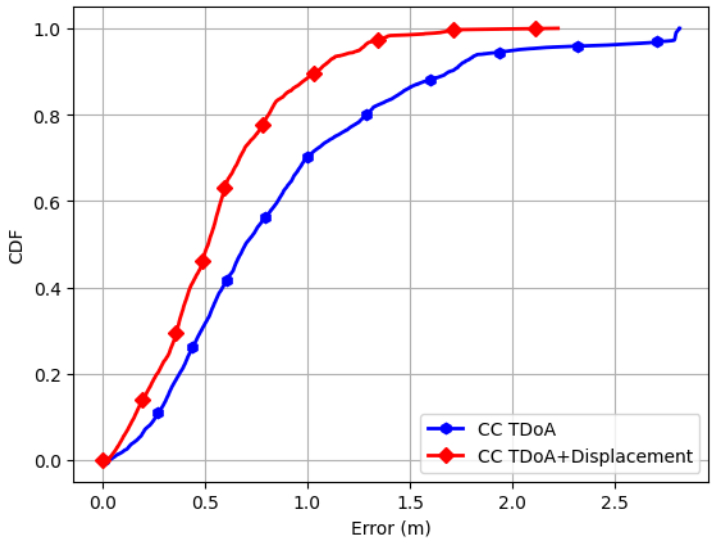

Figure 7.16: Simulated CDF NLoS masking with fixed $\lambda = 0.2$

Table 7.2 exhibits the quantitative and qualitative performance of our CC with TDoA and TDoA+Displacement models. On the quantitative side, key metrics in CC literature include Continuity (CT), which measures how well spatial relationships are preserved in the embedded space, and Trustworthiness (TW), which assesses whether embedded similarities correspond to actual proximity in the original space. Kruskal Stress (KS) is a distortion metric that measures how well the distances in the embeddings match the true distances in the original high-dimensional space. Lower distortion measured by KS means better embedding. All factors are described repeatedly in other works, such as in [110]. Another metric, the Cumulative Distribution Function (CDF) of the localization error at the 90th percentile (CE90), reflects both localization accuracy and the distribution of errors across positions. On the qualitative side, visual inspection of the embedded space against RTK estimated trajectory provides an additional check, ensuring that the model captures meaningful geometrical patterns and relationships within the data.

The benefit of including displacement information can be seen by comparing Figure 7.17 and Figure 7.18, which show the performance of the TDoA-CC method and the joint TDoA+Displacement CC method, respectively. While the TDoA-CC achieves acceptable results with about 2 m accuracy at the 90% point of the CDF, the joint method improves this to 1.8 m, with both evaluated under raw and mostly LoS conditions. The joint approach also yields more stable results, with reduced fluctuations even in the raw embeddings. To further enhance stability, the raw embeddings of both methods, shown in blue dots, are smoothed using a moving-average window of size 10 that is shown with red dots on the figures, while the green dots are the RTK ground truth positions.

It is important to note that relying solely on displacement measurements for positioning does not yield accurate trajectory estimation, since sensor-based displacement measurements inevitably accumulate the noise and bias introduced in Section 7.3 over time. An example of this growing bias is depicted in Figure 7.19. Consequently, velocity measurements and the corresponding displacement estimates remain reliable only over short intervals, where both noise and bias are limited.

Therefore, in this work, the displacement loss is used only to mitigate fluctuations in cases where a limited number of TDoA measurements are available during training. Finally, Figure 7.20 and Figure 7.21 are results of the CC with only TDoA loss function and with joint TDoA and displacement losses, respectively. Under various r_{LoS}, CC experiences more resilience by NLoS masking and adding displacement measurements. The positioning error in the GEO-5G testbed varies around 2-4 meters under variable LoS ratios, which is a significant improvement compared to the state-of-the-art CC and conventional TDoA-based methods.

$\%r_{\mathbf{LoS}}$	**CT**	**TW**	**KS**	**CE90 (m)**	**MAE (m)**
100	0.9751	0.9722	0.1762	2.04	1.35
	0.9838	**0.9796**	**0.1569**	**1.80**	**1.24**
75	0.9699	0.9529	0.2216	2.75	1.64
	0.9796	**0.9722**	**0.2145**	**1.92**	**1.42**
50	0.9389	0.9312	0.2666	4.12	2.42
	0.9717	**0.9442**	**0.2525**	**3.50**	**1.70**
25	0.9365	0.8655	0.3502	5.16	2.91
	0.9595	**0.8966**	**0.3187**	**3.86**	**2.60**

Table 7.2: GEO-5G testbed: Comparison of TDoA and **TDoA+Displacement** CC metrics while RTK is assumed to be the true position

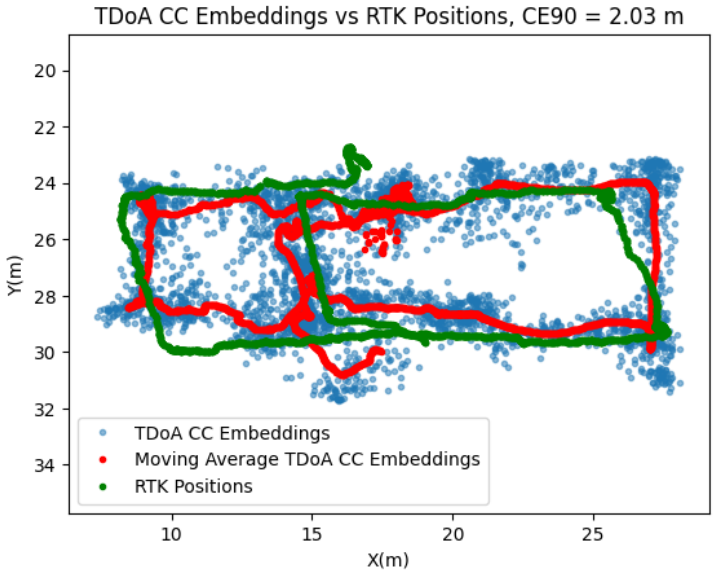

Figure 7.17: GEO-5G testbed: LoS TDoA CC embeddings with $r_{\text{LoS}} = 100\%$

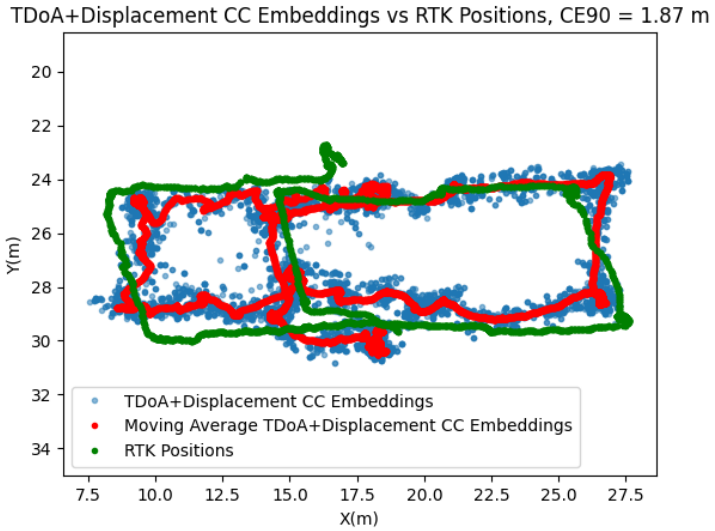

Figure 7.18: GEO-5G testbed: TDoA+Displacement CC embeddings with $r_{\text{LoS}} = 100\%$

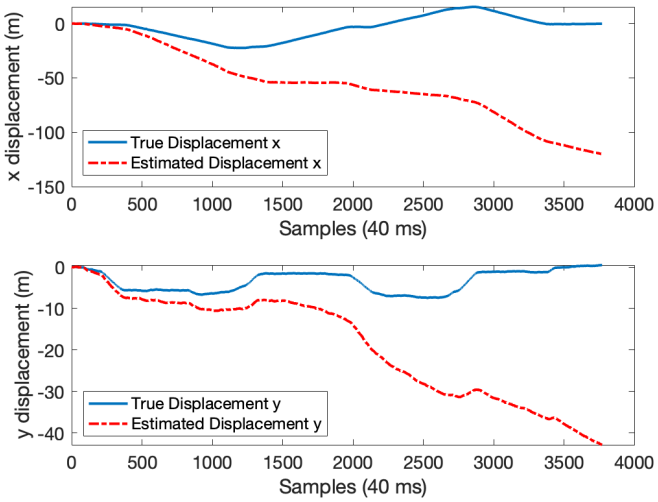

Figure 7.19: Displacement bias growing over time

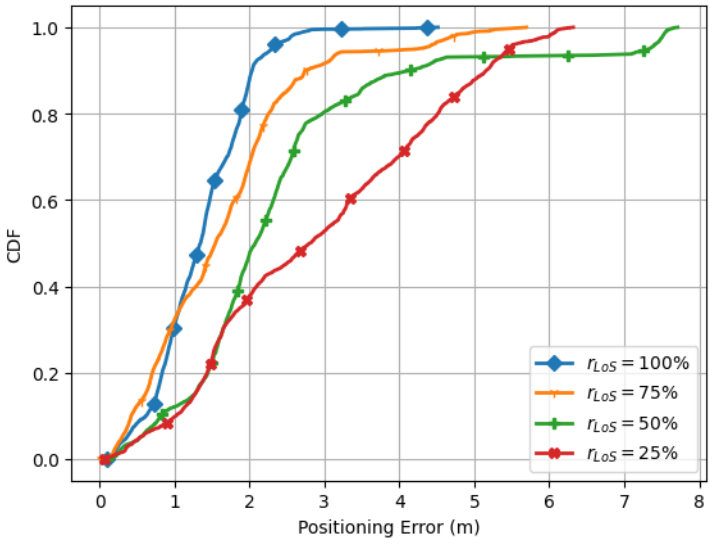

Figure 7.20: GEO-5G testbed: TDoA CC error at GEO-5G testbed

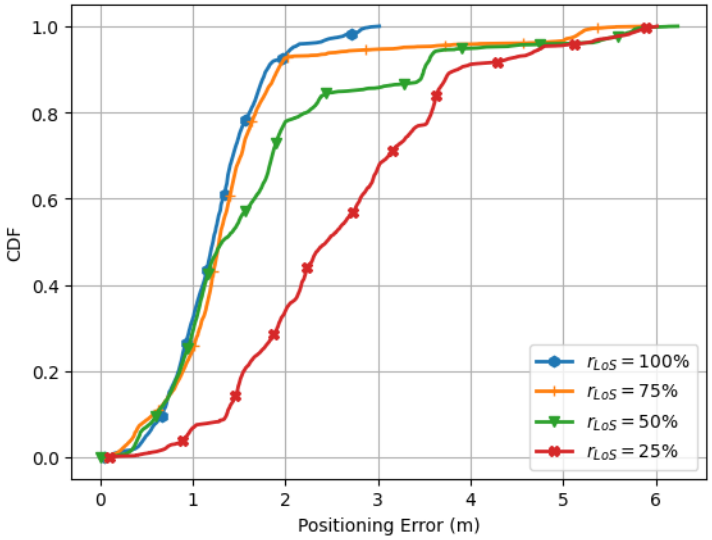

Figure 7.21: GEO-5G testbed: TDoA+Displacement CC error at GEO-5G testbed

7.8 Conclusions

In this work, we presented a self-supervised CC model for UE positioning in mixed LoS/NLoS conditions. The proposed method does not require ground-truth labels for training or any coordinate scaling, and operates in a global reference frame by exploiting only the known TRP locations, TDoA, and CIR data. Its performance is further improved in scenarios with limited LoS TRP availability by incorporating UE displacement measurements. The model was evaluated both in MATLAB simulations and in the real world GEO-5G positioning testbed at EURECOM using commercial O-RAN RUs and an OAI core network. Results of predicted positions from our joint TDoA+Displacement model compared to RTK positioning, show an accuracy of 2–4 m in 90% of the time, across scenarios with 100% to 25% LoS probability. The dataset of recorded CIRs, as well as RTK measurements to be used as ground truth positions, is publicly available for further research. As part of our future work, we plan to complete the integration of the E2 interface and conduct a performance evaluation of the proposed positioning system on the Near-Real-Time RIC based on OAI.

Chapter 8

Conclusions and Future Perspectives

8.1 Conclusions

This dissertation focused on research and development of positioning functionalities in standard and beyond-standard 5G NR cellular systems. Accurate positioning of a mobile UE in such a system is a procedure that involves multiple network nodes performing a chain of computations and interactions in real-time. Our positioning methods are mainly built on accurate time estimation assumptions, such as TDoA with nanoseconds precision from UL SRS signal in FR1. While the real-world network deployments involve hardware impairments, this work proposed tailored filtering methods to mitigate the effect of noise from outlier measurements. One of the highlights of this work was the employment of the NRPPa protocol to carry the TRP measurement and information to the 5G CN. On the CN, LMF is the next essential component, which was integrated with OAI in this work for the first time. We compared numerous state-of-the-art methods in position estimation and chose the best candidates to be implemented on the LMF. The performance of our positioning algorithms was evaluated in both simulation and real 5G testbeds in both outdoor and indoor scenarios. In this dissertation, novel CC models for 5G positioning with sensor fusion were also introduced that exploit non-conventional measurements such as CIR in an O-RAN framework beyond 5G standards.

A summary of the contributions in each chapter is as follows:

- Chapter 1 introduces the background of positioning systems, the evolution of measurements and methods in cellular networks with 5G enhancements, and outlines the objectives of the GEO-5G project motivating this dissertation.
- Chapter 2 gives a generic and standard background on the 3GPP and ORAN frameworks that we follow for 5G position estimation. Also, it presents the progressive research methodology of this dissertation in a summary.
- Chapter 3 has presented the fundamentals of UE positioning in 5G NR networks. By examining TDoA and AoD of DL PRS within a mmWave MIMO simulation framework, we have demonstrated the potential of 5G-based positioning in a standardized indoor factory hall scenario.
- Chapter 4 takes the first steps toward implementing an end-to-end 5G NR positioning system using OAI RFsim. The work emulates the main components of a standardized positioning architecture, including the OAI-UE, OAI-gNB, a lightweight protocol placeholder for NRPPa, and a localization algorithm implemented in the MATLAB environment.

- Chapter 5 has presented the successful results of three positioning testbeds that integrate the first open-source NRPPa and LMF into OAI. The primary contribution of this chapter lies in the design and implementation of the localization pipeline within the LMF.
- Chapter 6 proposes channel charting for localization by CIR measurements, which is beyond the standard 5G approach. Although CIR cannot be transferred to the LMF through NRPPa, this chapter shows the potential of data-driven positioning with only 2 LoS TRPs, especially when enhanced with sensor fusion.
- Chapter 7, extends the previous work on channel charting by adopting a more practical approach that exploits TDoA measurements together with TRP locations to derive a position estimation function. Both simulation results and experiments on the GEO-5G testbed demonstrate that the proposed channel charting method enables accurate UE localization under mixed LoS/NLoS conditions.

8.2 Future Perspectives

While this dissertation has explored key aspects of 5G NR positioning through testbed implementations and data-driven approaches, several potential directions remain open for future research.

First, the integration of the CC method with the E2 interface and the RIC on OAI is currently in progress. In addition, future evaluations could involve training the model on larger datasets to better assess its performance.

Secondly, extending the evaluations to FR2 and mmWave frequency bands will be essential to fully capture the benefits of wide bandwidths and narrow beams. These bands offer higher resolution for time and angle-based measurements, but they also introduce new challenges due to hardware impairments, blockage sensitivity, and more dynamic propagation conditions [119, 120]. Also, incorporating beamforming and advanced AoA/AoD estimation techniques can further enhance positioning accuracy. Although these aspects were thoroughly investigated in Chapter 2, practical validation did not take place due to limitations of the OAI software and the available equipment. However, it was shown that leveraging multi-antenna arrays and directional transmission will enable finer spatial resolution, which is critical in dense-multipath environments such as factories and urban canyons [121, 122].

Finally, sidelink-based collaborative positioning represents a significant opportunity beyond traditional network-centric approaches. By enabling UEs to exchange measurements directly, sidelink can improve coverage, robustness, and accuracy in scenarios where infrastructure-based positioning is limited. Integrating sidelink with the proposed data-driven frameworks could pave the way for resilient beyond-5G localization systems [123–125].

Together, these directions highlight a path toward more accurate, reliable, and scalable positioning solutions in future 5G and 6G networks.

Bibliography

[1] Elliott D. Kaplan and Christopher J. Hegarty. *Understanding GPS: Principles and Applications*. 2nd. Boston, MA: Artech House, 2005. ISBN: 9781580538947.

[2] Pratap Misra and Per Enge. *Global Positioning System: Signals, Measurements, and Performance*. 2nd. See Chapter 7, Sections 7.2.1 to 7.3 for discussion on urban canyon and indoor limitations due to signal blockage and multipath. Lincoln, MA: Ganga-Jamuna Press, 2006. ISBN: 9780970954428.

[3] Faheem Zafari, Athanasios Gkelias, and Kin K. Leung. "A Survey of Indoor Localization Systems and Technologies". In: *IEEE Communications Surveys & Tutorials* 21.3 (2019), pp. 2568–2599. DOI: 10.1109/COMST.2019.2911558.

[4] *3GPP TS 38.211: 5G; NR; Physical Channels and Modulation*. Tech. rep. 3rd Generation Partnership Project (3GPP), 2019.

[5] *3GPP TS 43.059: Functional stage 2 description of Location Services (LCS) in GERAN*. Tech. rep. Available at https://www.3gpp.org. 3rd Generation Partnership Project (3GPP), 2009.

[6] *3GPP TS 25.305: Stage 2 functional specification of User Equipment positioning in UTRAN*. Tech. rep. Available at https://www.3gpp.org. 3rd Generation Partnership Project (3GPP), 2006.

[7] *3GPP TS 36.305: Stage 2 functional specification of UE positioning in E-UTRAN*. Tech. rep. Available at https://www.3gpp.org. 3rd Generation Partnership Project (3GPP), 2019.

[8] Mike Koivisto et al. "High-Efficiency Device Positioning and Location-Aware Communications in Dense 5G Networks". In: *IEEE Communications Magazine* 55.8 (2017), pp. 188–195. DOI: 10.1109/MCOM.2017.1600584CM.

[9] Karthik Muthineni et al. "A Survey of 5G-Based Positioning for Industry 4.0: State of the Art and Enhanced Techniques". In: *arXiv preprint arXiv:2409.13308* (2024).

[10] Sharief Saleh et al. "Integration of 5G and Motion Sensors for Vehicular Positioning: A Loosely-Coupled Approach". In: *arXiv preprint arXiv:2403.10872* (2024).

[11] M. Majid Butt, Anna Pantelidou, and István Z. Kovács. "ML-Assisted UE Positioning: Performance Analysis and 5G Architecture Enhancements". In: *IEEE Open Journal of Vehicular Technology* 2 (2021), pp. 377–388. DOI: 10.1109/OJVT.2021.3110134.

[12] Sinan Gezici et al. "Localization via ultra-wideband radios: a look at positioning aspects for future sensor networks". In: *IEEE Signal Processing Magazine* 22.4 (2005), pp. 70–84. DOI: 10.1109/MSP.2005.1458287.

[13] Fredrik Gustafsson and Fredrik Gunnarsson. "Mobile positioning using wireless networks: possibilities and fundamental limitations based on available wireless network measurements". In: *IEEE Signal Processing Magazine* 19.6 (2002), pp. 41–53. DOI: 10.1109/MSP.2002.1049987.

[14] M. Sanjeev Arulampalam et al. "A tutorial on particle filters for online nonlinear/non-Gaussian Bayesian tracking". In: *IEEE Transactions on Signal Processing* 50.2 (2002), pp. 174–188. DOI: 10.1109/78.978374.

[15] Simon J. Julier and Jeffrey K. Uhlmann. "A new extension of the Kalman filter to nonlinear systems". In: *Signal Processing, Sensor Fusion, and Target Recognition VI*. Vol. 3068. SPIE. 1997, pp. 182–193. DOI: 10.1117/12.280797.

[16] James Kennedy and Russell Eberhart. "Particle swarm optimization". In: *Proceedings of ICNN'95 - International Conference on Neural Networks*. Vol. 4. IEEE. 1995, pp. 1942–1948. DOI: 10.1109/ICNN.1995.488968.

[17] David E. Goldberg. *Genetic Algorithms in Search, Optimization, and Machine Learning*. Addison-Wesley, 1989. ISBN: 978-0201157673.

[18] S. Kirkpatrick, C. D. Gelatt, and M. P. Vecchi. "Optimization by Simulated Annealing". In: *Science* 220.4598 (1983), pp. 671–680. DOI: 10.1126/science.220.4598.671.

[19] Rainer Storn and Kenneth Price. "Differential Evolution—a simple and efficient heuristic for global optimization over continuous spaces". In: *Journal of Global Optimization* 11.4 (1997), pp. 341–359. DOI: 10.1023/A:1008202821328.

[20] Christoph Studer et al. "Channel Charting: Locating users within the radio environment using channel state information". In: *IEEE Transactions on Wireless Communications* 18.1 (2019), pp. 64–77. DOI: 10.1109/TWC.2018.2879340.

[21] 3GPP. *NG Radio Access Network (NG-RAN); Stage 2 functional specification of User Equipment (UE) positioning in NG-RAN*. Technical Specification 3GPP TS 38.305. Version 16.1.0 Release 16. 3GPP, 2020.

[22] FIRECELL. *Private 4G/5G Networks*. https://www.firecell.io/. Accessed: 2025-07-16.

[23] Mohsen Ahadi and Florian Kaltenberger. "5GNR Indoor Positioning By Joint DL-TDoA and DL-AoD". In: *2023 IEEE Wireless Communications and Networking Conference (WCNC)*. 2023. DOI: 10.1109/WCNC55385.2023.10119056.

[24] Adeel Malik et al. "From Concept to Reality: 5G Positioning with UL-TDoA in OpenAirInterface". In: *IEEE INFOCOM 2025 - IEEE Conference on Computer Communications Workshops (INFOCOM WKSHPS)*. 2025, pp. 1–6. DOI: 10.1109/INFOCOMWKSHPS65812.2025.11152876.

[25] *3GPP TS 38.305: NR; Stage 2 functional specification of UE positioning*. Tech. rep. TS 38.305. Available at https://www.3gpp.org. 3rd Generation Partnership Project (3GPP), 2024.

[26] *3GPP TS 38.211: NR; Physical channels and modulation*. Tech. rep. TS 38.211. Available at https://www.3gpp.org. 3rd Generation Partnership Project (3GPP), 2024.

[27] *3GPP TS 38.455: NR; NR Positioning Protocol A (NRPPa)*. Tech. rep. TS 38.455. Available at https://www.3gpp.org. 3rd Generation Partnership Project (3GPP), 2024.

[28] 3GPP. *NG Radio Access Network (NG-RAN); Stage 2 functional specification of User Equipment (UE) positioning in NG-RAN*. Technical Specification 3GPP TS 38.305. Version 17.0.0 Release 17. 2022.

[29] *3GPP TS 23.501: System architecture for the 5G System (5GS); Stage 2*. Tech. rep. TS 23.501. Available at https://www.3gpp.org. 3rd Generation Partnership Project (3GPP), 2024.

[30] *3GPP TS 37.355: E-UTRA; LTE Positioning Protocol (LPP)*. Tech. rep. TS 37.355. Available at https://www.3gpp.org. 3rd Generation Partnership Project (3GPP), 2024.

[31] O-RAN Alliance. *O-RAN: Towards an Open and Smart RAN*. Tech. rep. White Paper, Available: https://www.o-ran.org/resources. O-RAN Alliance, 2020.

[32] *3GPP TR 38.901: Study on Channel Model for Frequencies from 0.5 to 100 GHz*. Tech. rep. 3rd Generation Partnership Project (3GPP), 2019.

[33] OpenAirInterface (OAI). *RF Simulator (RFSIM) README*. https://gitlab.eurecom.fr/oai/openairinterface5g/-/blob/develop/radio/rfsimulator/README.md. Accessed: 2025-09-01. May 2025.

[34] D. Wang and G. Hosangadi and P. Monogioudis and A. Rao. "Mobile Device Localization in 5G Wireless Networks". In: *Proc. Int. Conf. on Computing, Networking and Communications (ICNC)*. 2019.

[35] T.-K. Le and N. Ono. "Closed-Form and Near Closed-Form Solutions for TOA-Based Joint Source and Sensor Localization". In: *IEEE Transactions on Signal Processing* 64 (2016).

[36] N. H. Nguyen and K. Dogancay. "Optimal Geometry Analysis for Multistatic TOA Localization". In: *IEEE Transactions on Signal Processing* 64 (2016).

[37] D. Munoz and C. Vargas and R. Enriquez-Caldera and F. B. Lara. *Position Location Techniques and Applications*. Academic Press, 2009.

[38] P. Tarrio and A. M. Bernardos and J. A. Besada and J. R. Casar. "A New Positioning Technique for RSS-Based Localization Based on a Weighted Least Squares Estimator". In: *Proc. IEEE Int. Symp. on Wireless Communication Systems (ISWCS)*. 2008.

[39] T. Stoyanova and F. Kerasiotis and C. Antonopoulos and G. Papadopoulos. "RSS-Based Localization for Wireless Sensor Networks in Practice". In: *Proc. 9th Int. Symp. on Communication Systems, Networks and Digital Signal Processing (CSNDSP)*. 2014.

[40] J. A. del Peral-Rosado and R. Raulefs and J. A. Lopez-Salcedo and G. Seco-Granados. "Survey of Cellular Mobile Radio Localization Methods: From 1G to 5G". In: *IEEE Communications Surveys & Tutorials* 20 (2018), pp. 1124–1148.

[41] S. Wong and R. Jassemi-Zargani and D. Brookes and B. Kim. *A Geometric Approach to Passive Target Localization*. Tech. rep. ST Organization, 2017.

[42] Y. T. Chan and K. C. Ho. "A Simple and Efficient Estimator for Hyperbolic Location". In: *IEEE Transactions on Signal Processing* 42.8 (1994), pp. 1905–1915.

[43] Y. Huang and J. Benesty and G. W. Elko and R. M. Mersereau. "Real-Time Passive Source Localization: A Practical Linear-Correction Least-Squares Approach". In: *IEEE Transactions on Speech and Audio Processing* 9.8 (2001), pp. 943–956.

[44] K. W. Cheung and H. C. So and W. K. Ma and Y. T. Chan. "A Constrained Least Squares Approach to Mobile Positioning: Algorithms and Optimality". In: *EURASIP Journal on Applied Signal Processing* (2006).

[45] K. Yang and J. An. "Constrained Total Least-Squares Location Algorithm Using Time-Difference-of-Arrival Measurements". In: *IEEE Transactions on Vehicular Technology* 59.3 (2010).

[46] W. Chen and S. He and Q. Xu and J. Ren and Y. Huang and L. Yang. "Positioning Algorithm and AoD Estimation for mmWave FD-MISO System". In: *Proc. 10th Int. Conf. on Wireless Communications and Signal Processing (WCSP)*. 2018, pp. 1–6. DOI: 10.1109/WCSP.2018.8555713.

[47] *3GPP TS 38.305: 5G; NG-RAN; Stage 2 Functional Specification of User Equipment (UE) Positioning in NG-RAN*. Tech. rep. 3rd Generation Partnership Project (3GPP), 2019.

[48] *3GPP TS 37.355: LTE; 5G; LTE Positioning Protocol (LPP)*. Tech. rep. 3rd Generation Partnership Project (3GPP), 2019.

[49] *3GPP TS 38.211: 5G; NR; Physical Channels and Modulation*. Tech. rep. 3rd Generation Partnership Project (3GPP), 2019.

[50] S. He and J. Wang and Y. Huang and B. Ottersten and W. Hong. "Codebook-Based Hybrid Precoding for Millimeter Wave Multiuser Systems". In: *IEEE Transactions on Signal Processing* 65.20 (2017), pp. 5289–5304.

[51] *3GPP TR 38.802: Study on New Radio Access Technology Physical Layer Aspects*. Tech. rep. 3rd Generation Partnership Project (3GPP), 2017.

[52] *3GPP TS 38.215: NR Physical Layer Measurements*. Tech. rep. 3rd Generation Partnership Project (3GPP), 2019.

[53] J.-J. van de Beek and O. Edfors and M. Sandell and S. K. Wilson and P. O. Borjesson. "On Channel Estimation in OFDM Systems". In: *Proc. IEEE Vehicular Technology Conference (VTC)*. 1995, pp. 815–819. DOI: 10.1109/VETEC.1995.504981.

[54] W. H. Foy. "Position-Location Solutions by Taylor-Series Estimation". In: *IEEE Transactions on Aerospace and Electronic Systems* AES-12 (1976), pp. 187–194.

[55] S. M. Kay. *Fundamentals of Statistical Signal Processing: Detection Theory*. Vol. 2. Englewood Cliffs, NJ: Prentice-Hall, 1998.

[56] S. Sosnin and A. Lomayev and A. Khoryaev. "DL-AoD Positioning Algorithm for Enhanced 5G NR Location Services". In: *Proc. Int. Conf. on Indoor Positioning and Indoor Navigation (IPIN)*. 2021, pp. 1–7. DOI: 10.1109/IPIN51156.2021.9662638.

[57] *3GPP TR 38.901: Study on Channel Model for Frequencies from 0.5 to 100 GHz*. Tech. rep. 3rd Generation Partnership Project (3GPP), 2017.

[58] D. Wang and G. Hosangadi and P. Monogioudis and A. Rao. "Mobile Device Localization in 5G Wireless Networks". In: *International Conference on Computing, Networking and Communications (ICNC)*. 2019.

[59] R. Keating and M. Säily and J. Hulkkonen and J. Karjalainen. "Overview of Positioning in 5G New Radio". In: *2019 16th International Symposium on Wireless Communication Systems (ISWCS)*. Oulu, Finland, 2019, pp. 320–324. DOI: 10.1109/ISWCS.2019.8877160.

[60] *3GPP TS 38.305: 5G; NG-RAN; Stage 2 Functional Specification of User Equipment (UE) Positioning in NG-RAN*. Tech. rep. 3rd Generation Partnership Project (3GPP), 2019.

[61] R. M. Vaghefi and R. M. Buehrer. "Cooperative Localization in NLOS Environments Using Semidefinite Programming". In: *IEEE Communications Letters* 19.8 (2015), pp. 1382–1385. DOI: 10.1109/LCOMM.2015.2434393.

[62] G. Naddafzadeh-Shirazi and M. B. Shenouda and L. Lampe. "Second Order Cone Programming for Sensor Network Localization with Anchor Position Uncertainty". In: *IEEE Transactions on Wireless Communications* 13.2 (2014), pp. 749–763. DOI: 10.1109/TWC.2013.122113.130303.

[63] A. R. Destiarti and P. Kristalina and A. Sudarsono. "Mobile Cooperative Tracking with RSSI Ranging in EKF Algorithm for Indoor Wireless Sensor Network". In: *2016 International Conference on Knowledge Creation and Intelligent Computing (KCIC)*. 2016, pp. 60–66. DOI: 10.1109/KCIC.2016.7992649.

[64] W. Wang and D. Marelli and M. Fu. "Dynamic Indoor Localization Using Maximum Likelihood Particle Filtering". In: *Sensors* 21.4 (2021), p. 1090. DOI: 10.3390/s21041090.

[65] I. Palamà and S. Bartoletti and G. Bianchi and N. B. Melazzi. "5G Positioning with SDR-Based Open-Source Platforms: Where Do We Stand?" In: *2022 IEEE 11th IFIP International Conference on Performance Evaluation and Modeling in Wireless and Wired Networks (PEMWN)*. 2022, pp. 1–6. DOI: 10.23919/PEMWN56085.2022.9963853.

[66] J. He and H. C. So. "A Hybrid TDoA-Fingerprinting-Based Localization System for LTE Network". In: *IEEE Sensors Journal* 20.22 (2020), pp. 13653–13665. DOI: 10.1109/JSEN.2020.3004179.

[67] A. Pinto and G. Santaromita and C. Fiandrino and D. Giustiniano and F. Esposito. "Characterizing Location Management Function Performance in 5G Core Networks". In: *2022 IEEE Conference on Network Function Virtualization and Software Defined Networks (NFV-SDN)*. 2022, pp. 66–71. DOI: 10.1109/NFV-SDN56302.2022.9974927.

[68] J. Kennedy and R. Eberhart. "Particle Swarm Optimization". In: *Proc. Int. Conf. Neural Networks (ICNN)*. Perth, WA, Australia, 1995, pp. 1942–1948.

[69] M. Ahadi and F. Kaltenberger. "5G NR Indoor Positioning by Joint DL-TDoA and DL-AoD". In: *2023 IEEE Wireless Communications and Networking Conference (WCNC)*. Glasgow, United Kingdom, 2023, pp. 1–6. DOI: 10.1109/WCNC55385.2023.10119056.

[70] . "ToA and DOA Based Positioning". In: *Handbook of Position Location: Theory, Practice, and Advances*. IEEE, 2019, pp. 197–198. DOI: 10.1002/9781119434610.part2.

[71] Adeel Malik and Mohsen Ahadi and Florian Kaltenberger and Klaus Warnke and Nguyen Tien Thinh and Nada Bouknana and Cedric Thienot and Godswill Onche and Sagar Arora. *From Concept to Reality: 5G Positioning with Open-Source Implementation of UL-TDoA in OpenAirInterface*. 2025. arXiv: 2409.05217 [cs.IT]. URL: https://arxiv.org/abs/2409.05217.

[72] 3GPP. *NG-RAN; NR Positioning Protocol A (NRPPa)*. TS 38.455 v16.1.0. NG-RAN; positioning signaling between gNB and LMF. 2020.

[73] 3GPP. *5G; System; Location Management Services*. TS 29.572 v17.4.0. Defines LMF and its service-based interface (Nlmf_Location). 2022.

[74] Florian Kaltenberger et al. *Driving innovation in 6G wireless technologies: The OpenAirInterface approach*. ArXiV:2412.13295. Dec. 2024. URL: https://arxiv.org/abs/2412.13295.

[75] Rakesh Mundlamuri et al. "5G NR Positioning with OpenAirInterface: Tools and Methodologies". In: *2025 20th Wireless On-Demand Network Systems and Services Conference (WONS)*. 2025, pp. 1–7.

[76] Samuele Zanini et al. "Towards End-to-end Implementation of 5G Positioning with Off-the-shelf Devices". In: *2024 IEEE 100th Vehicular Technology Conference (VTC2024-Fall)*. 2024, pp. 1–6. DOI: 10.1109/VTC2024-Fall63153.2024.10757829.

[77] Li, Dexin and Chu, Xinghe and Wang, Luhan and Lu, Zhaoming and Zhou, Shuya and Wen, Xiangming. "Performance Evaluation of E-CID based Positioning on OAI 5G-NR Testbed". In: *2022 IEEE/CIC International Conference on Communications in China (ICCC)*. 2022, pp. 832–837. DOI: 10.1109/ICCC55456.2022.9880817.

[78] del Peral-Rosado, José A. and Yildirim, Ali Y. and Klinger, Nils C. and Nolle, Patric and Razavi, Sara M. and Parsawar, Sagar and Mundlamuri, Rakesh and Kaltenberger, Florian and Sirola, Niilo and Garlaschi, Stefano and Canzian, Luca and Talvitie, Jukka and Flachs, Detlef. "Preliminary Field Results of a Dedicated 5G Positioning Network for Enhanced Hybrid Positioning". In: *Engineering Proceedings* 54.1 (2023). ISSN: 2673-4591. DOI: 10.3390/ENC2023-15432. URL: https://www.mdpi.com/2673-4591/54/1/6.

[79] Rajeev Gangula and Tommaso Melodia and Rakesh Mundlamuri and Florian Kaltenberger. *Round Trip Time Estimation Utilizing Cyclic Shift of Uplink Reference Signal*. 2024. arXiv: 2410.04528 [cs.IT]. URL: https://arxiv.org/abs/2410.04528.

[80] Michele Gucciardo et al. "A Flexible 4G/5G Control Platform for Fingerprint-based Indoor Localization". In: *IEEE INFOCOM 2019 - IEEE Conference on Computer Communications Workshops (INFOCOM WKSHPS)*. 2019, pp. 744–749. DOI: 10.1109/INFCOMW.2019.8845272.

[81] Lin, Yu-Tai and Matson, N. Cameron and Sundaresan, Karthikeyan. "Bringing Collaborative Positioning to Native 5G Systems for Enhanced 2D & 3D Location Services". In: *Proc. ACM Netw.* 2.CoNEXT4 (Nov. 2024). DOI: 10.1145/3696380. URL: https://doi.org/10.1145/3696380.

[82] Palamà, Ivan and Bartoletti, Stefania and Bianchi, Giuseppe and Blefari Melazzi, Nicola. "Experimental assessment of SDR-based 5G positioning: methodologies and insights". In: *Annals of Telecommunications* 79.5 (2024), pp. 301–313.

[83] Ettus Research. *USRP Software Defined Radio (SDR)*. https://www.ettus.com/. Accessed: 2025-07-16.

[84] VVDN Technologies. *5G NR Enterprise Radio Units*. https://www.vvdntech.com.

[85] Pratap Misra and Per Enge. *Global Positioning System: Signals, Measurements and Performance*. 2nd. Ganga-Jamuna Press, 2011.

[86] Xinrong Li and K. Pahlavan. "Super-resolution TOA estimation with diversity for indoor geolocation". In: *IEEE Transactions on Wireless Communications* 3.1 (2004), pp. 224–234. DOI: 10.1109/TWC.2003.819035.

[87] Mohamed A. Khamsi and William A. Kirk. *An Introduction to Metric Spaces and Fixed Point Theory*. The Triangle Inequality in $\mathbb{R}^n$. Wiley-IEEE, 2001. Chap. 1.4. ISBN: 0-471-41825-0.

[88] Mohsen Ahadi et al. "5G NR UL SRS TDoA Positioning by OpenAirInterface." In: 2023.

[89] F. Gustafsson and F. Gunnarsson. "Positioning using time-difference of arrival measurements". In: *IEEE International Conference on Acoustics, Speech, and Signal Processing, 2003. Proceedings. (ICASSP '03).*

[90] Chan, Y.T. and Ho, K.C. "A simple and efficient estimator for hyperbolic location". In: *IEEE Transactions on Signal Processing* 42.8 (1994), pp. 1905–1915. DOI: 10.1109/78.301830.

[91] Ahasanun Nessa et al. "A Survey of Machine Learning for Indoor Positioning". In: *IEEE Access* 8 (2020). DOI: 10.1109/ACCESS.2020.3039271.

[92] Paul Ferrand et al. "Wireless channel charting: Theory, practice, and applications". In: *IEEE Communications Magazine* 61.6 (2023), pp. 124–130.

[93] Laurens Van Der Maaten, Eric O Postma, H Jaap van den Herik, et al. "Dimensionality reduction: A comparative review". In: *Journal of Machine Learning Research* 10.66-71 (2009), p. 13.

[94] Christoph Studer et al. "Channel Charting: Locating Users Within the Radio Environment Using Channel State Information". In: *IEEE Access* 6 (). DOI: 10.1109/ACCESS.2018.2866979.

[95] Junquan Deng et al. "Multipoint Channel Charting for Wireless Networks". In: *2018 52nd Asilomar Conference on Signals, Systems, and Computers*. DOI: 10.1109/ACSSC.2018.8645281.

[96] Chunhua Geng, Howard Huang, and Jack Langerman. "Multipoint Channel Charting With Multiple-Input Multiple-Output Convolutional Autoencoder". In: *2020 IEEE/ION Position, Location and Navigation Symposium*. DOI: 10.1109/PLANS46316.2020.9109875.

[97] Pengzhi Huang et al. "Improving Channel Charting with Representation-Constrained Autoencoders". In: *2019 IEEE 20th International Workshop on Signal Processing Advances in Wireless Communications (SPAWC)* ().

[98] Patrick Agostini et al. "Not-Too-Deep Channel Charting (N2D-CC)". In: *IEEE Wireless Communications and Networking Conference (WCNC)*. 2022. DOI: 10.1109/WCNC51071.2022.9771913.

[99] Eric Lei et al. "Siamese Neural Networks for Wireless Positioning and Channel Charting". In: *2019 57th Annual Allerton Conference on Communication, Control, and Computing (Allerton)*.

[100] Paul Ferrand et al. "Triplet-Based Wireless Channel Charting: Architecture and Experiments". In: *IEEE Journal on Selected Areas in Communications* 39.8 (2021). DOI: 10.1109/JSAC.2021.3087251.

[101] Euchner, Florian and Stephan, Phillip and Gauger, Marc and Dörner, Sebastian and Ten Brink, Stephan. "Improving Triplet-Based Channel Charting on Distributed Massive MIMO Measurements". In: *IEEE 23rd International Workshop on Signal Processing Advances in Wireless Communication (SPAWC)*. 2022. DOI: 10.1109/SPAWC51304.2022.9833925.

[102] Maximilian Stahlke et al. "Indoor Localization With Robust Global Channel Charting: A Time-Distance-Based Approach". In: *IEEE Transactions on Machine Learning in Communications and Networking* 1 (2023), pp. 3–17. DOI: 10.1109/TMLCN.2023.3256964.

[103] Amr Aly and Ender Ayanoglu. "Estimation of Cellular Wireless User Coordinates via Channel Charting and MUSIC". In: *2023 International Conference on Computing, Networking and Communications (ICNC)*.

[104] Florian Euchner, Phillip Stephan, and Stephan ten Brink. "Augmenting Channel Charting with Classical Wireless Source Localization Techniques". In: *2023 57th Asilomar Conference on Signals, Systems, and Computers*. 2023. DOI: 10.1109/IEEECONF59524.2023.10477049.

[105] Maximilian Stahlke et al. *Velocity-Based Channel Charting with Spatial Distribution Map Matching*. 2023. arXiv: 2311.08016 [eess.SP].

[106] Sueda Taner, Victoria Palhares, and Christoph Studer. "Channel Charting in Real-World Coordinates". In: *2023 IEEE Global Communications Conference*.

[107] Rakesh Mundlamuri and Rajeev Gangula and Florian Kaltenberger and Raymond Knopp. "Novel Round Trip Time Estimation in 5G NR". In: *2024 IEEE Global Communications Conference: Wireless Communications (Globecom 2024 WC)*. Cape Town, South Africa.

[108] Paul J Besl and Neil D McKay. "Method for registration of 3-D shapes". In: *Sensor fusion IV: control paradigms and data structures*. Vol. 1611.

[109] J. Kennedy and R. Eberhart. "Particle swarm optimization". In: *Proceedings of ICNN'95 - International Conference on Neural Networks*. Vol. 4. 1995, 1942–1948 vol.4. DOI: 10.1109/ICNN.1995.488968.

[110] AL-Tous, Hanan and Kazemi, Parham and Studer, Christoph and Tirkkonen, Olav. "Channel Charting with Angle-Delay-Power-Profile Features and Earth-Mover Distance". In: *2022 56th Asilomar Conference on Signals, Systems, and Computers*. 2022. DOI: 10.1109/IEEECONF56349.2022.10052099.

[111] Esrafilian, Omid and Ahadi, Mohsen and Kaltenberger, Florian and Gesbert, David. "Global Scale Self-Supervised Channel Charting with Sensor Fusion". In: *2024 IEEE Globecom Workshops (GC Wkshps)*. 2024, pp. 1–6. DOI: 10.1109/GCWkshp64532.2024.11101632.

[112] Jian Wang et al. "GPS/BDS RTK Positioning based on Equivalence Principle Using Multiple Reference Stations". In: *Remote Sensing* 12.19 (2020), p. 3178. DOI: 10.3390/rs12193178. URL: https://www.mdpi.com/2072-4292/12/19/3178.

[113] *O-RAN Architecture Overview*. O-RAN Software Community documentation. Cherry release, retrieved from O-RAN SC website. 2025.

[114] Mohsen Ahadi et al. *Experimental Insights from OpenAirInterface 5G positioning Testbeds: Challenges and solutions*. 2025. arXiv: 2508.19736 [cs.NI]. URL: https://arxiv.org/abs/2508.19736.

[115] Kaiming He et al. "Masked Autoencoders Are Scalable Vision Learners". In: *CoRR* abs/2111.06377 (2021). arXiv: 2111.06377. URL: https://arxiv.org/abs/2111.06377.

[116] Adeel Malik et al. "From concept to reality: 5G positioning with open-source implementation of UL-TDoA in OpenAirInterface". In: *arXiv preprint arXiv:2409.05217* (2024).

[117] Panorama Antennas. *Directional Antennas Product Information*. https://www.panorama-antennas.com/. Accessed: 2025-09-17.

[118] *O-RAN Fronthaul Control, User and Synchronization Plane Specification*. Tech. rep. O-RAN.WG4.CUS.0-v10.00. Available: https://www.o-ran.org/specifications. O-RAN ALLIANCE, July 2023.

[119] 3GPP. *Study on NR positioning support (Release 16)*. Tech. rep. TR 38.855 V16.0.0. 3rd Generation Partnership Project (3GPP), July 2019. URL: https://portal.3gpp.org/desktopmodules/Specifications/SpecificationDetails.aspx?specificationId=3389.

[120] Shanzhi He et al. "Overview of 5G NR positioning". In: *China Communications* 17.4 (Apr. 2020), pp. 92–119. DOI: 10.23919/JCC.2020.04.008.

[121] Y. Shen and M. Z. Win. "Fundamental Limits of Wideband Localization---Part II: Cooperative Networks". In: *IEEE Transactions on Information Theory* 56.10 (Oct. 2010), pp. 4981–5000. DOI: 10.1109/TIT.2010.2069030.

[122] Henk Wymeersch et al. "5G mmWave Positioning for Vehicular Networks". In: *IEEE Wireless Communications* 24.6 (Dec. 2017), pp. 80–86. DOI: 10.1109/MWC.2017.1700033.

[123] 3GPP. *Architecture enhancements for 5G System (5GS) to support Vehicle-to-Everything (V2X) services (Release 16)*. Tech. rep. TS 23.287 V16.2.0. 3rd Generation Partnership Project (3GPP), Dec. 2020. URL: https://portal.3gpp.org/desktopmodules/Specifications/SpecificationDetails.aspx?specificationId=3473.

[124] Fan Liu et al. "Joint Radar and Communication Design: Applications, State-of-the-Art, and the Road Ahead". In: *IEEE Transactions on Communications* 68.6 (June 2020), pp. 3834–3862. DOI: 10.1109/TCOMM.2020.2973976.

[125] Trung-Kien Le, Sebastian Wagner, and Florian Kaltenberger. "5G Sidelink Positioning in 3GPP Release 18 and Release 19". In: *CSCN 2023, IEEE Conference on Standards for Communications and Networking*. IEEE. Munich, Germany: IEEE, Nov. 2023, pp. 171–176. DOI: 10.1109/CSCN60443.2023.10453143. URL: https://hal.science/hal-04502465.